AD-A045 134 NAVAL POSTGRADUATE SCHOOL MONTEREY CALIF F/G 10/3
SCANNING ELECTRON MICROSCOPE STUDY OF POROUS ZINC BATTERY ELECT--ETC(U)
JUN 77 J R SAVORY

UNCLASSIFIED NL

1 OF 2
AD
AD045134

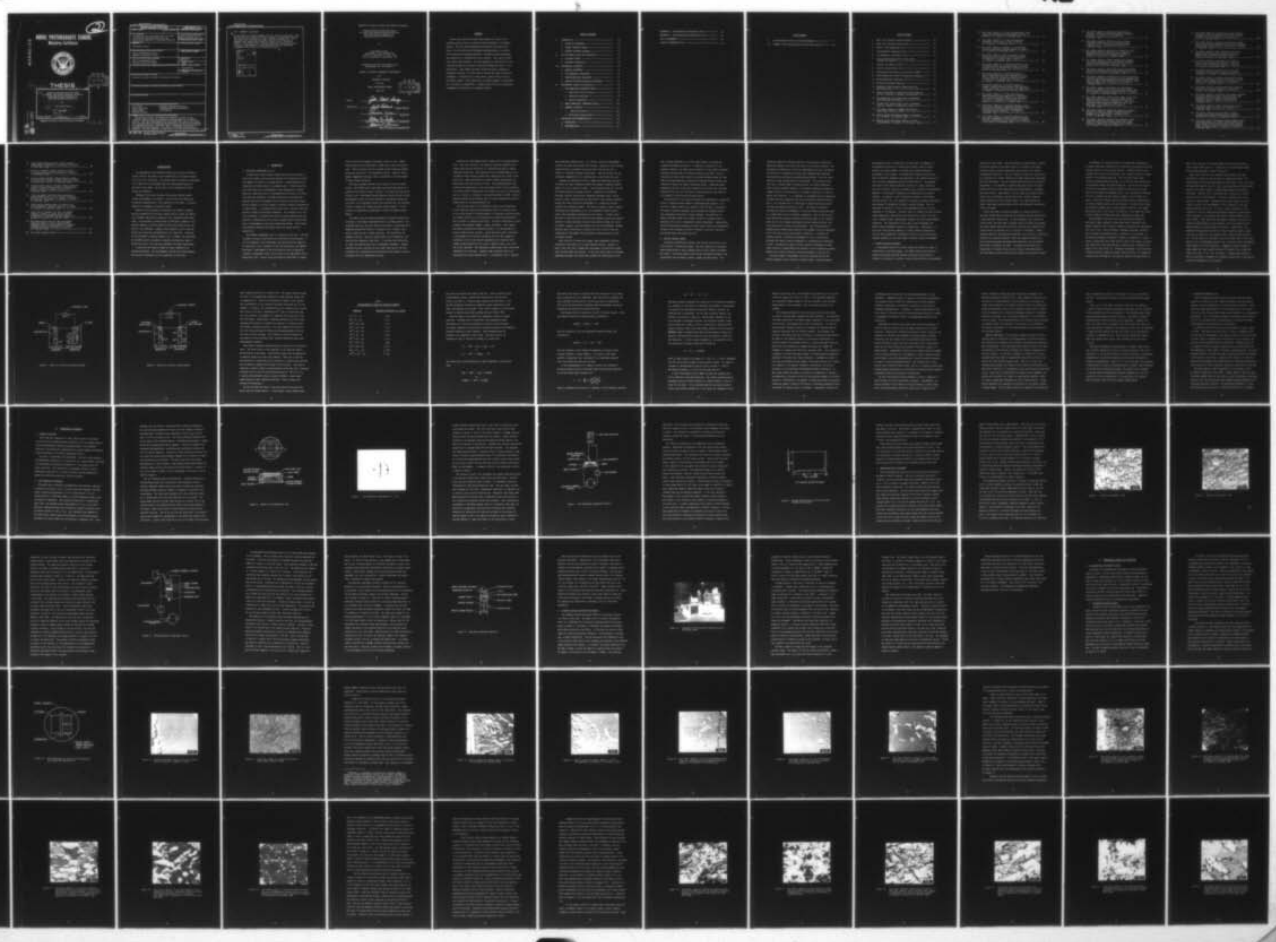

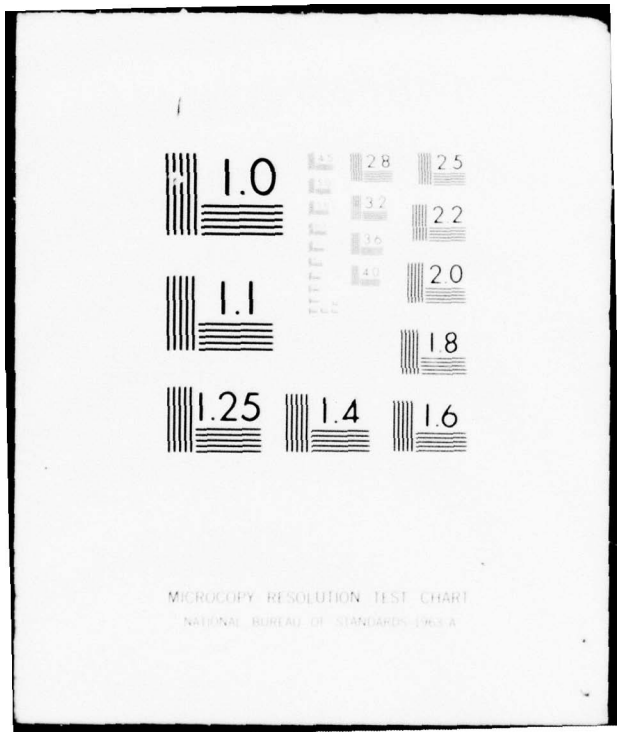
1.0
1.1
1.25
1.4
1.6
2.8
2.5
3.2
2.2
3.6
2.0
4.0
1.8
MICROCOPY RESOLUTION TEST CHART
NATIONAL BUREAU OF STANDARDS 1963 A

NAVAL POSTGRADUATE SCHOOL

Monterey, California

(9) Master's THESIS,

(6) SCANNING ELECTRON MICROSCOPE STUDY
OF POROUS ZINC BATTERY ELECTRODE OXIDATION
AFTER SERVICE-LIKE EXPOSURES IN
POTASSIUM HYDROXIDE ELECTROLYTE

by

(10) John Robert Savory

(11) June 1977

(12) 166 p.

Thesis Advisor: J. Perkins

Approved for public release; distribution unlimited.

251 450

UNCLASSIFIED
SECURITY CLASSIFICATION OF THIS PAGE (When Data Entered)

REPORT DOCUMENTATION PAGE		READ INSTRUCTIONS BEFORE COMPLETING FORM
1. REPORT NUMBER	2. GOVT ACCESSION NO.	3. RECIPIENT'S CATALOG NUMBER
4. TITLE (and Subtitle) Scanning Electron Microscope Study of Porous Zinc Battery Electrode Oxidation after Service-Like Exposures in Potassium Hydroxide Electrolyte		5. TYPE OF REPORT & PERIOD COVERED Mechanical Engineer and Master's Thesis; June 1977 6. PERFORMING ORG. REPORT NUMBER
7. AUTHOR(s) John Robert Savory		8. CONTRACT OR GRANT NUMBER(s)
9. PERFORMING ORGANIZATION NAME AND ADDRESS Naval Postgraduate School Monterey, California 93940		10. PROGRAM ELEMENT, PROJECT, TASK AREA & WORK UNIT NUMBERS
11. CONTROLLING OFFICE NAME AND ADDRESS Naval Postgraduate School Monterey, California 93940		12. REPORT DATE June 1977 13. NUMBER OF PAGES 168
14. MONITORING AGENCY NAME & ADDRESS(if different from Controlling Office)		15. SECURITY CLASS. (of this report) Unclassified 15a. DECLASSIFICATION/DOWNGRADING SCHEDULE

16. DISTRIBUTION STATEMENT (of this Report)

Approved for public release; distribution unlimited.

17. DISTRIBUTION STATEMENT (of the abstract entered in Block 20, if different from Report)

18. SUPPLEMENTARY NOTES

19. KEY WORDS (Continue on reverse side if necessary and identify by block number)

Zinc anode
Porous electrode
Shape change
Alkaline battery
Oxidation product morphology
Potassium hydroxide electrolyte
Zinc dendrite

20. ABSTRACT (Continue on reverse side if necessary and identify by block number)

Porous zinc battery electrodes were modeled for study of the oxidation products that are produced during discharge in an alkaline battery. Two- and three-dimensional pore models were used in the study. The electrodes were discharged galvanostatically in electrolyte solutions of potassium hydroxide. Oxidation product morphology was studied with a scanning electron microscope. Two types of oxidation product were observed. One type appeared to form directly on the electrode surface

DD FORM 1 JAN 73 1473 EDITION OF 1 NOV 65 IS OBSOLETE
S/N 0102-014-6601 |

UNCLASSIFIED
SECURITY CLASSIFICATION OF THIS PAGE (When Data Entered)

(20. ABSTRACT Continued)

as the result of reaction between the zinc and the electrolyte. This product was dark colored and fairly complete on passivated surfaces. The other type of product was light colored and incomplete. It appeared as a second layer, usually found on top of the darker product. This second type of product appears to precipitate out of solution at passivation. Strong pitting of the zinc base metal accompanies the production of oxidation product.

Approved for public release; distribution unlimited.

Scanning Electron Microscope Study of Porous Zinc Battery Electrode Oxidation after Service-Like Exposures in Potassium Hydroxide Electrolyte

by

John Robert Savory
Lieutenant, United States Navy
B.S.M.E., University of Utah, 1968
M.B.A., University of New Haven, 1974

Submitted in partial fulfillment of the
requirements for the degrees of

MASTER OF SCIENCE IN MECHANICAL ENGINEERING

and

MECHANICAL ENGINEER

from the

NAVAL POSTGRADUATE SCHOOL

June 1977

Author John Robert Savory

Approved by: Jeff Peshkin
Thesis Advisor

Theodore Katsanis
Co-Advisor

Allen E. Fuhs
Chairman, Department of Mechanical Engineering

Robert A. Brown
Dean of Science and Engineering

ABSTRACT

Porous zinc battery electrodes were modeled for study of the oxidation products that are produced during discharge in an alkaline battery. Two- and three-dimensional pore models were used in the study. The electrodes were discharged galvanostatically in electrolyte solutions of potassium hydroxide. Oxidation product morphology was studied with a scanning electron microscope. Two types of oxidation product were observed. One type appeared to form directly on the electrode surface as the result of reaction between the zinc an the electrolyte. This product was dark colored and fairly complete on passivated surfaces. The other type of product was light colored and incomplete. It appeared as a second layer, usually found on top of the darker product. This second type of product appears to precipitate out of solution at passivation. Strong pitting of the zinc base metal accompanies the production of oxidation product.

TABLE OF CONTENTS

I. INTRODUCTION ---------- 16

A. HISTORICAL BACKGROUND ---------- 16

B. BATTERY INDUSTRY TRENDS ---------- 20

C. BATTERY ELECTRODE RESEARCH ---------- 22

II. ZINC ELECTRODE THEORY AND CONSTRUCTION ---------- 27

A. ELECTRODE THEORY ---------- 27

B. ELECTRODE CONSTRUCTION ---------- 39

III. EXPERIMENTAL PROCEDURES ---------- 42

A. GENERAL PROCEDURES ---------- 42

B. TWO-DIMENSIONAL EXPERIMENT ---------- 42

C. THREE-DIMENSIONAL EXPERIMENT ---------- 50

D. SCANNING ELECTRON MICROSCOPE PROCEDURES ---------- 61

IV. EXPERIMENTAL RESULTS AND DISCUSSION ---------- 66

A. TWO-DIMENSIONAL EXPERIMENT RESULTS ---------- 66

1. Penetration Profile Results ---------- 66

2. Oxidation Morphology ---------- 69

3. Dendrite Morphology ---------- 107

B. THREE-DIMENSIONAL EXPERIMENT RESULTS ---------- 120

C. SUMMARY OF RESULTS ---------- 143

1. Quantitative Results ---------- 148

2. Postulated Oxidation Model ---------- 148

V. CONCLUSIONS AND RECOMMENDATIONS ---------- 153

A. CONCLUSIONS ---------- 153

B. RECOMMENDATIONS ---------- 154

APPENDIX A: Two-Dimensional Experimental Data ---------- 156

APPENDIX B: Three-Dimensional Experimental Data ---------- 162

LIST OF REFERENCES ---------- 164

INITIAL DISTRIBUTION LIST ---------- 166

LIST OF TABLES

I. Electrochemical Series for Selected Elements ---------- 31

II. Summary of Zinc Anode Oxidation Quantitative Results ------ 149

LIST OF FIGURES

1. Basic cell reactions during discharge ---------- 28

2. Basic cell reactions during charge ---------- 29

3. Sketch of two-dimensional cell ---------- 44

4. Two-Dimensional experiment cell, 1.4X ---------- 45

5. Two-dimensional experiment circuit ---------- 47

6. Typical passivation curve for zinc anode (1N KOH, 23.3 mA/cm^2) ---------- 49

7. Typical zinc spheres, 580X ---------- 52

8. Typical plated spheres, 63X ---------- 53

9. Microtomed plated sphere cross-sections, 3000X ---------- 54

10. Three-dimensional sphere bed experiment apparatus ------- 55

11. Three-dimensional experiment circuit ---------- 57

12. Monolayer experiment apparatus ---------- 60

13. Cambridge S4-10 Stereoscan Scanning Electron Microscope (SEM) ---------- 62

14. Charge transferred to reduce zinc anode oxidation film as a function of distance from separator ---------- 68

15. Two-dimensional cell anode region designations used during SEM observations ---------- 70

16. Polished zinc anode surface, prior to exposure, region A, adjacent to separator, 1120X ---------- 71

17. Zinc anode, region A, polished and etched to reveal grain structure, 200X ---------- 72

18. Heavily pitted zinc anode, region A; 10 minutes at 1.67 mA/cm^2 in 9.96N KOH, 520X ---------- 74

19. Heavily pitted zinc anode, region A, 0.1 mm from separator; 10 minutes at 1.67 mA/cm^2, 520X --------- 75

20. Zinc anode, region A, 0.25 mm from separator; local large pits and possible grain boundary etching; 10 minutes at 1.67 mA/cm^2 in 9.96N KOH, 520X ---------- 76

21. Zinc anode, region A, 0.75 mm from separator; assortment of various pit sizes; 10 minutes at 1.67 mA/cm^2 in 9.96N KOH, 520X ---------- 77

22. Zinc anode, region D, adjacent to outside edge; deep pits resulting from edge effects; 10 minutes at 1.67 mA/cm^2 in 9.96N KOH, 510X ---------- 78

23. Zinc anode, region A, next to separator; heavy oxidation product layer covering pitted surface; 21 minutes at 1.67 mA/cm^2 plus 12 minutes at 6.67 mA/cm^2 in 9.96N KOH, 220X ---------- 80

24. Zinc anode, region B, 1.5 mm from separator; thick oxidation product layer showing partial cracking; 21 minutes at 1.67 mA/cm^2 plus 12 minutes at 6.67 mA/cm^2 in 9.96N KOH, 200X ---------- 81

25. Zinc anode, region B, 1.9 mm from separator; edge of dense oxidation layer showing pits which are not completely covered by oxidation product; 21 minutes at 1.67 mA/cm^2 plus 12 minutes at 6.67 mA/cm^2 in 9.96N KOH, 550X ---------- 82

26. Zinc anode, region B, 2.0 mm from separator; boundary between oxidation product layer and bare, pitted zinc surface; 21 minutes at 1.67 mA/cm^2 plus 12 minutes at 6.67 mA/cm^2 in 9.96N KOH, 200X ---------- 83

27. Zinc anode, region B, 2.15 mm from separator; oxidation product layer edge next to pitted bare zinc surface; oxidation products just starting to cover pits; 21 minutes at 1.67 mA/cm^2 plus 12 minutes at 6.67 mA/cm^2 in 9.96N KOH, 550X ---------- 84

28. Zinc anode, region B, 2.4 mm from separator; bare surface pits and small precipitate oxidation product particles at sites near pits; 21 minutes at 1.67 mA/cm^2 plus 12 minutes at 6.67 mA/cm^2 in 9.96N KOH, 550X ---------- 85

29. Zinc anode, region D, 5.0 mm from separator; etch pits and surrounding nucleation sites of oxidation products; 21 minutes at 1.67 mA/cm^2 plus 12 minutes at 6.67 mA/cm^2 in 9.96N KOH, 200X ---------- 86

30. Zinc anode, region A; faceted pit which has been partially covered by both gray and white oxidation products; 17.5 minutes at 6.67 mA/cm^2 in 9.96N KOH, 2300X ---------- 90

31. Zinc anode, region A; closeup of gray and white oxidation products which have partially covered a faceted pit; 17.5 minutes at 6.67 mA/cm^2 in 9.96N KOH, 5700X ---------- 91

32. Zinc anode, region B; faceted pits covered by a thin gray oxidation layer over which there appears an incomplete layer of white oxidation product; 15 minutes at 10 mA/cm^2 in 9.96N KOH, 2500X ---------- 92

33. Zinc anode, region A; view of geometrically shaped pits within faceted base metal structure; oxidation product growth beginning to flow into pits; 17.5 minutes at 6.67 mA/cm^2 in 9.96N KOH, 2400X ---------- 93

34. Zinc anode, region A; view within faceted pit showing growth of both gray and white oxidation products; 17.5 minutes at 6.67 mA/cm^2 in 9.96N KOH, 2400X ---------- 94

35. Zinc anode, region B; closeup view of etch pits showing corrosive undercutting and growth of gray oxidation layer over pit edges; white oxidation product nucleation sites visible close to pits; 15 minutes at 10 mA/cm^2 in 9.96N KOH, 2400X ---------- 95

36. Zinc anode, region C; base metal pit surrounded by partially complete layer of gray oxidation product upon which deposit of white product has started; 15 minutes at 10 mA/cm^2 in 9.96N KOH, 2300X ---------- 96

37. Zinc anode, region D, close to outer edge; pitted base metal structure partially covered by smooth, gray oxidation product layer; a sprinkling of small white oxidation product particles appears on top of the gray layer; 17.5 minutes at 6.67 mA/cm^2 in 9.96N KOH, 2400X ---------- 97

38. Zinc anode, region B; cumulative buildup of oxidation products resulting in smooth, rounded surface; 21 minutes at 1.67 mA/cm^2 plus 12 minutes at 6.67 mA/cm^2 in 9.96N KOH, 2600X ---------- 98

39. Zinc anode, region B; closeup view of smooth, thick oxidation layer showing surface cracks and "furry" texture; 21 minutes at 1.67 mA/cm^2 plus 12 minutes at 6.67 mA/cm^2 in 9.96N KOH, 13000X ---------- 99

40. Zinc anode, region A; closeup view of gray and white oxidation products showing similar surface textures; 21 minutes at 1.67 mA/cm^2 plus 12 minutes at 6.67 mA/cm^2 in 9.96N KOH, 6600X ---------- 100

41. Zinc anode, region B; surface pits partially aligned along possible grain boundary; gray and white oxidation products are covering surface; 15 minutes at 10 mA/cm^2 in 9.96N KOH, 1120X ---------- 102

42. Zinc anode, region B; gray oxidation layer nearly complete over surface pits; nucleation sites of white oxidation products are also in view; 15 minutes at 10 mA/cm^2 in 9.96N KOH, 1150X ---------- 103

43. Zinc anode, region B; incomplete gray oxidation product layer surrounding etch pits; a thin top cover of white product also appears; 15 minutes at 10 mA/cm^2 in 9.96N KOH, 1250X ---------- 104

44. Zinc anode, region B; closeup view of pits with oxidation product growth outlining cavity edges; 15 minutes at 10 mA/cm^2 in 9.96N KOH, 6200X ---------- 105

45. Zinc anode, region C; complete gray oxidation layer (darker in some areas) which is covered by a partial layer of white oxidation product; 15 minutes at 10 mA/cm^2 in 9.96N KOH, 620X ---------- 106

46. Zinc anode, region C; gray and white dual oxidation products, white layer incomplete; 15 minutes at 10 mA/cm^2 in 9.96N KOH, 1120X ---------- 108

47. Zinc anode, region C; transition zone between complete two-layer oxidation products (gray and white) and incomplete two-layer products (complete gray, incomplete white); 15 minutes at 10 mA/cm^2 in 9.96N KOH, 570X ---------- 109

48. Zinc anode, region B; view of dense layer of white oxidation product; 15 minutes at 10 mA/cm^2 in 9.96N KOH, 1200X ---------- 110

49. Zinc anode, region B; gray and white oxidation products, white product showing vertical growth; 15 minutes at 10 mA/cm^2 in 9.96N KOH, 2400X ---------- 111

50. Zinc anode, region B; boundary between complete white oxidation product layer (left) and incomplete white layer (right); gray oxidation product layer appears below the white product; 15 minutes at 10 mA/cm^2 in 9.96N KOH, 600X ---------- 112

51. Separator between zinc anode and copper cathode; view of zinc dendrites growing from cathode to anode; 21 minutes at 1.67 mA/cm^2 plus 12 minutes at 6.67 mA/cm^2 in 9.96N KOH, 17X ---------- 113

52. Zinc anode, region A, adjacent to separator; view of shorting dendrite which has grown across separator from cathode; thick, cracked surface of oxidation product layer also visible; 21 minutes at 1.67 mA/cm^2 plus 12 minutes at 6.67 mA/cm^2 in 9.96N KOH, 100X ---------- 114

53. Copper cathode, next to separator; typical clusters of hexagonal zinc plates which grow during initial stages of cathodic plating; 21 minutes at 1.67 mA/cm^2 plus 12 minutes at 6.67 mA/cm^2 in 9.96N KOH, 1100X ---------- 116

54. Copper cathode, next to separator; typical stacked hexagonal plates resulting from zinc plating; 21 minutes at 1.67 mA/cm^2 plus 12 minutes at 6.67 mA/cm^2 in 9.96N KOH, 1080X ---------- 117

55. Copper cathode, adjacent to separator; view of zinc plating which has initially grown in vertical columns and then moved horizontally across separator to form a shorting dendrite; 21 minutes at 1.67 mA/cm^2 plus 12 minutes at 6.67 mA/cm^2 in 9.96N KOH, 220X ---------- 118

56. Separator between cathode and zinc anode; closeup of ordered zinc plates that comprise a dendrite which has grown across the separator from cathode to anode; 21 minutes at 1.67 mA/cm^2 plus 12 minutes at 6.67 mA/cm^2 in 9.96N KOH, 1080X ---------- 119

57. Typical unexposed plated sphere, 580X ---------- 122

58. Silver sphere with visible etch pits; 30 seconds at 50 mA/cm^2 in 9.96N KOH, 1200X ---------- 123

59. Plated sphere showing extensive pitting; 30 seconds at 50 mA/cm^2 in 9.96N KOH, 2400X ---------- 124

60. Zinc sphere with nearly complete gray oxidation layer; several large pits remain uncovered; 30 seconds at 50 mA/cm^2 in 9.96N KOH, 2600X ---------- 126

61. Closeup of zinc sphere pit site with surrounding gray oxidation layer and observable initial oxidation product nucleation within the pit; 30 seconds at 50 mA/cm^2 in 9.96N KOH, 6400X ---------- 127

62. Zinc sphere surface showing complete gray oxidation product layer and nucleation sites of incomplete white oxidation product layer; 30 seconds at 50 mA/cm^2 in 9.96N KOH, 2700X ---------- 128

63. Closeup of zinc sphere surface on which white oxidation product nucleation sites have developed over gray oxide surface layer; 30 seconds at 50 mA/cm^2 in 9.96N KOH, 6700X ---------- 129

64. Plated sphere displaying growth of dark and light ("salt and pepper") oxidation products; 30 seconds at 50 mA/cm^2 in 9.96N KOH, 1200X ---------- 130

65. Plated sphere displaying complete surface cover composed of "salt and pepper" oxidation product; 30 seconds at 25 mA/cm^2 in 9.96N KOH, 1250X ---------- 131

66. Plated sphere completely covered with "salt and pepper" oxidation product layer; 30 seconds at 25 mA/cm^2 in 9.96N KOH, 2500X ---------- 132

67. Closeup view of "salt and pepper" oxidation product on plated sphere; product appears as a cracked gray layer with a scattering of white particles; 30 seconds at 5 mA/cm^2 in 9.96N KOH, 6700X ---------- 133

68. High magnification view of a dense "salt and pepper" oxidation product layer on a plated sphere surface; individual constituent white and gray products are distinguishable; 30 seconds at 25 mA/cm^2 in 9.96N KOH, 6300X ---------- 134

69. Plated sphere surface on which an incomplete layer of "salt and pepper" oxidation product has grown; 30 seconds at 25 mA/cm^2 in 9.96N KOH, 2500X ---------- 135

70. Closeup of plated sphere surface on which "salt and pepper" oxidation product appears; initial stages of product growth are visible in lower half of photograph; 30 seconds at 25 mA/cm^2 in 9.96N KOH, 6200X ---------- 136

71. Advanced stage of "salt and pepper" oxidation product growth on plated sphere surface; thick, crusty product has developed; 30 seconds at 10 mA/cm^2 in 9.96N KOH, 1250X ---------- 137

72. Plated sphere showing growth of dark "pancake" shaped oxidation products; 30 seconds at 50 mA/cm^2 in 9.96N KOH, 1300X ---------- 139

73. Profile of "pancake" shaped oxidation products on plated sphere surface; 30 seconds at 50 mA/cm^2 in 9.96N KOH, 2500X ---------- 140

74. View of single "pancake" shaped oxidation product on plated sphere surface; dimpled center is visible; 30 seconds at 50 mA/cm^2 in 9.96N KOH, 2500X ---------- 141

75. Closeup profile view of "pancake" shaped oxidation products on plated sphere; height of products is clearly visible; 30 seconds at 50 mA/cm^2 in 9.96N KOH, 6300X ---------- 142

76. "Salt and pepper" oxidation product growing on plated sphere surface; a few "pancake" oxidation products are also present; 30 seconds at 5 mA/cm^2 in 9.96N KOH, 1320X ---------- 144

77. Plated sphere showing growth of "pancake" and "salt and pepper" oxidation products; 30 seconds at 50 mA/cm^2 in 9.96N KOH, 1200X ---------- 145

78. Close view of "pancake" and "salt and pepper" oxidation products on plated sphere surface; transparency of "pancakes" may be observed; 30 seconds at 50 mA/cm^2 in 9.96N KOH, 2400X ---------- 146

79. High magnification view of "salt and pepper" oxidation product on plated sphere surface; transparent dark and gray patches are "pancake" oxidation products; 30 seconds at 50 mA/cm^2 in 9.96N KOH, 6100X ---------- 147

80. Zinc anode oxidation model ---------- 150

ACKNOWLEDGMENT

The experimental work performed during this study was performed jointly with Dr. Ted Katan of the Lockheed Palo Alto Research Laboratory, Palo Alto, California. The author wishes to express his gratitude to Dr. Katan for his invaluable help and understanding during all portions of this study. He has been a fine colleague and friend during this research.

Throughout this study Professor Jeff Perkins offered helpful counsel and guidance as an advisor. His help was very useful and contributed significantly to the completion of the study. A sincere thank-you is extended to Professor Perkins.

Material Science Laboratory Technician, Roy Edwards, deserves special recognition for his never ending efforts to keep the laboratory equipment operational, especially the scanning electron microscope. On the several occasions when the SEM didn't respond to the author's demands it was the tender-loving-care provided by Roy that made all the difference. Numerous other demands on Roy's time and skills were always met enthusiastically and cheerfully. Gratitude is also extended to Research Chemist, Ken J. Graham. Ken was always an available source of answers to chemical problems that came up during this study. His help and friendship are deeply appreciated.

A final and very special thanks is warmly extended to my loving wife Maureen. Her encouragement, patience and understanding were directly responsible for the completion of this work.

I. INTRODUCTION

A. HISTORICAL BACKGROUND [1,2,3,4]

A device that stores chemical energy which may be converted to electrical energy, and thus allows delivery of an electrical current upon demand, is known as a storage battery. Storage batteries are classified as either primary or secondary types. Primary batteries are those which are non-rechargeable after expenditure of energy. These are single-direction or dischargeable-only devices; the useful life ends upon discharge. Secondary batteries are two-direction devices; they may be recharged (from an exterior electrical energy source) because of a certain degree of inherent chemical reversibility in their design. A secondary battery thus lives a cyclical life comprised of charge and discharge components. The original use of the term "secondary" to describe this type of battery resulted from the practice of charging this device from a primary battery during times prior to development of electrical generating methods. Thus primary and secondary described the energy source and energy receiver respectively.

The smallest independent unit of a battery is the cell. A battery is simply a group of cells which are electrically interconnected. A cell is comprised of two electrodes, one positive and one negative, an electrolyte, and a container to hold the electrolyte and immersed electrodes. Development of the first electric cells is generally credited to Alessandro Volta, as the result of his experiments which began about 1796. Volta's cells used positive electrodes of copper,

brass or silver and negative electrodes of zinc or tin. Simple electrolytes such as plain water or some type of salty fluid were used. Volta's initial work was followed by many alternate designs during the first half of the nineteenth century. Daniell, Grove, Bunsen, Poggendorff and many others contributed to the development of early primary batteries.

The first secondary battery was the result of work by Gaston Planté. The Planté battery used sheet lead electrodes spaced by a separator and coiled to form a cylinder. The electrolyte was dilute sulfuric acid. The Planté lead-acid battery system received further developmental effort from many individual contributors during the last part of the nineteenth century and continued into the twentieth century to become the leading secondary battery system. It still retains its popularity and dominance in today's secondary battery market.

The 1860's were also years during which Leclanché developed his prototype of the modern flashlight battery, a primary battery. The Leclanché cell was a wet cell using a zinc anode, a conducting mix of manganese dioxide and carbon in a porous pot as a cathode, with a central carbon rod as a current collector. The electrolyte was ammonium chloride. This cell proved itself to be inexpensive, non-corrosive and reasonably long lived. It received wide initial use in light load applications such as telegraphic equipment. Gassner improved the cell by having the zinc anode serve also as the cell container and by immobilizing the electrolyte with plaster of paris. The modern dry cell subsequently evolved.

Alkaline cell development began in 1881 with the Lalande-Chaperon cell. This cell utilized a zinc negative electrode combined with a copper oxide positive electrode in a potassium hydroxide or sodium hydroxide electrolyte. Many variations of the Lalande-Chaperon cell followed as other inventors added their imagination and talent to the basic cell. Early applications included a French experimental submarine and a New York trolley car line. The Lalande-Chaperon cells suffered from dissolution of zinc and copper oxide in the electrolyte. In the late 1800's Thomas Edison took interest in the cell and improved upon it, taking out a patent on the improved version in 1889. Edison's improved version found extensive use in railway signaling devices and became known as the Edison-Lalande cell.

The last few years of the nineteenth century and the beginning of the twentieth century saw considerable effort in different parts of the world devoted to the development of a secondary alkaline battery. The primary task was to find successfully suitable electrodes which were insoluble in alkaline electrolyte. The major contributors to this research were Waldemar Jungner, a Swede, and Edison. Both Jungner and Edison considered the lead-acid battery to be unacceptable as a light, portable source of power. Edison was particularly interested in development of an electric automobile and felt that commercial production of such a car would be impossible with lead-acid cells. Jungner worked extensively with nickel, cadmium, copper, iron, zinc and silver compounds. His experiments probed almost every conceivable combination of electrodes. Jungner's name ultimately came to be associated with nickel-cadmium cells. A considerable part of Edison's

work paralleled Jungner's work. As a result, there was considerable activity in patent suits between the two men. Instead of joint research characterized by cooperation with each other, the two men left a history of turbulent relations behind them. Edison's battery work was ultimately remembered for his contributions to the nickel-iron cell.

Although the exploratory work of Jungner and Edison was carried on by others, the early twentieth century saw extensive commercial development of only two battery systems: the Leclanché primary dry cell and the Planté lead-acid secondary battery. Batteries for automobile starting, military applications, telephone exchanges, buses, trucks, aircraft, ships, railroads and the multitude of other devices appearing during this time required the development of a competitive battery industry for production support. The battery industry, however, emphasized empirical improvement of the two predominant battery systems rather than stimulating development of new systems. It wasn't until World War II and later that new and diverse demands required the battery industry to pursue extensive research into battery systems that could be smaller, lighter, and more powerful than the two predominant systems. Military needs of World War II spilled over into an era of post war technological developments which provided continued stimulus for new and better systems.

After the work of Edison and Jungner, many independent inventors continued in the pursuit of an ideal alkaline battery. However, it wasn't until 1941 that a significant development occurred which helped pave the path toward new systems. In that year Henri André, a Frenchman, published his paper "The Silver-Zinc Accumulator" describing his work

with a system comprised of a silver oxide cathode, zinc anode and potassium hydroxide electrolyte. In addition to promotion of the system's potential, the paper gave recognition to the system's problems, carefully analyzed them, and offered practical solutions. With the concurrent war effort and interest in systems showing promise for high power and energy densities, André's work inspired further interest and research by others into André's system and others. André had worked extensively with the silver-zinc system since the 1920's and continued working with it well into the 1950's, even producing his own electric car powered by the silver-zinc battery system.

Since World War II the battery industry has demonstrated a continuous effort to develop systems capable of maximizing power density. The search for lighter weight, more powerful cells has been in response to the needs of military programs, space programs and consumer products that developed as spin-offs of those programs. One needs only to examine the power supply for a pocket calculator or digital watch to appreciate this type of contemporary battery requirement. Additionally, the petroleum product shortages of recent years, as well as environmental concerns, have rekindled the kind of interest in electric cars which preoccupied Edison and André years ago.

B. BATTERY INDUSTRY TRENDS

The battery industry has evolved, over the last 150 years or so of world history, in three main stages. The first stage was an inventive phase characterized by early pioneers such as Volta, Planté, Leclanché and others. The second stage could be called the empirical phase, with contributors such as Gassner, Edison, Jungner and many others. The

empirical stage has a dominant position in the evolution process, and empiricism remains very strong even today in the battery industry. The philosophy of empiricism is such that improvement upon basic inventions was and still is conducted by placing major emphasis upon operating characteristics and practical manufacturing problems; "trial and error" might be a crude classification of this method. The transition from the first to second stage is neither distinct nor easily identified. There have been numerous examples of interwoven inventive and empirical stages in which an inventor went on to become an empiricist in order to improve his invention. It is important to understand that the empiricist provided the major foundation upon which the battery industry has been built. The contributions of a multitude of empiricists have provided most battery design as we know it today. The result of empirical influence has been the development of a battery industry whose practices to a large extent have no scientific foundation. Even on the few occasions when basic scientific research efforts were made, as the industry grew, the all too frequent end product was that research results could not be correlated to actual cell performance. Thus the motivation to design battery systems using scientific and academic tools was negligible due to the lack of most early research credibility. Ultimately an industry starved in theoretical knowledge but rich in practicality furnished the battery products demanded by a technologically developing society. The empirical stage of battery industry development is sometimes credited to Thomas Edison and referred to as the Edisonian approach. Almost all of today's batteries have been developed in this way [3].

The third stage of development, and still relatively new to the battery industry, may be called the research stage. Although research

was shunned in favor of empiricism for many years, the demands of a technological world have in recent years created a need for basic research to provide answers to problems that inhibited empirical development of new systems. Providing new and improved battery systems is inherently dependent upon knowledge of the chemistry and structure of battery components and their interactions [2]. The movement away from art and toward scientific principle is clearly evident by the bulk of battery literature available today, authored by distinguished members of the scientific community and documenting basic research findings. As recently as 1947 the Battery Division of the Electrochemical Society, Inc., was organized to stimulate research, publication, and exchange of information relating to battery systems. Thus the influence of research is a very recent phenomenon and not yet fully ingrained in the industry. The major thrust of research has been directed toward examination, description, and verification of basic cell reactions, transport modes, morphological changes, and other electrochemical properties. The translation of this type of basic knowledge into battery design parameters remains an ultimate goal. References 5, 6, 7 and 8 are a few selected examples of current research thinking and activity which demonstrate the general direction of the basic battery research movement in this third stage of battery industry development.

C. BATTERY ELECTRODE RESEARCH

A considerable portion of battery theory and research is aimed at optimization of electrode design. The simple planar electrode with a single well-defined interface between electrolyte and electrode is limited in its ability to provide a large contact area for electrochemical

reaction per unit volume. Since the amount of electrochemical reaction is directly related to the power output of the battery, the planar electrode tends to prevent large power output without also having a corresponding large size. This is a simple but important concept since the usefulness of a battery system for portable applications diminishes with size and weight. Thus for portable applications such as electric automobiles, it is desirable to provide some other type of electrode design, which will allow compactness and minimum weight to accompany high power output. Additionally, for both fixed and portable applications, size can influence cost and thus affect a battery system's competitiveness with other energy sources. For these reasons and others, high output battery design efforts have generally incorporated porous electrodes.

Porous electrodes are usually designed as a matrix structure of some type through which electrolyte can penetrate and make contact with a large electrode surface area. In their simplest form, porous electrodes usually have some type of skeletal grid to provide the necessary structural support upon which the active (reaction participating) electrode material is placed by one of a variety of techniques. Design leading conditions, manufacturing technology, cost, and other constraints influence the technique selected. There are numerous variations of porous electrode design and manufacturing practices, but the desired end product is basically the same: to produce an electrode with a large number of reaction sites per unit volume, thus contributing to the power density (power output per unit volume) of the battery system.

The geometry of electrode design is one important consideration; an equally important consideration is selection of an appropriate active material, which is a many faceted process. A material decision must consider factors such as availability, cost, weight, half-cell voltage, stability, and manufacturing ease. Zinc has historically been a favorite electrode material because of its low cost, good availability, low equivalent weight, and high voltage [9]. Its use can be traced as far back as the primitive battery systems of Volta and it has been used in both primary and secondary cells. The conventional flashlight dry cell is perhaps the most familiar example of zinc primary cell usage. Silver-zinc alkaline aqueous batteries are most representative of recent secondary battery zinc applications. The silver-zinc system has become an integral part of major missile, satellite, and weapons applications due to its ability to produce up to six times more energy per unit weight and volume than other conventional systems [10].

The marriage of zinc and porous electrode design produces an electrode of great promise for high power density secondary cells. However secondary cells using zinc negative electrodes have experienced poor cyclic life. Cyclic lifetime is dependent upon many variables, such as charge and discharge rates, in addition to cell design. If the detailed influence of specific variables is neglected, in order to obtain a qualitative "ball park" feel for cyclic life values, one finds that silver-zinc cells have typically enjoyed a short lifetime in the range of 10 to 150 cycles [2]. Reference 10 promotes a new silver-zinc "long-life battery" capable of greater than 400 cycles. By comparison, the best cyclic lifetime for the familiar lead-acid storage battery is

about 1400 cycles and for the best alkaline battery system (nickel-iron) is about 4000 cycles [2]. These cyclic lifetime figures assume cyclical deep discharge to about 70% capacity.

Short cyclic life for zinc secondary cells generally has been attributed to failure of the zinc anode or negative electrode. Two failure modes are directly associated with zinc anodes: short circuiting and electrode capacity loss [9]. Short circuiting results from dendritic metallic zinc growth forming a bridge between negative and positive electrodes. Capacity loss is associated with a reduction in surface area of the zinc active material. The loss in reaction area can be related to "shape change." Mechanistically, shape change can be described in terms of the rearrangement of active material on the zinc anode during the cell's life. In this, it must be pointed out that oxidation of the zinc anode during discharge produces an oxide product which is soluble in the alkaline electrolyte, forming complex zincate ions, $Zn(OH)_4^{=}$. Since these ions are capable of moving in solution, an effective redistribution of active material can occur during the subsequent charge or reduction phase of the cycle. Additionally, zinc deposition during charge can take the form of a massive, dense, nodular structure as compared to the original porous, finely divided structure [9]. The net result is a decrease in the true surface area of the active material and a corresponding capacity loss. The basic factors influencing shape change are not well understood. Fundamental research studies of shape change have been reported by Lander [9], McBreen [11], Lander and Cooper [12], Choi, et al., [13], and others. Solving these problems of the zinc electrode is paramount to successful exploitation of the positive attributes possessed by this electrode.

With these basic ideas in mind, the intent of this research was to add to the growing body of scientific knowledge about zinc electrodes that ultimately may help find solutions to the problems that limit utilization of zinc's strong assets in secondary batteries. This research attempted to expose zinc electrodes to alkaline service conditions and then study the changes which occurred as a result of such exposure. The discharge or oxidation phase of the cycle was of primary interest in this study. It was particularly desired to examine the morphological changes occurring at the zinc anode during oxidation to obtain a greater understanding of the nucleation and growth process of oxidation products. The primary analytical tool used in this study was the scanning electron microscope (SEM).

II. ZINC ELECTRODE THEORY AND CONSTRUCTION

A. ELECTRODE THEORY

The zinc electrode is one constituent of a cell system. It is normally used as the negative electrode or anode in the cell. Completing the cell are a positive electrode, or cathode, and an electrolyte in which both electrodes are immersed. The anode is the electrode at which an oxidation reaction (electrons given up) takes place during cell discharge, while the cathode is the electrode where the corresponding reduction (electron capture) reaction takes place. In order for the cell to be functional, an external circuit is necessary to connect electrically anode and cathode. Through the external circuit, electrons flow from the electrode being oxidized (anode) to the electrode being reduced (cathode). The flow of electrons constitutes an electric current (By convention electric current flux is in the opposite direction to electron flux.). Figure 1 depicts the discharge reactions for a typical basic cell. The reactions shown in Figure 1 are very general in nature, in order to represent any electrolytic cell. At the anode, M represents any metal, and the cathodic reaction shown is only one of many possible cathodic reactions. The reactions for any specific cell will obviously be a function of the specific electrodes and electrolyte used.

A secondary cell is capable of reversal or charging. During charge the roles of cell anode and cathode are reversed such that electrons are released by the new anode (old cathode) and flow to the new cathode (old anode). This role reversal is induced through the use of an externally impressed current from a charging source. Figure 2 depicts

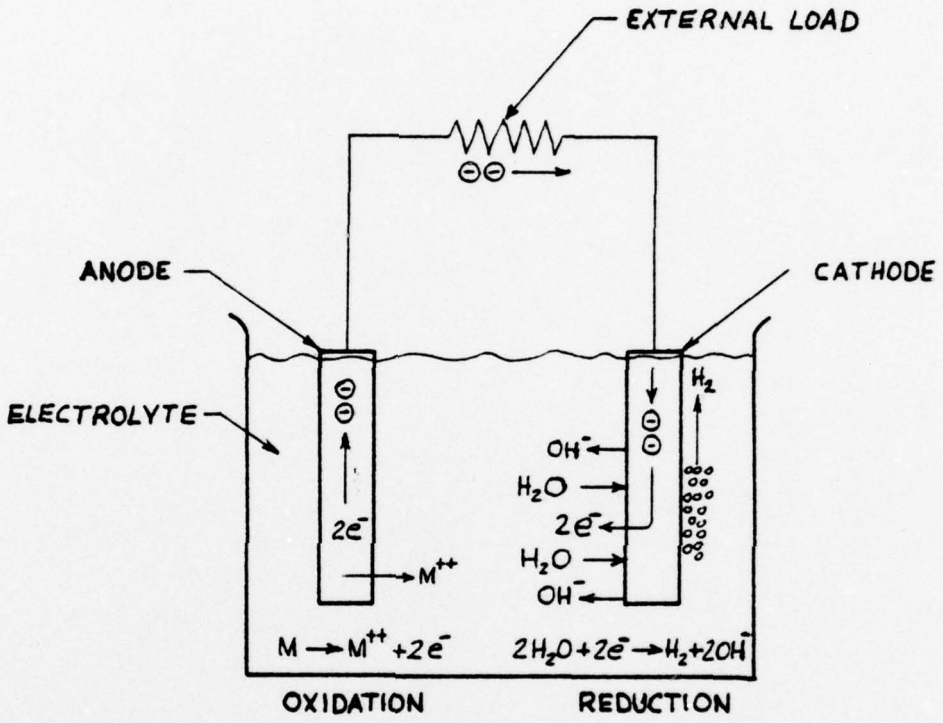

Figure 1. Basic cell reactions during discharge.

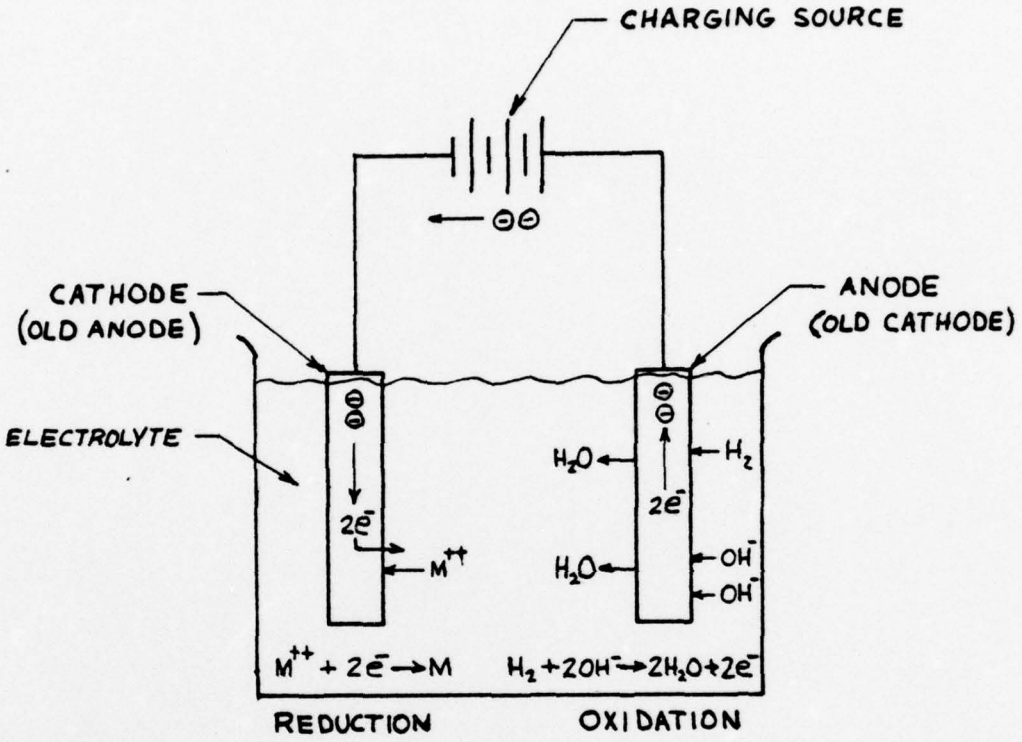

Figure 2. Basic cell reactions during charge.

basic charge reactions for a typical cell. The charge process returns the cell to its predischarge condition by using external energy from a charging source. This is an idealization, however, which assumes full reversibility of all reactions and ideal efficiency for all components. In reality, full reversibility is not possible due to losses that occur in the cycle. Replating of M^{++} ions to form M metal may not occur properly, for example, or reactants such as H_2 may be lost from the system. Additionally, competing reactions may occur during charging which prevent or diminish the reversal of the basic anodic and cathodic discharge reactions. For these reasons and others the cell will lose some capacity during each discharge/charge cycle and thus have a finite lifetime. Cell lifetime is usually measured by the number of cycles available until capacity diminishes below some predetermined threshold.

Many factors influence electrode material selection, as previously noted. One factor which is very important is the ease with which a material gives up electrons. This material quality may be measured as a potential relative to some known standard. When this is done for many materials, the materials may be ordered in a fashion that indicates how one material compares with another in this quality. This type of ordering is usually called an electrochemical series and uses a reference potential value of zero for the reduction reaction: $2H^{+} + 2e^{-} \rightarrow H_2$. A typical electrochemical series is given by Table 1, which ranks common metals by their reduction potential. Table 1 values were obtained from Reference 3.

One can conclude from Table 1 that zinc gives up electrons more easily than any element below it. Additionally, those elements above

Table I

ELECTROCHEMICAL SERIES FOR SELECTED ELEMENTS

Reaction	Reduction Potential, E_o (volts)
$K^+ + e^- \rightarrow K$	- 2.92
$Na^+ + e^- \rightarrow Na$	- 2.71
$Mg^{++} + 2e^- \rightarrow Mg$	- 2.37
$Zn^{++} + 2e^- \rightarrow Zn$	- 0.76
$Fe^{++} + 2e^- \rightarrow Fe$	- 0.44
$Ni^{++} + 2e^- \rightarrow Ni$	- 0.25
$Pb^{++} + 2e^- \rightarrow Pb$	- 0.12
$2H^+ + 2e^- \rightarrow H_2$	0.00
$Cu^{++} + 2e^- \rightarrow Cu$	+ 0.34
$Ag^+ + e^- \rightarrow Ag$	+ 0.80
$Au^{+++} + 3e^- \rightarrow Au$	+ 1.50

zinc give up electrons more easily than zinc. Zinc's location in the electrochemical series, coupled with availability, cost and other factors, has made it a favorite anodic material for many years. Zinc has been anodically coupled with numerous cathodic materials in both acidic and alkaline cell systems. Most current interest in zinc systems centers on alkaline electrolyte systems which use NaOH or KOH.

The zinc anode in an alkaline cell undergoes a series of complex reactions. Although there is uncertainty and disagreement among researchers as to the exact mechanism of reaction during discharge and charge, Reference 9 contains the following reactions as the generally accepted conclusion of most research. The discharge process is believed to be comprised of three steps. The first step is the oxidation of zinc to form ZnO or $Zn(OH)_2$ in a solid form:

$$Zn + 2OH^- \rightarrow ZnO + H_2O + 2e^-$$

or

$$Zn + 2OH^- \rightarrow Zn(OH)_2 + 2e^-$$

The second step is the dissolution of these compounds to form zincate ions:

$$ZnO + 2OH^- + H_2O \rightarrow Zn(OH)_4^=$$

or

$$Zn(OH)_2 + 2OH^- \rightarrow Zn(OH)_4^=$$

The second step reactions continue until the electrolyte is no longer able to dissolve the zinc compounds. When this point is reached, the zinc compounds flourish and as a third step produce a passivating film on the electrode which ultimately ends the discharge reaction by insulating the electrode from the electrolyte.

The charge process is believed to follow a two-step process. First the complex zincate ion produces $Zn(OH)_2$ according to:

$$Zn(OH)_4^{=} \rightarrow Zn(OH)_2 + 2OH^-$$

Then the reduction of the zinc hydroxide compound produces zinc according to:

$$Zn(OH)_2 + 2e^- \rightarrow Zn + 2OH^-$$

The zinc produced in this fashion has generally not been an even, strongly adherent or porous deposit. As a result, some anodic porosity is generally lost, resulting in an accompanying capacity loss of the anode and thus the cell also.

If the thermodynamics of a chemical reaction are considered, electrode potential may be calculated using the principles described by the well known Nernst equation [2]:

$$E = E^\circ - \frac{RT}{nF} \ln \left[\frac{(a_C)^c (a_D)^d}{(a_A)^a (a_B)^b}\right]$$

where a_i represents the activity of component i in the chemical equation:

$$aA + bB \rightarrow cC + dD$$

The Nernst equation expresses the variation of the reversible potential as a function of the activity of reactants and products. Thus knowing the equation that describes an electrode's chemical reaction, its potential may be calculated. For the zinc electrode, however, the process is not quite so clear cut. During anodic discharge of the zinc electrode in alkaline solutions, the oxidation products formed may be either ZnO, $Zn(OH)_2$, or both. Additionally, there have been several different types of ZnO and $Zn(OH)_2$ reported in the literature. Different types of product which bear the same chemical formula are generally differentiated by qualities such as stability, solubility, and reactivity. In view of these complexities, the potential of the zinc electrode in alkaline electrolyte is given by:

$$E = E_o' + 0.059pOH$$

where E_o' takes values in the range of - 1.221 V to - 1.260 V, depending upon the solid product formed on the electrode surface. The range of voltages is characterized by inactive ZnO at one end (- 1.260 V) and amorphous $Zn(OH)_2$ (- 1.221 V) at the other end [9].

A cell's electromotive force (EMF) is simply the algebraic sum of the individual electrode potentials. The cathode potential may be determined using the Nernst equation in a manner similar to that outlined for the anode. If one considers the cell utilizing a silver/silver oxide cathode coupled with a zinc anode, the components of the

familiar silver-zinc cell, the standard cell potential for this system covers the range from 1.566 V to 1.867 V. This high EMF range plus the relatively moderate weight of the cell provides a very favorable energy density value and makes it one of the most attractive cell systems.

The limiting processes for the zinc porous electrode are kinetic in nature, involving mass transport and ionic diffusion. The operating electrode constitutes a two phase system, comprised of a solid electrode structure and a surrounding ionic fluid or electrolyte. In order for the electrode's chemical reactions to proceed, the reactants must be supplied continually and the products removed. The processes that influence this simple idea are the subject of "porous electrode theory." As simple as this general concept is, the analytic description of reaction kinetics is extremely difficult. Porous electrode theory has been dealt with extensively by Newman and Tobias [5], Newman and Tiedeman [7], Delahay and Tobias [8], and many others. Most theoretical treatments of porous electrodes attempt to develop general mathematical equations to describe their overall behavior. Mathematical models of this type are generally quite complex, involving equations that account for transport in the matrix; transport, conservation, and electroneutrality in the solution; and interphase boundary conditions. In most cases, models are unable to account for consumption of reactants and deposition of products as well as the resulting changes in electrode structure. Additionally, the geometry of porous electrodes is generally random and complex, leading to difficulty in predicting parameters which are needed for complete analytic treatment. Experimental research has

increasingly been called upon to provide approximations to those parameters. Newman and Tobias [5] indicate that useful approximations for parameters such as effective conductivity of matrix material, diffusion coefficients, and mobility of species in a pore can be determined experimentally. In general, a better understanding of the local extent of reaction within a porous electrode structure is needed to complement the analytic efforts of distinguished authors in the literature.

Knowledge of reaction rates within pores and the distribution of rates is directly related to the net power available from a porous electrode. Additionally, knowing the distance to which a reaction can penetrate an electrode can determine its optimum design thickness. Electrodes that are thinner than the penetration depth behave like planar electrodes, while those that are thicker than the penetration depth are not fully utilized and therefore constitute a penalty to energy density. Experimental studies such as those of Katan and Bauman [14] and Szpak and Katan [15] are examples of current research efforts which attempt to provide approximations to reaction process parameters in order to refine the modeling effort. The ultimate goal of this overall effort should be kept in mind, that is, to provide scientifically founded design optimization for the purpose of allowing battery industry development beyond the constraints of empiricism.

The zinc electrode has unique problems of its own in addition to those outlined for porous electrodes in general. Increasingly, the service failures of zinc anodes are being attributed to shape change. Short circuiting between cathode and anode, due to dendritic zinc

growth, although a problem, has been controlled successfully with appropriate separator materials [12]. Shape change is believed to be the result of a redistribution of active material by a process that allows active material to be removed ionically from a site during discharge and eventually tied up as an oxidation product which is remote from the original site. During the subsequent reduction of oxidation products on recharge, zinc is therefore deposited at a site different from its origin. Zinc oxidation products are soluble in KOH, producing the complex zincate ion; mobility of the zincate ion is believed to be partially responsible for this redistribution of active material on the electrode surface.

Complete knowledge of zinc oxidation product solubility in KOH is lacking, which is reflected in the disagreement of various sources in the literature; but generally ZnO solubility increases with increasing KOH concentrations. Since ZnO dissolution produces zincate, the local concentration of KOH directly influences the zincate concentration at any cell location. As zincate is produced, of course, OH^- ions are consumed which then tends to decrease KOH concentration; this in turn affects the local zincate reaction rate. The point is that local concentration gradients can develop for both KOH and zincate which can have direct influence, on a microscopic scale, upon reaction rates within a pore. There can be a distribution of reaction rates throughout the porous zinc electrode, as a result of concentration gradients, which can produce undesirable differences in local current density. Concentration gradients are regarded as contributors to the overall problem of shape change. The cell design approach to minimize this problem has

been to maximize the volume of electrolyte in a cell and saturate it with ZnO. This approach, however, has limits associated with weight penalty.

Choi, et al., [13] report convective flows also can develop as a result of KOH and zincate concentration gradients, and can contribute to the redistribution of active material. The resulting shape change eventually means capacity loss and failure. The extent of material redistribution on zinc electrodes can be impressive. MacBreen and Dalin [16] report that in secondary zinc cells cycled 100 times, the zinc electrode had a geometric area reduction of 50%, that the thickness of edges had been reduced, and that the center of the electrode had increased in thickness by 15%. These are very significant changes when one considers that typical plate thickness values are about 1 mm [9].

Additional knowledge and understanding of transport modes during zinc electrode oxidation can help to provide a solution to the cyclic degradation of the electrode during its service lifetime. Morphological examinations of oxidation processes can help provide information to bridge the knowledge gap. Katan, et al., [17] have shown the usefulness of morphological studies in providing detailed transport mode parameters for silver/silver chloride electrodes. The present study attempted to provide similar morphologically-derived information for the zinc electrode, with the ultimate goal of contributing to the research effort directed toward solving the shape change problem.

B. ELECTRODE CONSTRUCTION [9]

Zinc electrodes historically have been constructed from simple sheet zinc in addition to more complex techniques involving pasting, pressing, and electrodeposition on suitable matrix structures. Procedures vary among manufacturers, but the ultimate goal is to produce a structure that will meet high energy density demand of the contemporary marketplace. Two of the general methods of porous electrode construction will be discussed here as representative of industrial methods. Electrodeposition and pressing will be discussed.

The matrix structure for most porous electrodes is usually copper or silver. The material selected will, of course, be dependent upon the cell service requirements, but normally copper or silver are chosen in woven screen or expanded metal form because of their superior conductivity and acceptable mechanical properties. Expanded metal form is achieved by placing uniformly spaced slots in the metal sheet and then expanding it under tension to produce a uniform pattern. The plate terminal material is usually the same as the matrix material and welded to the matrix in flat strips. Impurity level control is crucial for proper plate performance and reproducibility of performance characteristics from plate to plate; therefore, high purity materials are selected.

The basic material used for application to the matrix or grid structure is high purity zinc oxide. A small amount of mercuric oxide is usually blended with the zinc oxide to raise the hydrogen overvoltage value for the zinc electrode and thus minimize hydrogen generation and concurrent electrode corrosion. The equilibrium potential of a pure zinc electrode can be over 0.4 V more active than that of a hydrogen

electrode in the same KOH solution; this results in the spontaneous oxidation of zinc by the electrolyte, with accompanying reduction of water to produce hydrogen. Small additions of mercuric oxide (amalgamation) make the zinc electrode behave more like mercury than zinc and thus impede this spontaneous reaction with the electrolyte.

The electrodeposition manufacturing method utilizes a plating bath consisting of KOH and deionized water to which the zinc oxide powder has been added. KOH concentration is about 45% by weight. The grid is usually held in place in the plating bath with a Lucite frame, and it is common practice to construct a very long grid for the plating operation and cut it into smaller plates after electroplating. A nickel counter electrode is generally used during the plating operation; after plating to the required specifications the plate is water washed, wet pressed to the desired thickness, and oven dried.

The pressed powder method of manufacture utilizes a cavity mold which is usually constructed from steel and is slightly oversized from the desired electrode plate dimensions. A piece of nonwoven material, such as Viscon paper, is placed in the mold within which the grid is placed. The nonwoven material is cut to sufficient size to allow folding over the grid in an envelope fashion. Zinc oxide powder is then placed on the grid, evenly distributed, and the nonwoven material is folded over the grid and powder. At this point the assembly looks like a closed envelope containing grid and loose powder. A pressing block is then placed in the mold cavity and on top of the plate assembly, to which pressure is applied. After appropriate time, the pressed

plate assembly is removed from the mold cavity and placed in a dilute solution of KOH, usually about 5% by weight. Utilizing appropriate separator materials, a nickel counter electrode is also placed in the KOH; and current is passed through the pressed plate to reduce the zinc oxide and produce zinc. After completion, the zinc plate is removed from the KOH, washed, wet pressed to desired thickness, and dried in a manner similar to that used in the electrodeposit manufacturing process.

Finished characteristics of zinc electrode plates produced by both of the methods described are slightly different, and therefore applications may differ. The electrodeposited plate has a porosity value in the range of 55% to 65% and can be made as thin as 0.25 mm. The pressed powder plate has porosity values ranging from 60% to 70% but can only be made as thin as about 0.7 mm. The electrodeposited plate is considered to be the most rugged of the two and can stand up to more rough handling and abuse during processing and cell construction.

III. EXPERIMENTAL PROCEDURES

A. GENERAL PROCEDURES

This study was conducted as a joint venture with Dr. Ted Katan of the Palo Alto Lockheed Research Laboratory, with all sample preparations and experimental exposures being performed at the Lockheed Laboratory, and microscopic examinations of exposed samples subsequently being accomplished at the Naval Postgraduate School.

Two types of experiments were performed. The first type involved a two-dimensional simulation of a single pore in a porous battery electrode; this experiment was essentially exposure of a very small scale zinc planar electrode. The second type of experiment involved a three-dimensional simulation of a porous electrode; the three-dimensional model was constructed using very small zinc spheres.

B. TWO-DIMENSIONAL EXPERIMENT

The model used to simulate two-dimensional pore behavior comprised a miniature electrolytic cell. An epoxy resin metallographic specimen holder, measuring approximately 2.5 cm in diameter and 1.0 cm in height, served as a structural member to contain embedded cathode, anode and separator components. The cathode and anode were of approximate equal size, with exposed surface approximately 0.6 cm X 1.0 cm after mounting. Separating anode from cathode was a bakelite separator with an exposed surface 0.3 cm X 2.0 cm. The components were embedded in the epoxy holder using standard metallographic cold mounting/casting techniques for epoxy resins such as described in Reference [18]. After

mounting, the top surface, containing anode, cathode and separator, was polished using progressively finer grit hand sanding followed by polishing wheel treatment using progressively finer Al_2O_3 slurries down to 0.05 μm in particle size. The final polishing treatment used cerium oxide as the polishing medium. Polishing was performed to remove any surface irregularities before exposure. After each exposure and subsequent SEM examination, repolishing was performed to prepare the cell for further exposure. After one of these polishing evolutions the zinc anode was etched using Palmetron Reagent for 30 seconds to reveal the base metal grain structure. The grain structure was recorded photographically using a Bausch & Lomb Dynazoom Bench Metallograph and attached camera with Type 405 Polaroid Land Film Holder. A sketch of the cell is shown in Figure 3, and a photograph of the actual cell is shown in Figure 4.

The cell anode was made from 99.99% zinc. Cathodic material was selected mainly based upon availability and convenience since an external impressed current source was used to provide the potential difference between anode and cathode, as opposed to a galvanic cell relationship. Two cells were produced; one of the cells used copper for a cathode while the other cell used zinc for its cathode. The epoxy holder had two 1/16 inch holes drilled in its base, one to the bottom surface of the cathode and the other to the bottom surface of the anode. These holes served to allow electrical connection with external circuitry. The top of the cell was fitted with a 15 μm mylar spacer which framed the circumference of the anodic and cathodic combined area. A glass cover slide sat on top of the spacer thus providing

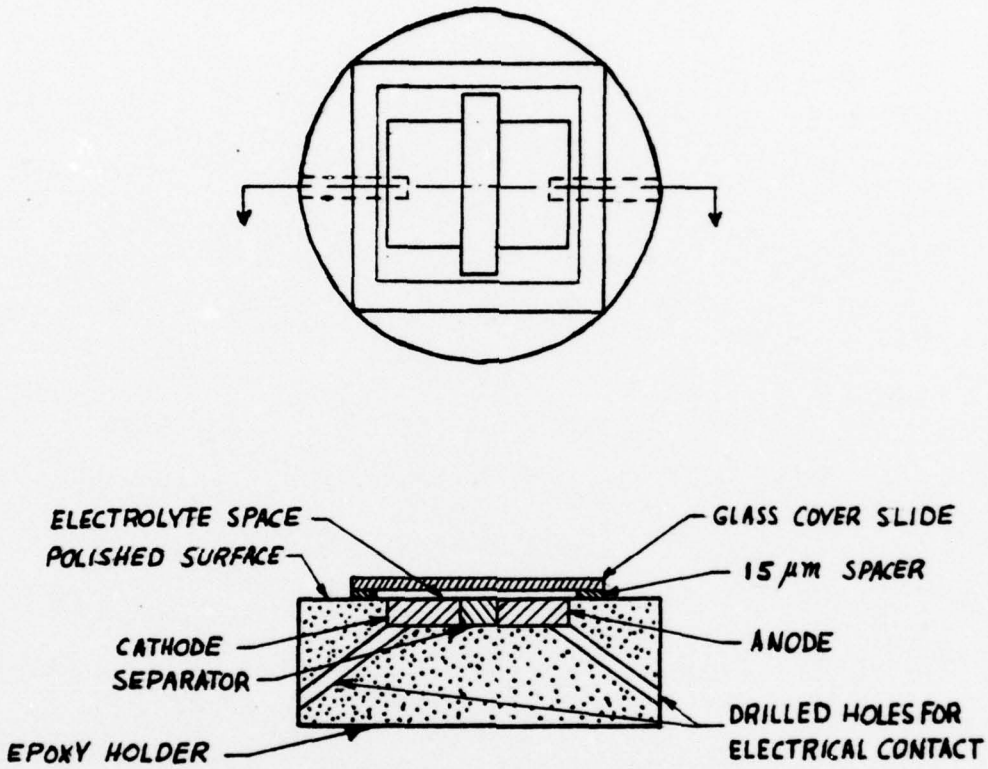

Figure 3. Sketch of two-dimensional cell

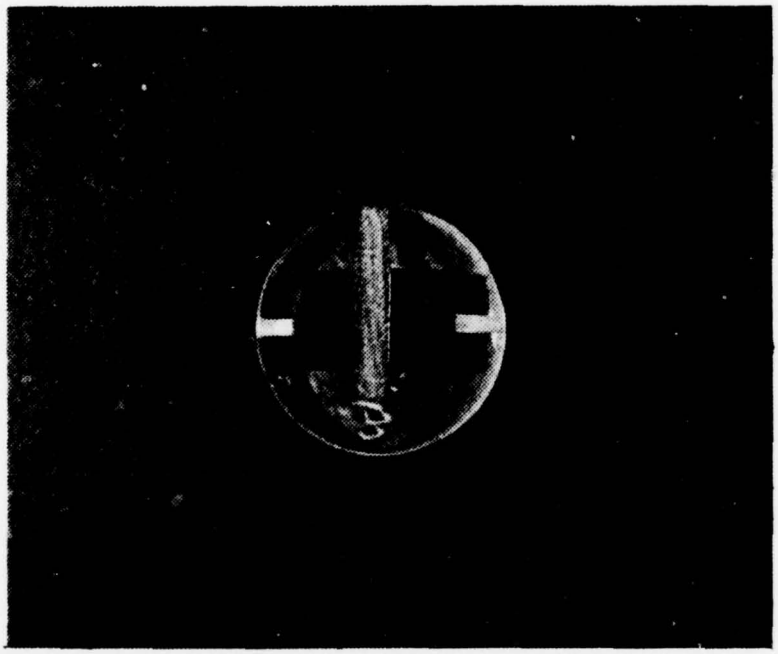

Figure 4. Two-dimensional experiment cell, 1.4X.

a small enclosed volume within which a thin film of electrolyte could cover anode and cathode. The cover slide had a small hole drilled through its center to allow an electrolyte bridge to a Hg/HgO reference electrode from the space between anode and cathode. Anodic potential relative to the reference electrode was measured during exposure, and used as an indicator of passivation. Potential was recorded continuously during runs on a Sargent Model MR Stripchart Recorder. All exposures were made galvanostatically (constant current, varying potential) using either a Princeton Applied Research Model 371 Potentiostat-Galvanostat or an Electronics Measurements Model C612 Constant Current Power Supply. Actual circuit current flow was monitored using a Greibach Instruments Model 510 Milliammeter. A schematic sketch of the experiment circuitry is shown in Figure 5.

The electrolyte used in the experiment was reagent grade KOH diluted to the desired concentration using triple distilled water. The first three runs were conducted using 2.0N KOH. All subsequent runs were conducted with 9.96N KOH saturated with ZnO. The runs using 2.0N KOH were intended as trial runs to demonstrate operability of apparatus and to develop initial reaction profile data. Subsequent runs using 9.96N KOH saturated with ZnO were made to duplicate actual working electrolyte conditions in alkaline silver-zinc batteries. This concentration corresponds to 40% KOH by weight, which is a frequently used value [2]. Electrolyte concentration was verified by titration with 1.00N HCl. Saturation of electrolyte with ZnO was performed by calculating the required amount of ZnO to be added from solubility data in Reference 2 and then adding 1.5 times that amount to the electrolyte to insure

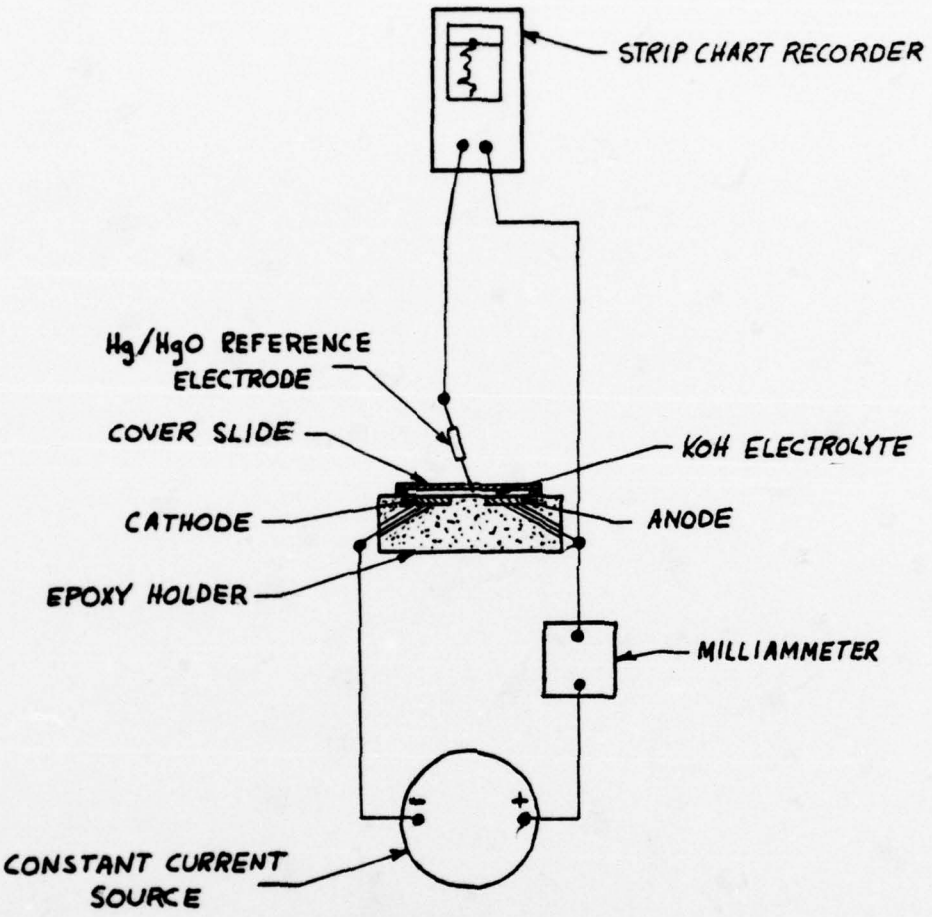

Figure 5. Two-dimensional experiment circuit.

saturation. This procedure was followed as a conservative precaution since ZnO solubility data in the literature lacks agreement from source to source. ZnO saturation is desirable in working electrolytes as a means to reduce the amount of zinc electrode dissolution by the electrolyte.

All runs were conducted at room temperature and at atmospheric pressure. Macroscopic observation of the zinc anode surface during runs was possible through the use of a Bausch & Lomb Stereozoom Model 7 Binocular Microscope. This relatively low power (7X to 100X) instrument was mounted directly over the anodic surface. Initial runs were made using a constant current density and allowing time to be variable. In this manner the cell was given short pulses of current cumulatively until passivation occurred. The cumulative formation of oxidation products was observed directly through the microscope during each pulse. Later runs were conducted by applying a continuous constant current until passivation occurred. Current density values, with respect to total anode area of 0.6 cm^2, were in the range of 1 mA/cm^2 to 10 mA/cm^2. Total cumulative exposure times were usually less than 35 minutes although there was one 98-minute exposure. In all runs passivation was assumed to have occurred when anodic potential values, measured with respect to the reference, were observed to increase unbounded on the strip chart. A typical passivation curve similar to those observed in this study and taken from Reference 9 is shown in Figure 6. In this study passivation is assumed to be defined as the point at which the zinc anode surface is prevented from having any further reaction with the electrolyte due to the complete surface coverage by a passive film.

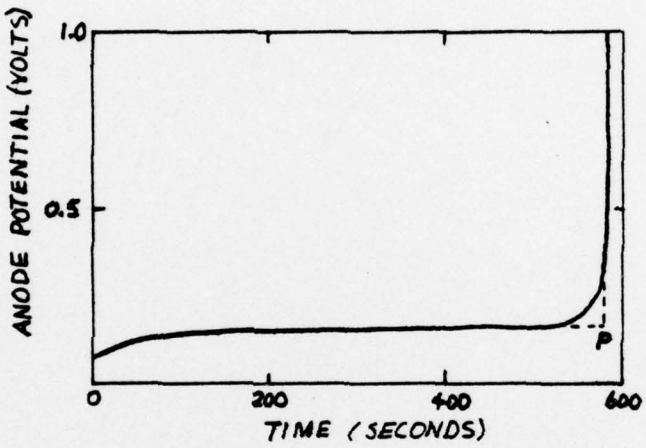

Figure 6. Typical passivation curve for zinc anode (1N KOH, 23.3 mA/cm^2).

During a few runs, after passivation had occurred, fresh electrolyte was added to the cell. This caused a "depassivation" effect to occur which produced visual evidence of a decrease in the amount of oxidation products and also required additional current to be passed in order to reach a new passivation point.

After each run the cell surface was carefully washed several times with triple distilled water and force-air-dried with cold air. The cell was placed in a protective plastic container for later SEM analysis. Cell and plastic container were kept in a desiccator when not being analyzed to minimize moisture effects on the exposed anodic surface. This procedure was followed for all specimens used in this study.

C. THREE-DIMENSIONAL EXPERIMENT

The three-dimensional model used for porous electrode simulation was made of metallic spheres. The use of spherical particles to construct a porous electrode model was successfully reported by Katan, et al., [17] in studies of Ag/AgCl electrodes. Models of this type have a porosity of about 40%. Two types of spherical particles were used in this experiment. One type was derived from 99.5% reagent grade zinc spherical metal dust supplied by the Fisher Scientific Company. These spheres, henceforth referred to as the zinc spheres, had an average diameter of 5.3 μm with an average deviation of 2.4 μm. The second type of spherical particle used was a zinc-plated silver sphere. This type, henceforth referred to as the plated spheres, had a more uniform size distribution and larger average size than the zinc spheres. It was felt that a larger and more uniform size might provide a more uniform current distribution through a spherical particle bed and also

might provide greater ease in SEM analysis. This was only an intuitive feeling, however, and the intention was to use both types of particles and eliminate one if unsatisfactory results were obtained. There were pros and cons for both sphere types. Considerations in favor of using the pure zinc spheres included the possibility of dissolution of the zinc plating on plated spheres, which could lead to uncovering silver and production of complex oxidation products. The plated spheres were originally procured from the Metz Refining Co. and then electroplated with zinc using a cyanide bath and a current density of 0.7 mA/cm^2. Plated spheres had an average diameter of 78.3 μm with an average deviation of 0.8 μm. Plating thickness was determined to be about 1 μm by microtoming individual spheres and making microscopic measurement of resultant cross-sections. Typical zinc spheres and typical plated spheres are shown in Figures 7 and 8 respectively. Microtomed cross-sections of plated spheres are shown in Figure 9.

The original experimental plan was to construct a spherical particle bed of a given thickness, discharge it galvanostatically in KOH, and investigate oxidation product morphology both with regard to its form and type as well as functional dependence on depth. Depth data was to be obtained by slicing the bed into many thin sections after exposure and examining individual section spheres with the SEM. In order to perform this type of experiment, apparatus designed by Katan, shown in Figure 10, and described in Reference 17 was used. Basically the apparatus consists of a truncated hypodermic sytringe housing into which a disc shaped silver stage measuring 1.41 cm in diameter and 0.30 cm in thickness was fitted. The stage was provided with electrical

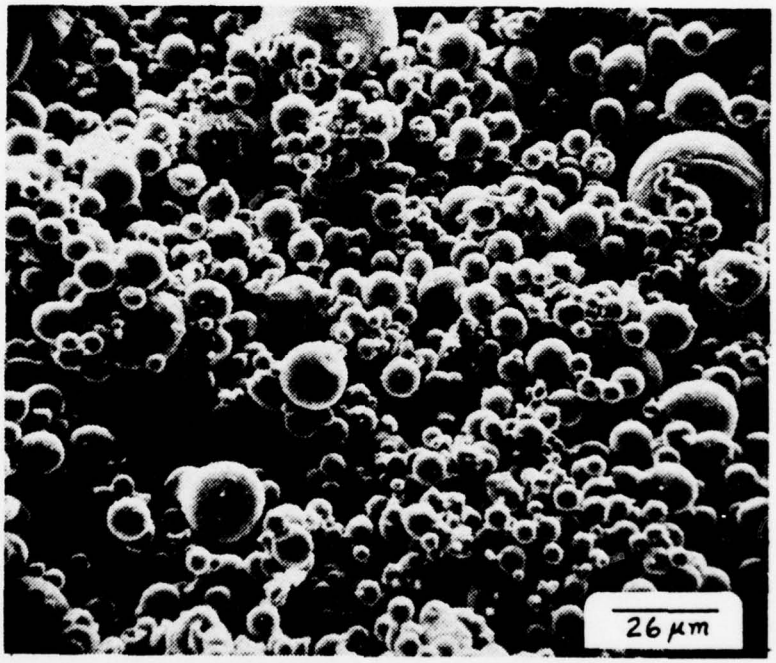

Figure 7. Typical zinc spheres, 580X.

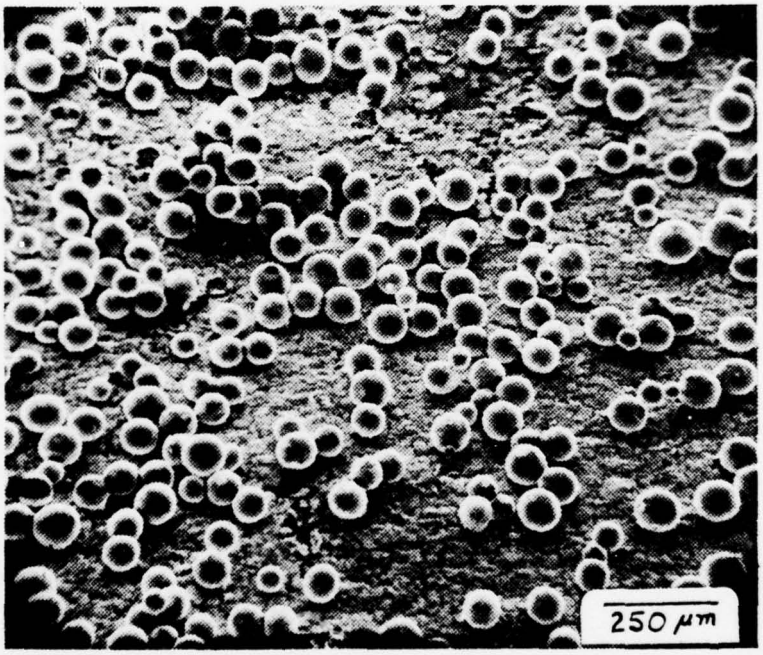

Figure 8. Typical plated spheres, 63X.

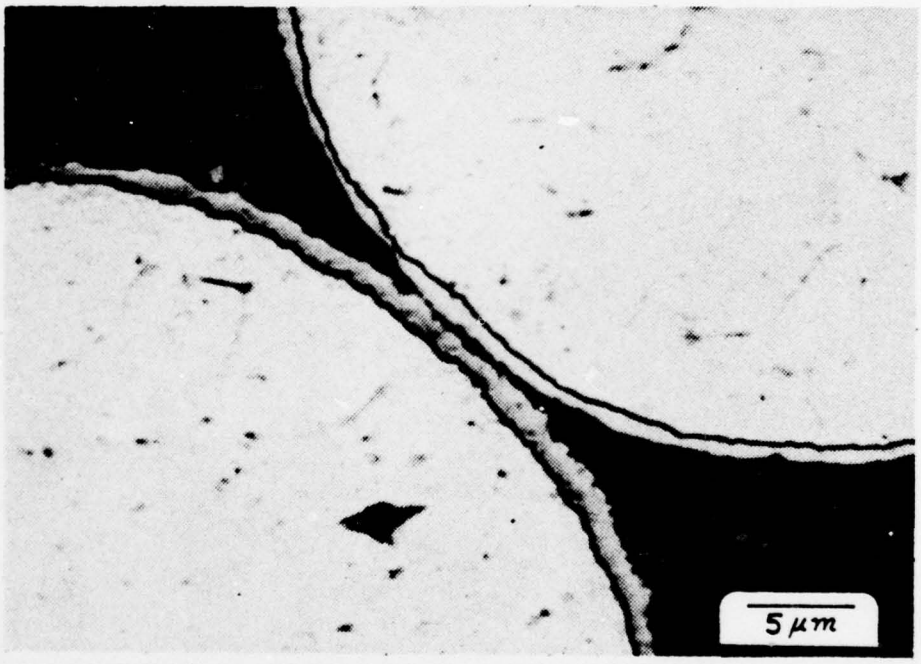

Figure 9. Microtomed plated sphere cross-sections,

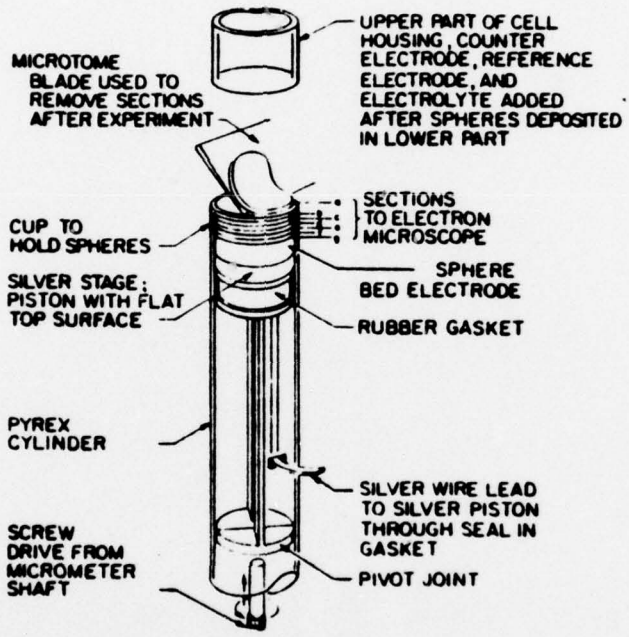

Figure 10. Three-dimensional sphere bed experiment apparatus.

connection to other circuitry through a spot welded silver lead which passed through a rubber gasket below the stage and out the side of the syringe housing. The stage was moveable vertically in the syringe housing, the amount of movement being controlled by rotation of a micrometer shaft which was butted up to the stage bottom. The micrometer allowed stage movements as small as ± 0.0005 cm. The sphere bed was placed on the silver stage. Initially the stage was lowered to accommodate a bed thickness greater than desired. The cylindrical volume defined by the stage top and syringe walls was then filled with spheres. Finally the micrometer shaft was rotated to a predetermined value corresponding to the desired bed thickness, causing upward movement of the stage. The resulting excess spheres which protruded above the top edge of the syringe housing were carefully scraped flush with the top edge using a microtome blade. After obtaining the desired bed thickness, the upper part of the cell housing was joined to the lower housing in a flush fit, and teflon tape was wrapped around the joint making it leak tight. The upper part of the cell was a cylindrical section of identical diameter as the lower syringe housing and containing openings to insert a Ag/AgO counter electrode (cathode) and a Hg/HgO reference electrode. After joining of the two sections, the cell was completed by carefully adding electrolyte with a plastic tube inserted through one of the openings in the upper section in a fashion so as not to disturb the sphere bed. The external circuitry arrangement, shown in Figure 11, was identical to that described for the two-dimensional experiment except that the strip chart recorder was replaced by a Republican Instruments Model 2730 potentiometer for monitoring anodic potential with respect to the reference.

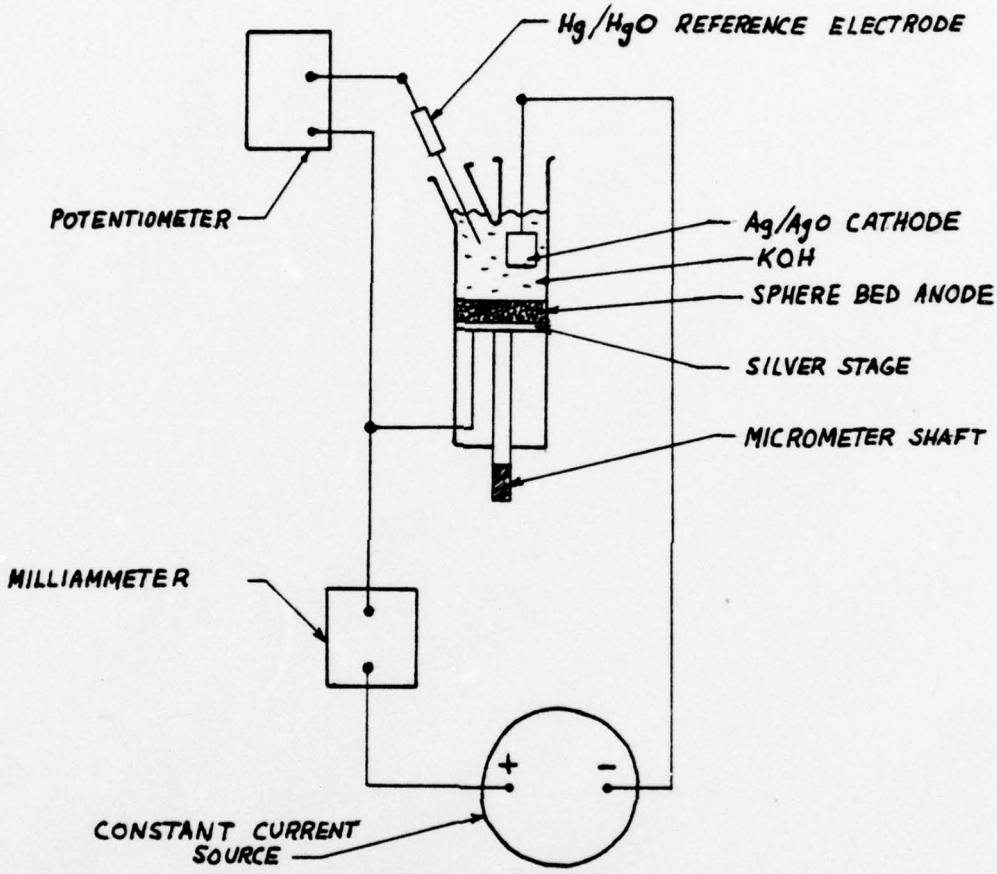

Figure 11. Three-dimensional experiment circuit.

The experiment was performed using a 1.0 cm thick sphere bed composed of zinc spheres. The zinc spheres were initially rinsed in methanol and air dried. They were then placed in 9.96N KOH saturated with ZnO and added as a slurry to the silver stage. After apparatus assembly, 9.96N KOH saturated with ZnO was used to fill the cell. The sphere bed was exposed to a current density of 5 mA/cm^2 for 10 minutes. After exposure, the electrolyte was carefully removed with a plastic tube inserted in the same manner as for filling. The apparatus was disassembled, and the sphere bed was sectioned. Sectioning was accomplished by turning the micrometer shaft to a predetermined setting causing the stage to move up an amount corresponding to the desired section thickness. The protruding spheres were scraped off flush with the top surface of the lower housing into a beaker and rinsed with two 10 cc methanol rinses, following three similar rinses in triple distilled water. Finally the spheres were air dried and transferred to a small vial for later SEM examination. The procedure was repeated for each subsequent section. Section thickness was 0.010 cm for all sections except the first one, which was 0.0050 cm.

SEM analysis of the sectioned layers produced disappointing and inconclusive results. Oxidation products were few, and distinguishable differences from section to section were not apparent. Because of these results, low conductivity of the sphere bed was suspected. Oxidizing individual spheres from section to section is dependent upon adequate conductivity through the thickness of the bed. Thus it was decided to construct a similar bed to the one previously exposed and measure the specific resistance as an indication of conductivity. Specific resistance of such a bed was measured as 23.5 ohm-cm. This is a very high value when compared to the results for a similar bed composed of

silver spheres, for which Katan, et al., [17] report a value of 1.0 ohm-cm. In view of these results, it was assumed that a loose sphere bed of zinc or plated spheres of sufficient thickness to allow a sectioning process would have insufficient conductivity to produce useful results. Thus further attempts with the sectioned electrode were abandoned; and, as an alternative, a similar experiment utilizing a thin or monolayer of spheres was devised.

The monolayer experiment utilized a similar but not identical apparatus to that previously described. Since no sectioning was to be performed, a much simpler cell was utilized which did not incorporate the micrometer adjustable stage of the previous apparatus. The new cell is shown in Figure 12. This new cell used a truncated plastic hypodermic syringe housing fitted with a platinum stage measuring 1.41 cm in diameter and 0.10 cm in thickness. A platinum lead was spot welded to the stage and passed through the rubber seal below the stage for connection to external circuitry. The stage was recessed in its housing approximately 1.0 cm to allow volumetric space for containment of a thin sphere layer as well as electrolyte. Spheres used for the experiment were initially rinsed with methanol, air dried, and then lightly sprinkled on the platinum stage until the stage was barely covered with a very thin layer. KOH electrolyte of 9.96N concentration saturated with ZnO, as before, was carefully added to the recessed volumetric space so as not to disturb the sphere layer. A platinum counter electrode and a Hg/HgO reference electrode were lowered into the electrolyte. External circuitry was arranged in a manner identical to the arrangement used for the sectioning experiment.

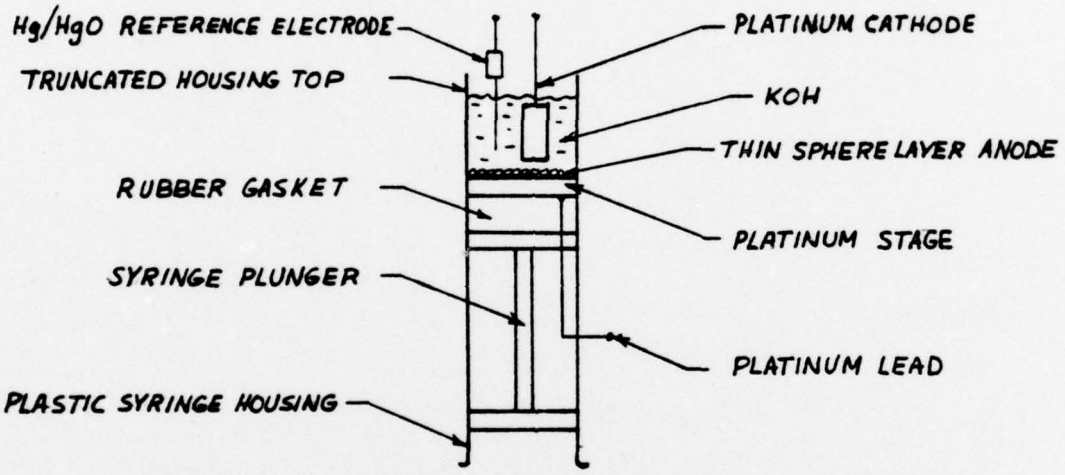

Figure 12. Monolayer experiment apparatus.

Both zinc and plated spheres were used in separate runs of the monolayer experiment. Additionally, one run was made using silver spheres; this run was intended to provide a reference, with which to compare the plated spheres, especially with respect to possible silver oxidation products due to thin or incomplete plating. All runs were made galvanostatically using a constant exposure time of 0.5 minutes. Current density, with respect to the stage cross-sectional area of 1.56 cm^2, was constant for any given run but was varied from run to run, covering a range from 1 mA/cm^2 to 50 mA/cm^2. Anodic potential with respect to the reference electrode was monitored during each run. After exposure the spheres were rinsed at least three times in triple distilled water and given a final rinse in methanol before air drying. The spheres were transferred to individual vials for later SEM examination.

D. SCANNING ELECTRON MICROSCOPE PROCEDURES

The scanning electron microscope (SEM) was the primary analysis tool used in this study. The model used at the Naval Postgraduate School is a Cambridge S4-10 Stereoscan Scanning Electron Microscope, shown in Figure 13. The SEM is a reasonably new research instrument, having been developed in the 1960's. It provides two distinct advantages over previous microscopy techniques. One advantage is the great east of sample preparation. Optical microscopy and transmission electron microscopy (TEM) require time consuming and sometimes quite elaborate sample preparation procedures. In contrast, the normal preparation for the SEM is simply to mount the sample on a special mount that allows the sample to be placed in the instrument's chamber. This mounting

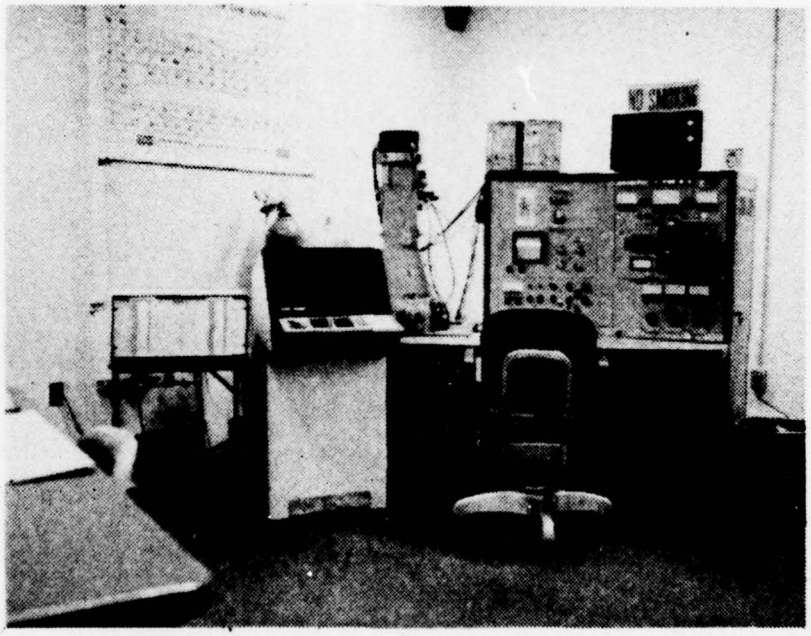

Figure 13. Cambridge S4-10 Stereoscan Scanning Electron Microscope (SEM).

procedure is usually a simple glue or tape procedure requiring minimum time. Another advantage of SEM is its ability to give exellent depth of field at relatively high magnification. Useful magnification for most specimens is in the range of 20X to 12000X, although the instrument is capable of magnification up to 100,000X. Depth of field is rated to be 300 times greater than that of a light microscope when both types are adjusted for optimum performance.

The SEM utilizes a fine probe of electrons to scan the topography of specimens. Scanned areas range from 5 mm to 2 μm depending upon the magnification selected. The resulting three-dimensional appearing image is displayed on a cathode ray tube (CRT). In addition to the image viewing CRT, a second CRT is provided for use in photographic image recording. A Tektronik Oscilloscope Camera Model C-27 equipped with a Polaroid 545 attachment is provided for this purpose. When used with Polaroid Type 55 Positive-Negative Film the user has the capability to produce a quality negative in addition to the print [19]. During this study over 200 photographs were made of selected specimen areas using this equipment. The SEM also has additional capability for elemental analysis. A coupled Princeton Gamma Tech (PGT 1000) energy dispersive X-ray analyzer and software disc storage unit allow detection of X-ray energies associated with electron transitions in the outer shells of material being analyzed. Energy spectrums so derived allow classification of elements contained in the specimen. No major use of this capability was made during this study.

The SEM is capable of being used with either of two different specimen stages. The smaller of the two, known as Type 96172, accepts small specimens up to 3 mm thick which can be mounted on a 12 mm

diameter stub. The larger stage, known as the Multipurpose Stage or Type 96117, is capable of accepting samples up to about 1 cm in thickness which can be mounted on a 3 cm diameter stub. Both stubs allow the specimen to be plugged simply into the appropriate stage for analysis after mounting. The Multipurpose Stage is capable of many other uses, as its name implies; however, these other capabilities were of no concern to this study. Both stages allow specimen translation during analysis in x, y and z directions, rotation through 360 degrees and changes in the viewing angle of incidence from 0 to 90 degrees.

Both stages were used during the study. The small stage was utilized for analysis of spherical particles associated with three dimensional experiments while the large stage was used for analysis of two-dimensional experimental results. Mounting of spherical particle specimens on the small stage stub was accomplished by painting the stub face with silver conductive paint (using a very thin coat) and carefully sprinkling the loose spheres directly on the painted surface. Mounting of two-dimensional experiment specimens was accomplished by mounting the entire epoxy holder as a unit on to a large stage stub. This was done by gluing the holder to the stub with silver conductive paint after inserting short electrical leads into the drilled passages to provide a ground path for the electrodes to the stub. The advantage of using the large stage for this size of specimen was obvious. Without the benefit of a large stub the anode would have been required to be removed from the epoxy holder at the expense of possible damage to oxidation products.

During subsequent operation of the SEM and analysis of the two-dimensional experiment specimens, resolution degradation was encountered associated with local charging of the epoxy holder surface and some areas of oxidation product growth. After much experimentation a layer of gold (40 angstroms thick) was placed on the entire surface of the specimen using a vacuum deposition chamber. This provided a grounding path for these localized ungrounded areas without destroying any of the sample topography. This proved to be a solution to the resolution problem. All subsequent two-dimensional experiment specimens were gold coated in the same manner.

IV. EXPERIMENTAL RESULTS AND DISCUSSION

A. TWO-DIMENSIONAL EXPERIMENT RESULTS

The series of two-dimensional experiments provided two general types of results: reaction penetration profiles and morphological observations. Penetration profiles give a general insight into the depth of anode pore necessary for anodic oxidation reactions to take place effectively; anode pore depth information is useful in determining the correct thickness for zinc electrode manufacture. Morphological information provides a means through which basic ideas relative to anodic oxidation reaction mechanisms can be formulated. Appendix A contains experimental data for two-dimensional experiments.

1. Penetration Profile Results

During the first six experiments with the two-dimensional cell, anodic oxidation product penetration, measured as distance from the separator, was observed concurrently with the binocular microscope. Penetration distances were observed to increase as a function of increasing current-time product up to a limiting, or saturation, value; beyond this point no increase in penetration distance was observed. This indicated that the zinc anode had a finite depth beyond which no further appreciable charge accumulation or oxidation reaction took place; in other words, the reaction was limited to a certain depth. This value was observed to be in a range from 0.88 mm to 2.40 mm, depending upon the specific current density applied during the experiment. The most frequently observed value was 1.35 mm, corresponding to runs at 1.67 mA/cm^2.

In order to verify the microscopically derived penetration distance values using a different technique, Experiment #3 of the two-dimensional series was performed; in this experiment a previously oxidized anode was reduced, one rectangular strip of area at a time, to determine a reaction profile. This was accomplished by tape masking all of the anodic area except for a small strip next to the separator, for which the section width (penetration distance) was known. The small strip was then galvanostatically reduced in KOH until hydrogen gas was generated from the electrolyte, indicating that all of the anodic oxidation product had been reduced. Knowing the current and time needed to reach this point, charge transferred was known. Continuing the experiment in a like manner, reducing subsequent small strips of anodic area from the previously masked anode, one by one, until the entire anode had been reduced, provided data to construct a profile of charge transferred versus distance from the separator (penetration distance). This type of procedure for obtaining penetration profiles has been reported by Szpak and Katan [15] for silver electrodes.

The reaction profile obtained by the strip reduction method is shown in Figure 14. This profile shows that the largest amount of charge transfer for reduction was required when closest to the separator; this is logical since the largest accumulation of oxidation product was observed to occur closest to the separator and would require a large current-time product for reduction. Moving further away from the separator, a smaller accumulation of oxidation product was encountered, and thus the charge required to reduce it should be smaller, as

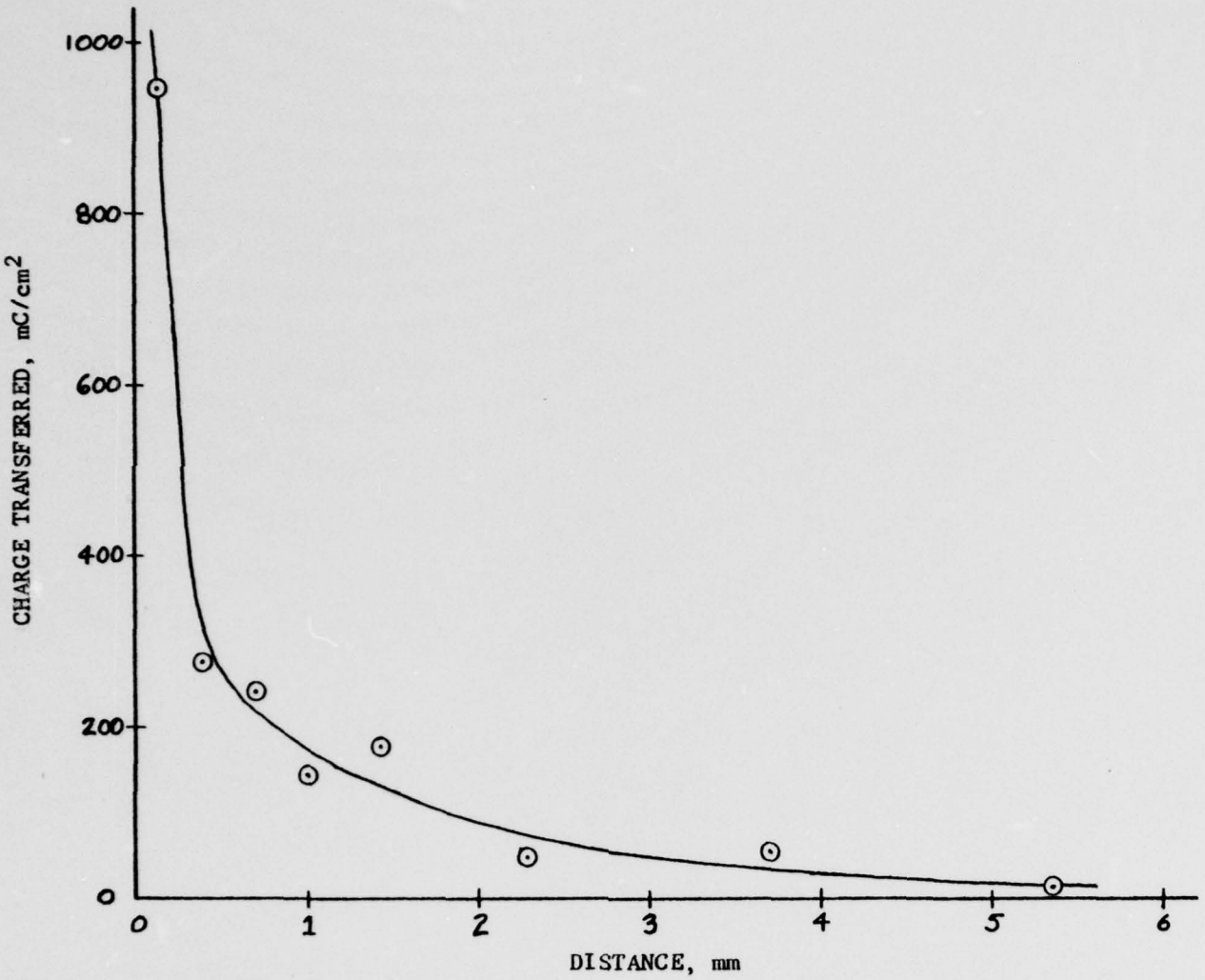

Figure 14. Charge transferred to reduce zinc anode oxidation film as a function of distance from separator.

shown in the figure. Without resorting to any elaborate quantitative interpretation procedures, it can be observed that the majority of the charge transferred is confined to about the first 2 mm or less. Beyond that distance there is very slight additional contribution. This essentially means that the anodic oxidation product is mainly confined to the first 2 mm of anode depth; thus most oxidation reactions are also confined to this limit or less. This is consistent with visual observations of penetration depth in the range of 0.88 - 2.40 mm.

2. Oxidation Morphology

Morphological data are a direct result of microscopic examinations of oxidized zinc anodes, using the SEM as a primary tool of analysis. As an aid for reader assistance, Figure 15 describes anodic locations where microscopic data were collected. All microscopic data from two-dimensional experiments have been identified with respect to the anodic region where obtained, in accordance with Figure 15.

Figures 16 and 17 provide references which allow identification of characteristics typical to the unexposed zinc anodes used in the two-dimensional experiments. Figure 16 shows a polished anodic surface which has a surface texture characteristic of the pre-exposed condition. This figure is particularly useful to the reader for comparison with exposed samples, in order to distinguish oxidation products from base metal The few lines observable on the anode surface in Figure 16 are polishing marks. Figure 17 reveals the grain structure of the anode; average grain diameter was determined to be 50.46 μm, and the

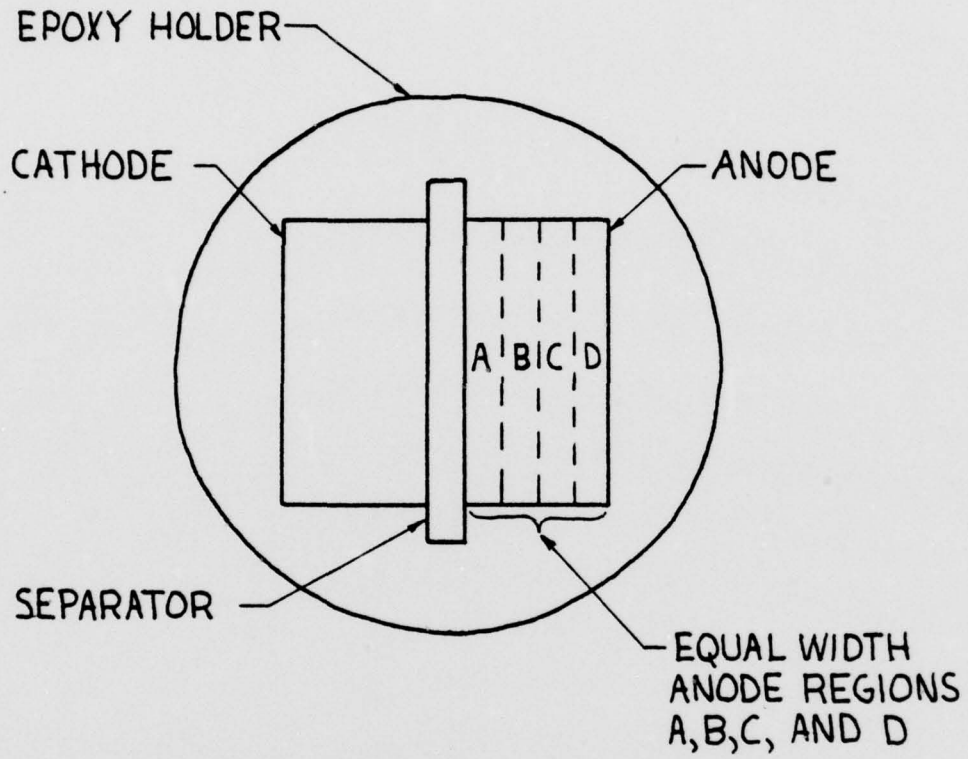

Figure 15. Two-dimensional cell anode region designations used during SEM observations.

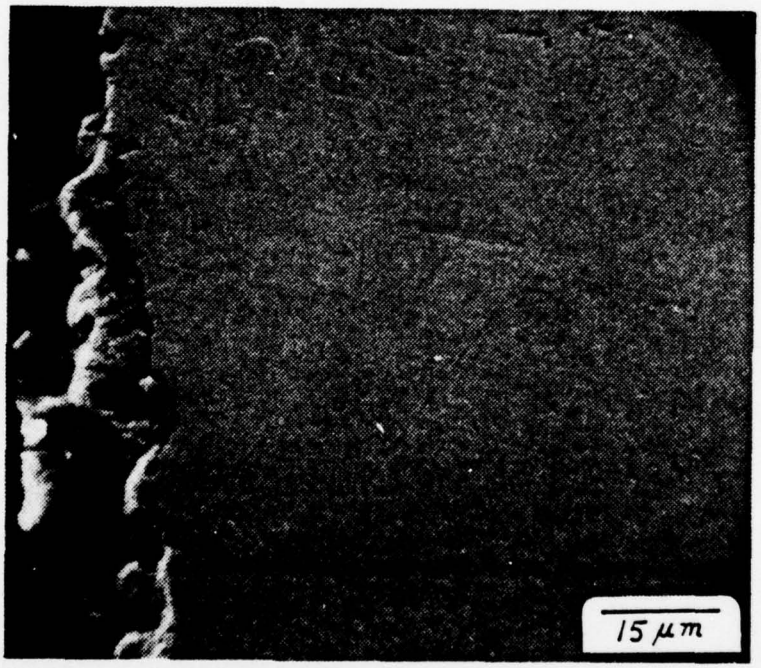

Figure 16. Polished zinc anode surface, prior to exposure, region A adjacent to separator, 1120X.

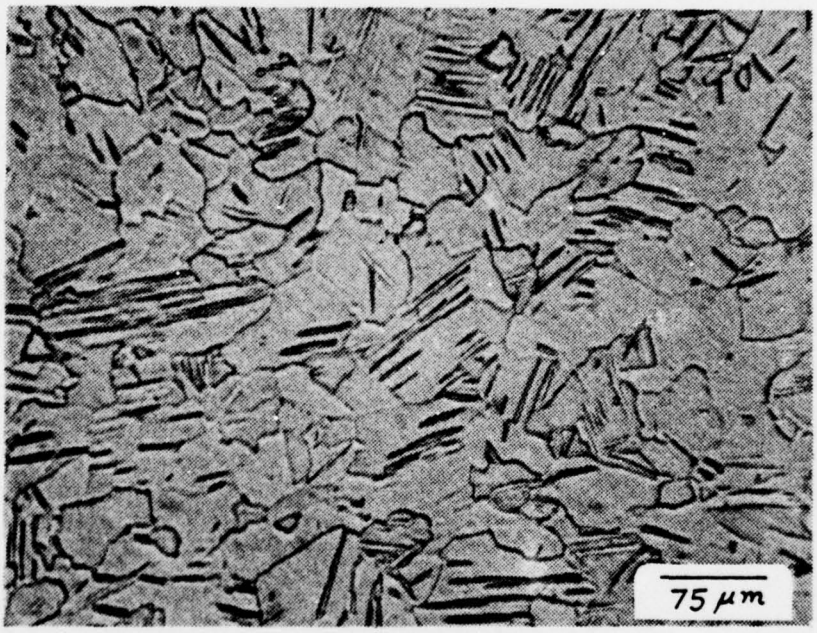

Figure 17. Zinc anode, region A, polished and etched to reveal grain structure, 200X.

average number of grains per unit area was found to be 2.82×10^4 grains/cm^2. Within grains, parallel bands may be noted, which are known as twins.[1]

Figures 18-22 show the result of low current-time product exposures of a zinc anode. In this series of figures very little oxidation product is observable; the main effect observed is strong etching/pitting that is the result of zinc dissolution. This indicates that production of oxidation products requires some minimum threshold current-time product; similar results were shown by Luebke [21] who reported minimum current-time product values necessary for oxidation product coatings on zinc anodes in sea water. The influence of distance from the separator upon the amount of etching/pitting is evident from observations made during movement from the separator outward, as in Figures 18-22. This is another indication of diminishing reaction rate with distance of penetration. Average pit size was measured as 4.0 μm, and average pit density was found to be 9.1×10^5 pits/cm^2. Pitting is the first visible step in the zinc anode oxidation process. Since zinc oxidation products are soluble in KOH, pitting without visible oxidation products is evidence that the rate of oxidation product dissolution exceeds the formation rate; thus the electrolyte is receiving the products of oxidation as zincate ions. This analysis is in agreement

---

[1]Twinning is a phenomenon associated with regional changes in orientation within individual crystals due to plastic deformation; mechanical working and annealing or recrystallization are frequent causes. Internal stresses set up during quenching or casting are sometimes sufficient to induce annealing twins upon subsequent heating [20]. Preferential attack by etchant results in revealing these bands; similar preferential attack occurs at grain boundaries.

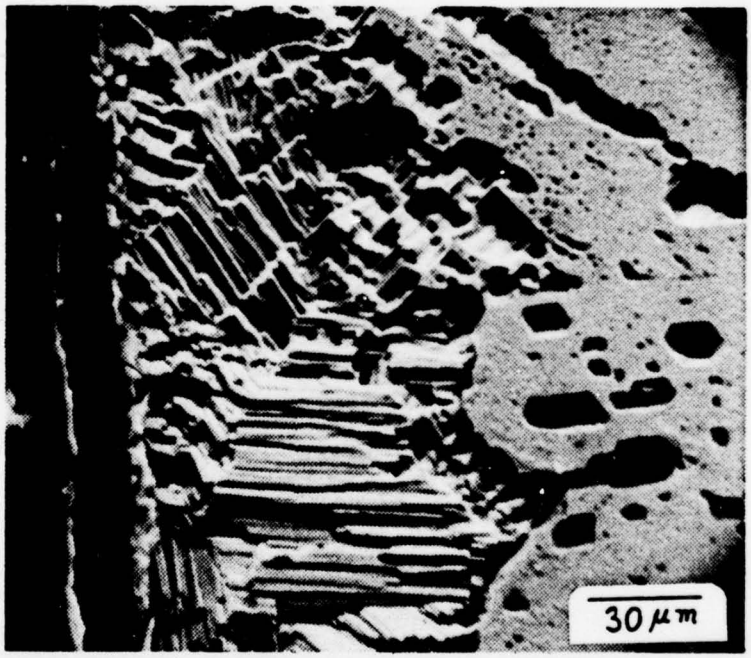

Figure 18. Heavily pitted zinc anode, region A; 10 minutes at 1.67 mA/cm^2 in 9.96N KOH, 520X.

Figure 19. Heavily pitted zinc anode, region A, 0.1 mm from separator; 10 minutes at 1.67 mA/cm^2, 520X.

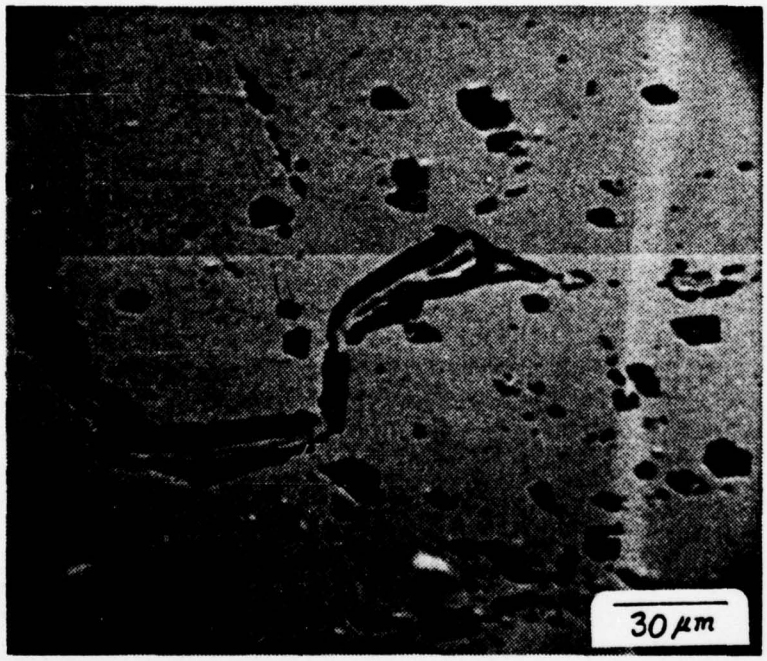

Figure 20. Zinc anode, region A, 0.25 mm from separator; local large pits and possible grain boundary etching; 10 minutes at 1.67 mA/cm^2 in 9.96N KOH, 520X.

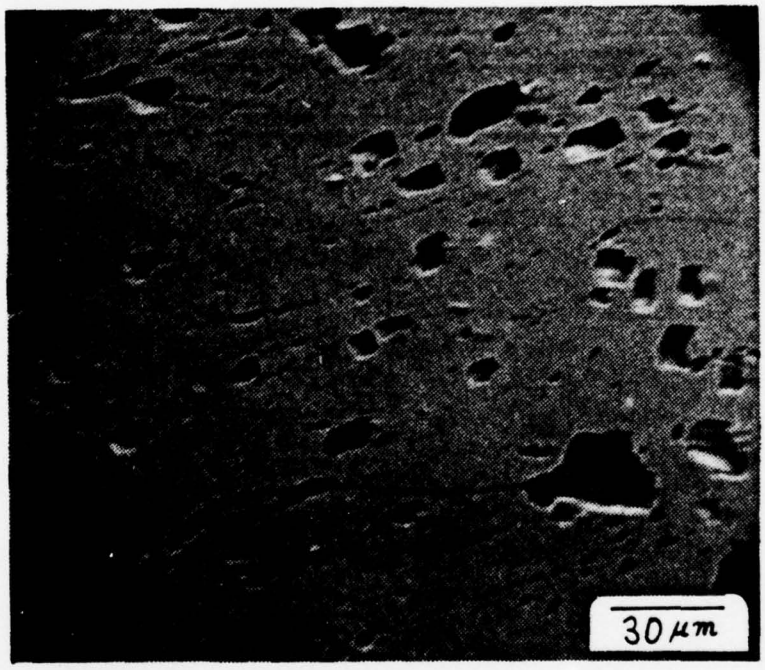

Figure 21. Zinc anode, region A, 0.75 mm from separator; assortment of various pit sizes; 10 minutes at 1.67 mA/cm^2 in 9.96N KOH, 520X.

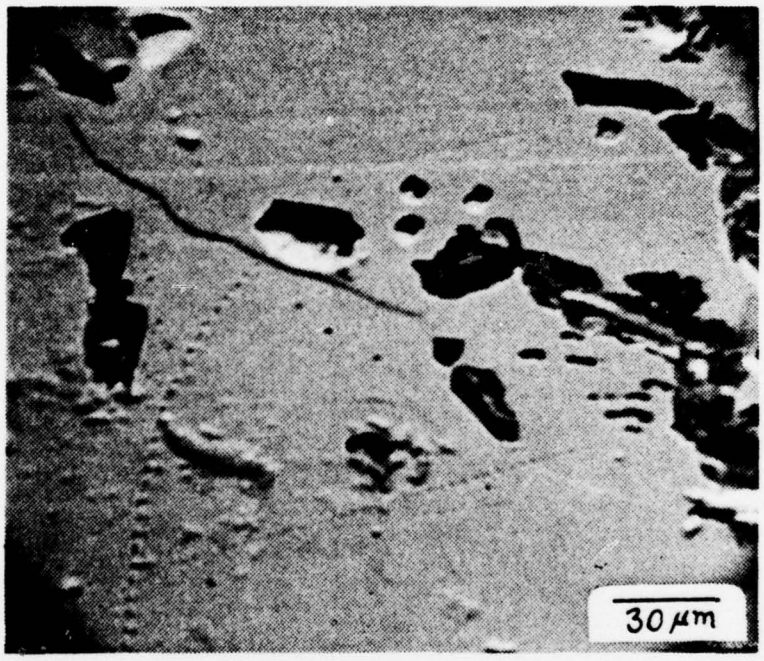

Figure 22. Zinc anode, region D, adjacent to outside edge; deep pits resulting from edge effects; 10 minutes at 1.67 mA/cm^2 in 9.96N KOH, 510X.

with the literature, which indicates that KOH electrolytes are capable of accepting zincate up to a point of supersaturation.

Figure 22 shows large pits close to the outside edge of the anode. These results are indicative of anodic edge effects and represent a geometric limitation of the two-dimensional model. Edges of the anode tended to have unpredictable and non-uniform current distributions, leading to spurious reaction rates; for this reason, edge data were generally disregarded.

The etching/pitting observed generally shows a definite geometric pattern. In Figure 18, the zinc dissolution has occurred in such a manner as to reveal individual grains and specific planar orientations within each individual grain. At least three grains are easily visible in Figure 18 due to the different slip plane directions revealed for each grain by etching action. The straight and parallel slip planes revealed within each grain are characteristic of the zinc lattice structure. Zinc has a hexagonal close-packed space lattice and deforms along one family of planes, those parallel to the base plane of the hexagonal prism; these planes are known as basal planes. The basal slip planes are apparently preferentially attacked by the electrolyte during anodic dissolution. Preferential attack is also seen at grain boundaries; an example is the S-shaped grain boundary "canyon" seen in Figure 20. Grain sizes revealed by etching in Figures 18-20 correlate favorably with the average grain size previously reported for Figure 17.

Figures 23-29 show oxidation product growth on the zinc anode. This series of photographs reveals the heaviest oxidation accumulation

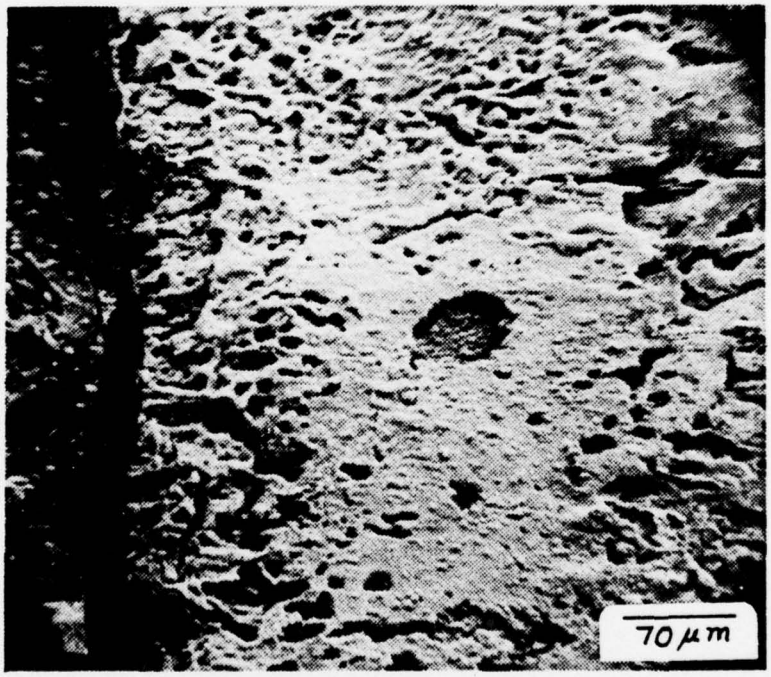

Figure 23. Zinc anode, region A, next to separator; heavy oxidation product layer covering pitted surface; 21 minutes at 1.67 mA/cm^2 plus 12 minutes at 6.67 mA/cm^2 in 9.96N KOH, 220X.

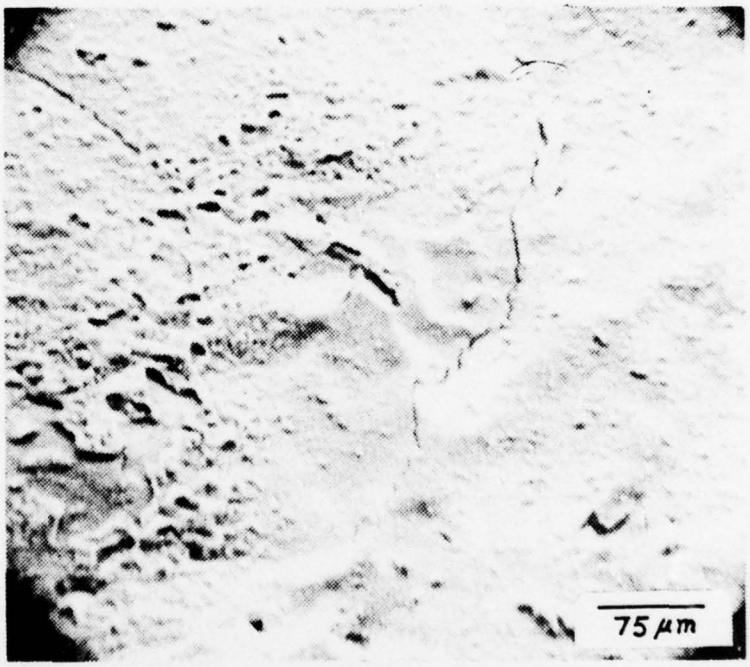

Figure 24. Zinc anode, region B, 1.5 mm from separator; thick oxidation product layer showing partial cracking; 21 minutes at 1.67 mA/cm^2 plus 12 minutes at 6.67 mA/cm^2 in 9.96N KOH, 200X.

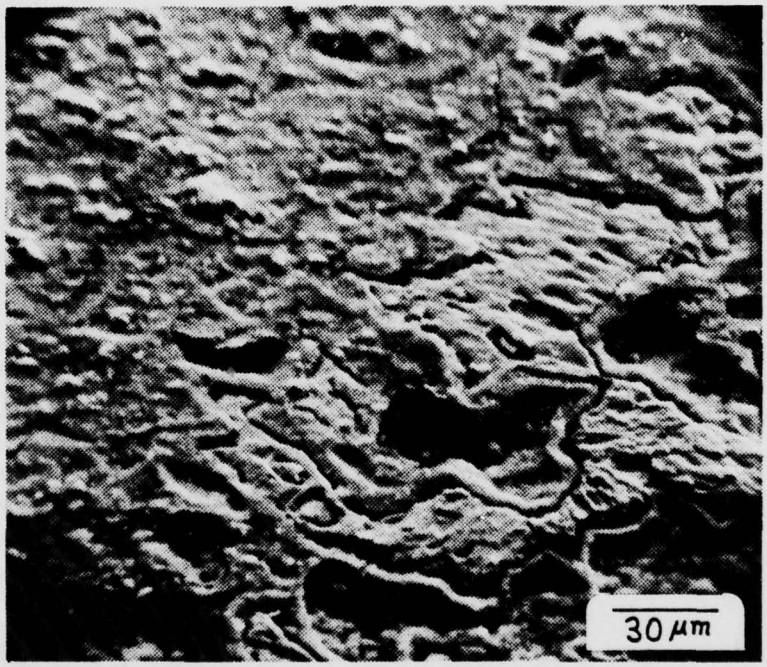

Figure 25. Zinc anode, region B, 1.9 mm from separator; edge of dense oxidation layer showing pits which are not completely covered by oxidation product; 21 minutes at 1.67 mA/cm^2 plus 12 minutes at 6.67 mA/cm^2 in 9.96N KOH, 550X.

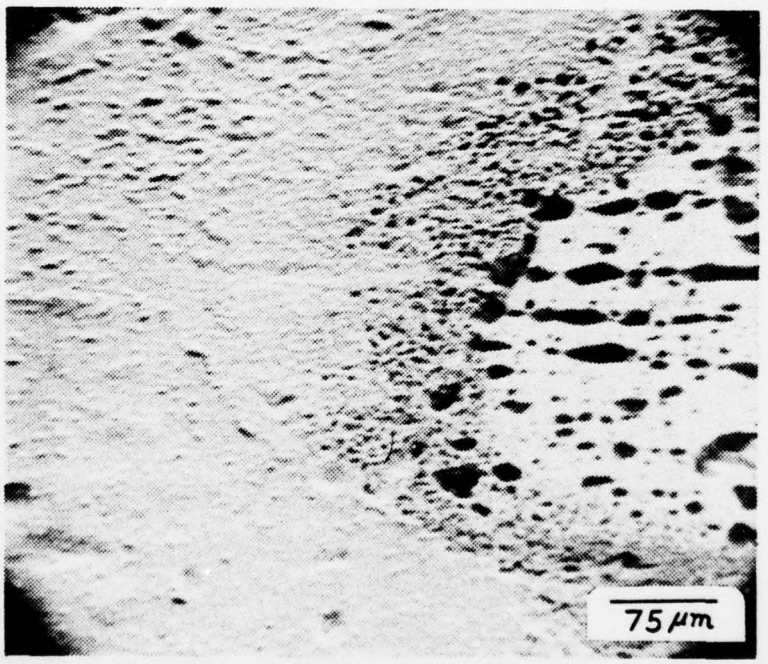

Figure 26. Zinc anode, region B, 2.0 mm from separator; boundary between oxidation product layer and bare, pitted zinc surface; 21 minutes at 1.67 mA/cm^2 plus 12 minutes at 6.67 mA/cm^2 in 9.96N KOH, 200X.

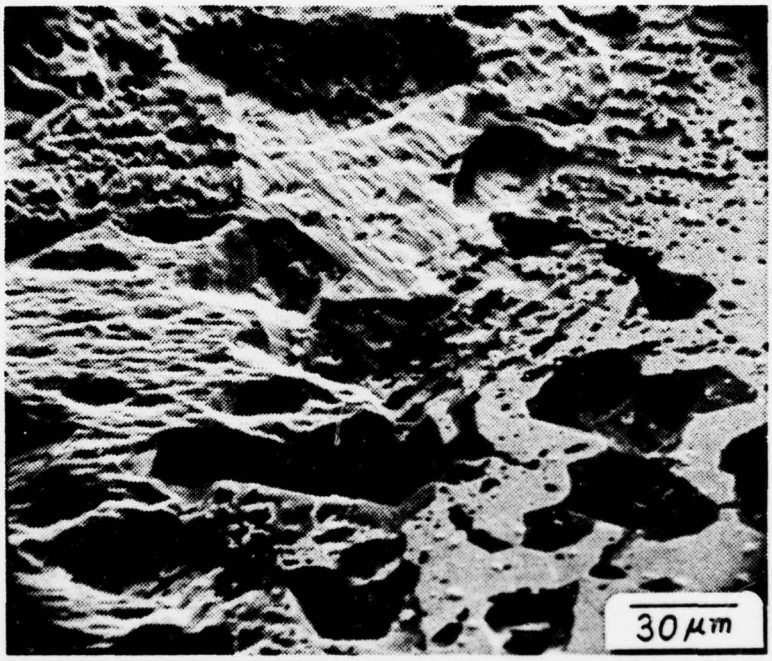

Figure 27. Zinc anode, region B, 2.15 mm from separator; oxidation product layer edge next to pitted bare zinc surface; oxidation products just starting to cover pits; 21 minutes at 1.67 mA/cm^2 plus 12 minutes at 6.67 mA/cm^2 in 9.96N KOH, 550X.

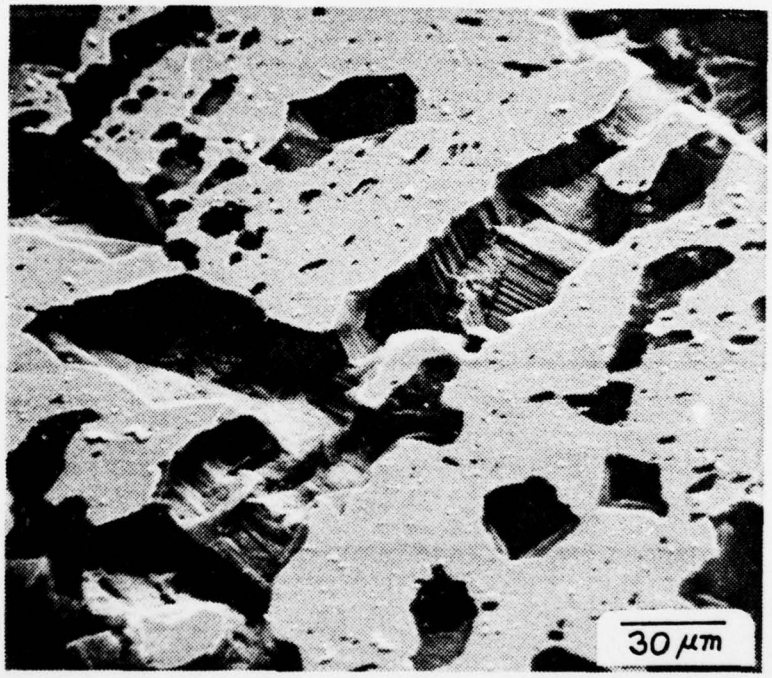

Figure 28. Zinc anode, region B, 2.4 mm from separator; bare surface pits and small precipitate oxidation product particles at sites near pits; 21 minutes at 1.67 mA/cm^2 plus 12 minutes at 6.67 mA/cm^2 in 9.96N KOH, 550X.

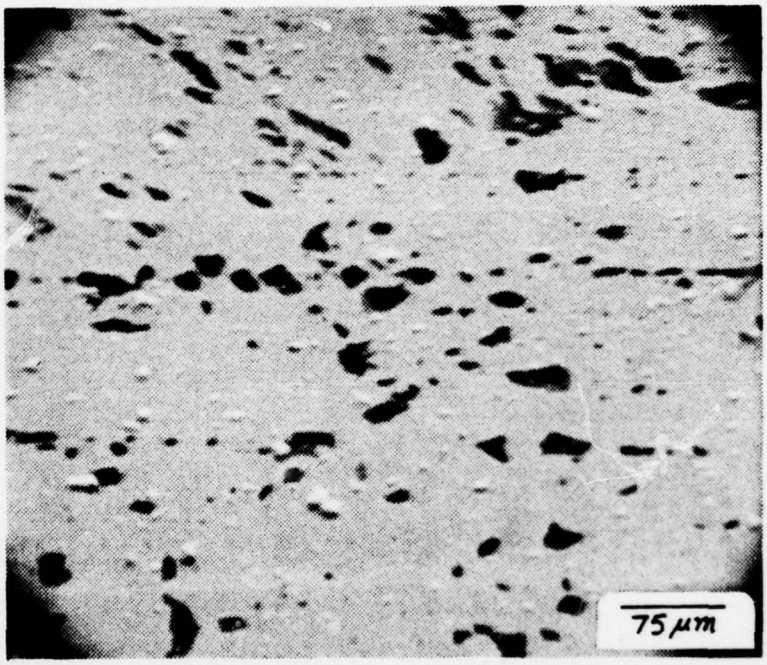

Figure 29. Zinc anode, region D, 5.0 mm from separator; etch pits and surrounding nucleation sites of oxidation products; 21 minutes at 1.67 mA/cm^2 plus 12 minutes at 6.67 mA/cm^2 in 9.96N KOH, 200X.

next to the separator and a diminishing amount of product as one moves outward from the separator, until the bare, pitted zinc surface is revealed; these results are in agreement with the profile of Figure 14 discussed previously. In Figure 23 two types of oxidation product are observable; there is a heavy, cracked, crusty layer through which holes appear to lead to underlying pits, which remain as active sites for oxidation reactions; there is also a product which appears to have been sprinkled lightly on top of the crusty layer and is lighter in color than the crusty layer. The same general product characteristics are evident in Figure 24. Figure 25 shows the edge of the dense, crusty layer, and large pit sites appear to be partially uncovered. Figure 26 shows a distinct boundary between oxide covered surface and bare, pitted base metal. It is significant to note that the penetration distance for this interface in Figure 26 is 2.0 mm, which correlates with zinc anode penetration distances previously discussed.

The two distinctly different types of oxidation product are evident in Figure 27; on the bare, pitted zinc surface (right side of Figure 27) there is a sprinkling of small, white particles, 1 μm to 2 μm in diameter; on the left side, however, the oxide product is an even, complete, adherent coating that assumes the shape of the underlying surface. These two different types of oxidation products were encountered on most samples studied. Powers [22] has identified these two products as types of ZnO, referring to the white particles as Type I ZnO and the adherent coating as Type II ZnO. In most observations the even and adherent oxidation product was darker in color than the loose, flocculent white particles which comprised the other type of product. Because of this color differentiation, it was decided to

refer to the products as "gray product" and "white product." The gray product actually took on a range of colors from light gray to nearly black; it had an estimated thickness varying from about 0.2 μm to 5 μm, depending upon its location; thicker locations were generally closest to the separator.

Since the gray product always appeared as a tightly adherent surface coating, in many cases assuming the contours of the underlying surface, it is believed that this product results from a direct reaction between metal and electrolyte, in which the product is formed very close to the reaction site. The white product however, always appeared as if it had fallen down upon the surface in a shower from the electrolyte, implying that a precipitation mechanism was responsible, with deposition at sites not necessarily next to corresponding dissolution sites. Dissolution of zinc oxidation products in KOH, producing the complex zincate ion, is well documented and the precipitation of white product is probably associated with local supersaturation of the electrolyte with zincate at individual locations. Zincate concentration gradients, which are known to exist in porous electrode structures, play an important part in the overall zinc oxidation process and are the subject of numerous research efforts in the literature. Similar conclusions regarding precipitation mechanisms for deposit of white product have been reported by Powers [22,23], Nagy and Bockris [24], and others who have studied zinc anode behavior in alkaline electrolytes. It should be pointed out that white product appeared on almost all anodic samples used in this study. Generally the oxidized sample surfaces had white product alone or a combination of white product and gray product; there were no cases in which gray product appeared by itself.

Figures 28 and 29 are representative of white product which appeared directly on the zinc anode surface without any gray product; particle density was determined to be 7.7×10^4 particles/cm^2 from Figure 29. Figures 30-34 show surfaces covered by both white and gray products; the faceted, etched zinc anode surface is visible below the oxidation products in these figures. White products in some locations were lumped together forming clusters with diameters as large as 10 μm, while the gray layer was about 1 μm thick. In Figures 33 and 34, oxidation products are beginning to "flow" into faceted, stepped shaped pits from adjacent oxidation layer covered surfaces. It was observed that pit sites were the last part of a sample surface to be covered by oxidation product. The reason for this behavior is concluded to be due to pit sites being major suppliers of zinc ions during the oxidation process; as such, these sites are actively pumping out zinc ions which subsequently participate in oxidation product formation reactions. As the buildup of oxidation product closes in on a pit site, some undercutting of adjacent oxidation layers usually occurs. This undercutting process is evident in Figures 35-37. Eventually, as exposure continues, some pit sites are filled in, producing a smooth surface resembling hill and valley land topography, as the gray product layer assumes the contours of pits and high spots below it. Figure 38 shows an example of this end result with "hill" elevations approaching 7 μm.

If the surface texture of a smooth layer, which has covered pit sites, is examined closely, it is found to have a "furry" texture resembling a carpet surface; Figures 39 and 40 show this texture. Nagy

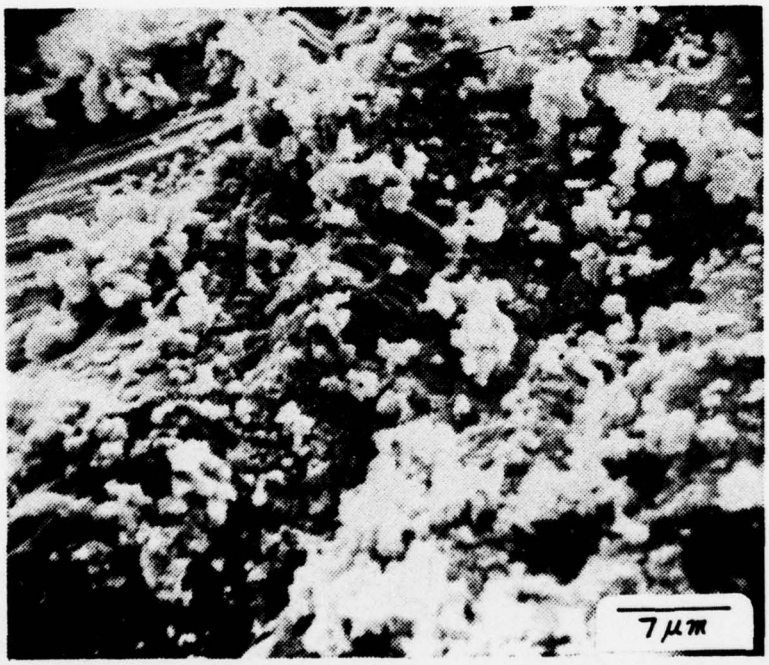

Figure 30. Zinc anode, region A; faceted pit which has been partially covered by both gray and white oxidation products; 17.5 minutes at 6.67 mA/cm^2 in 9.96N KOH, 2300X.

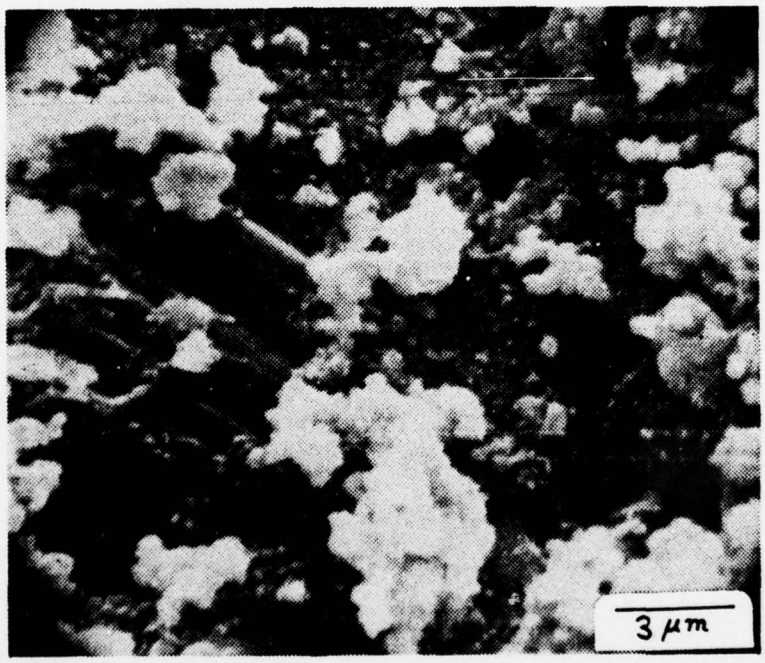

Figure 31. Zinc anode, region A; closeup of gray and white oxidation products which have partially covered a faceted pit; 17.5 minutes at 6.67 mA/cm^2 in 9.96N KOH, 5700X.

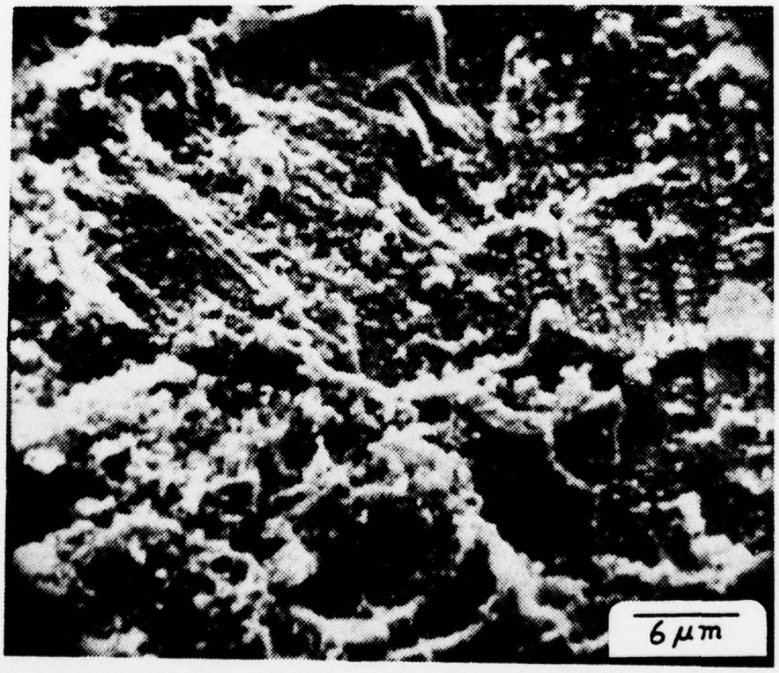

Figure 32. Zinc anode, region B; faceted pits covered by a thin gray oxidation layer over which there appears an incomplete layer of white oxidation product; 15 minutes at 10 mA/cm^2 in 9.96N KOH, 2500X.

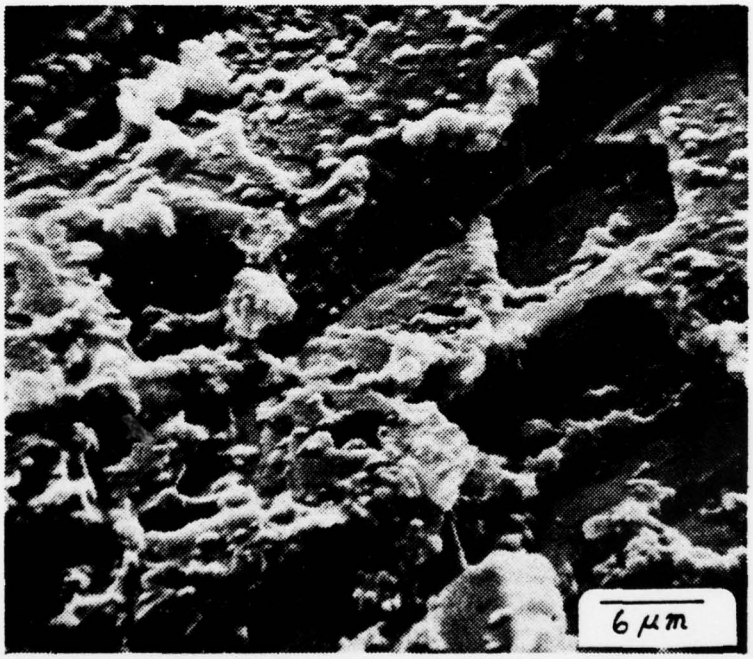

Figure 33. Zinc anode, region A; view of geometrically shaped pits within faceted base metal structure; oxidation product growth beginning to flow into pits; 17.5 minutes at 6.67 mA/cm^2 in 9.96N KOH, 2400X.

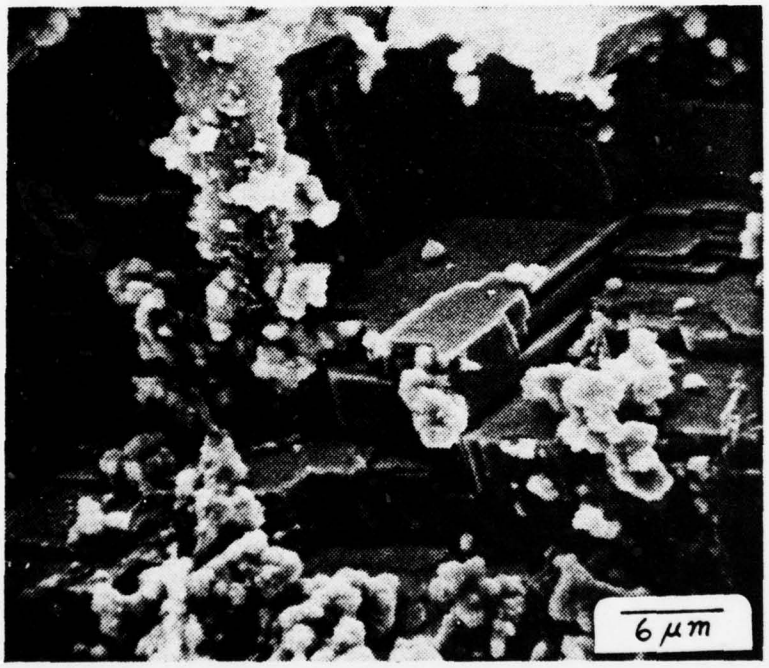

Figure 34. Zinc anode, region A; view within faceted pit showing growth of both gray and white oxidation products; 17.5 minutes at 6.67 mA/cm^2 in 9.96N KOH, 2400X.

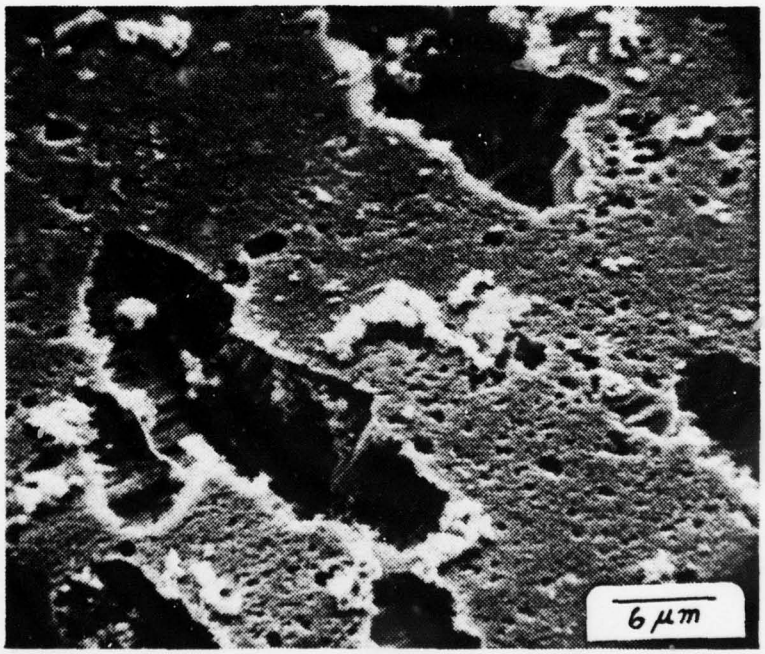

Figure 35. Zinc anode, region B; closeup view of etch pits showing corrosive undercutting and growth of gray oxidation layer over pit edges; white oxidation product nucleation sites visible close to pits; 15 minutes at 10 mA/cm^2 in 9.96N KOH, 2400X.

AD-A045 134 NAVAL POSTGRADUATE SCHOOL MONTEREY CALIF F/G 10/3
SCANNING ELECTRON MICROSCOPE STUDY OF POROUS ZINC BATTERY ELECT--ETC(U)
JUN 77 J R SAVORY

UNCLASSIFIED NL

2 OF 2
AD
AD045134

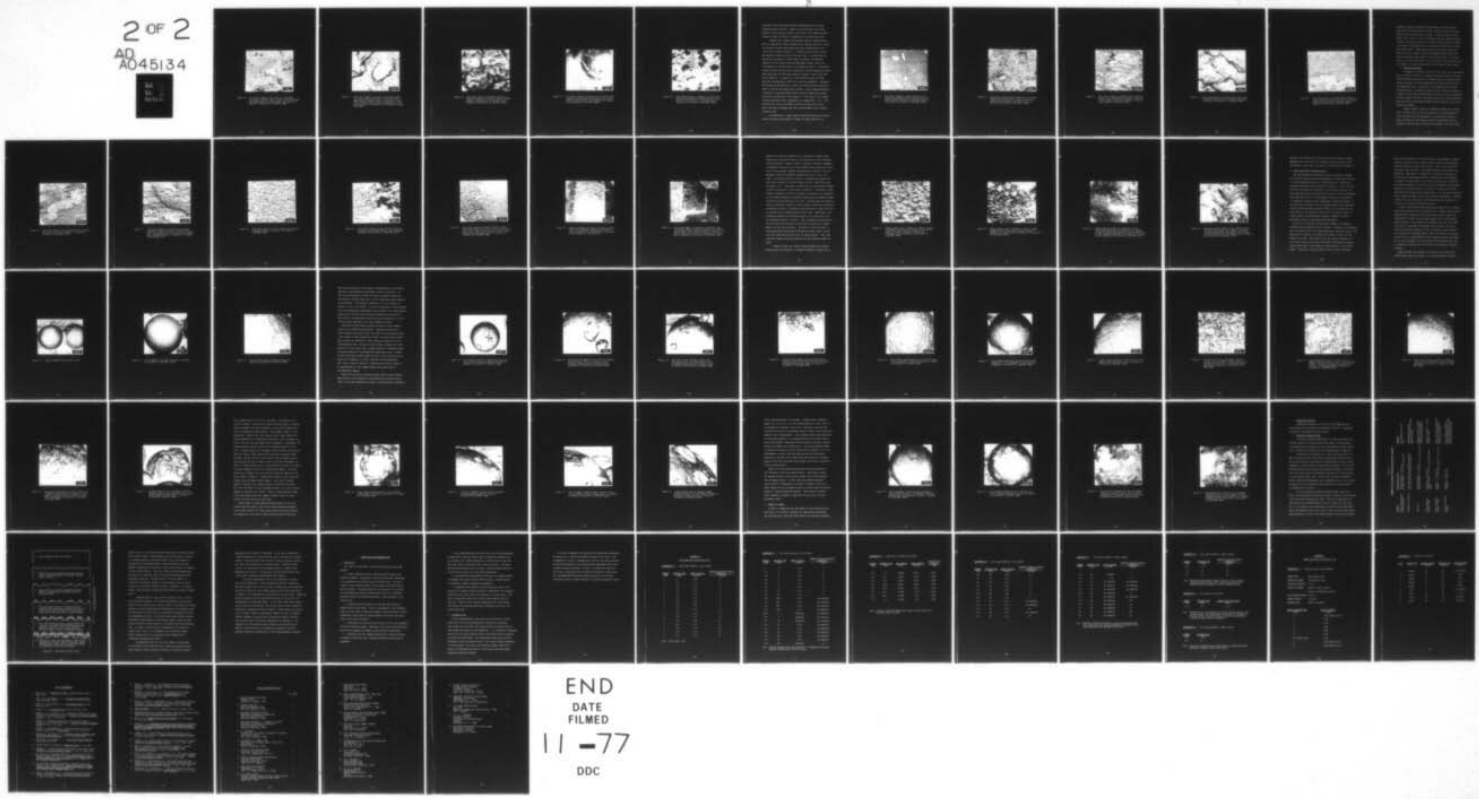

END
DATE
FILMED
11 -77
DDC

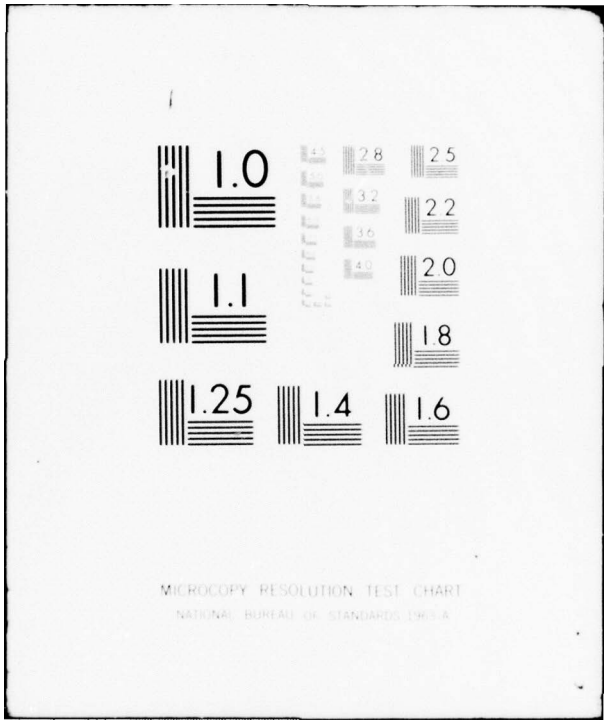
1.0
1.1
1.25
1.4
1.6
2.8
2.5
3.2
2.2
3.6
2.0
4.0
1.8
MICROCOPY RESOLUTION TEST CHART
NATIONAL BUREAU OF STANDARDS 1963-A

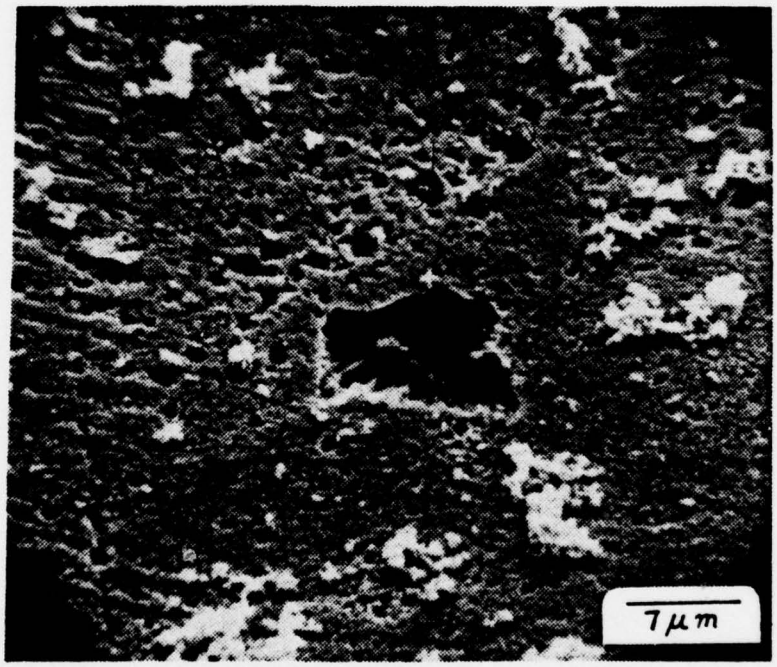

Figure 36. Zinc anode, region C; base metal pit surrounded by partially complete layer of gray oxidation product upon which deposit of white product has started; 15 minutes at 10 mA/cm^2 in 9.96N KOH, 2300X.

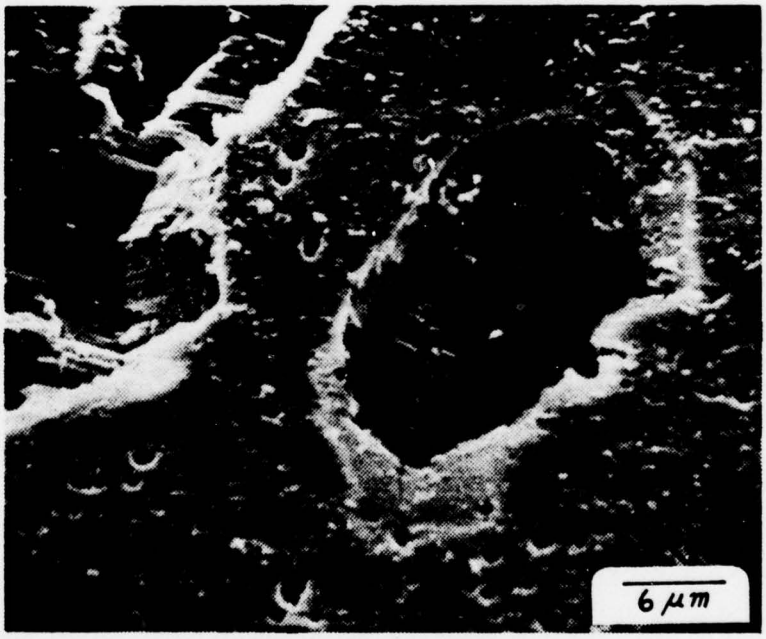

Figure 37. Zinc anode, region D, close to outer edge; pitted base metal structure partially covered by smooth, gray oxidation product layer; a sprinkling of small white oxidation product particles appears on top of the gray layer; 17.5 minutes at 6.67 mA/cm^2 in 9.96N KOH, 2400X.

Figure 38. Zinc anode, region B; cumulative buildup of oxidation products resulting in smooth, rounded surface; 21 minutes at 1.67 mA/cm^2 plus 12 minutes at 6.67 mA/cm^2 in 9.96N KOH, 2600X.

Figure 39. Zinc anode, region B; closeup view of smooth, thick oxidation layer showing surface cracks and "furry" texture; 21 minutes at 1.67 mA/cm^2 plus 12 minutes at 6.67 mA/cm^2 in 9.96N KOH, 13000X.

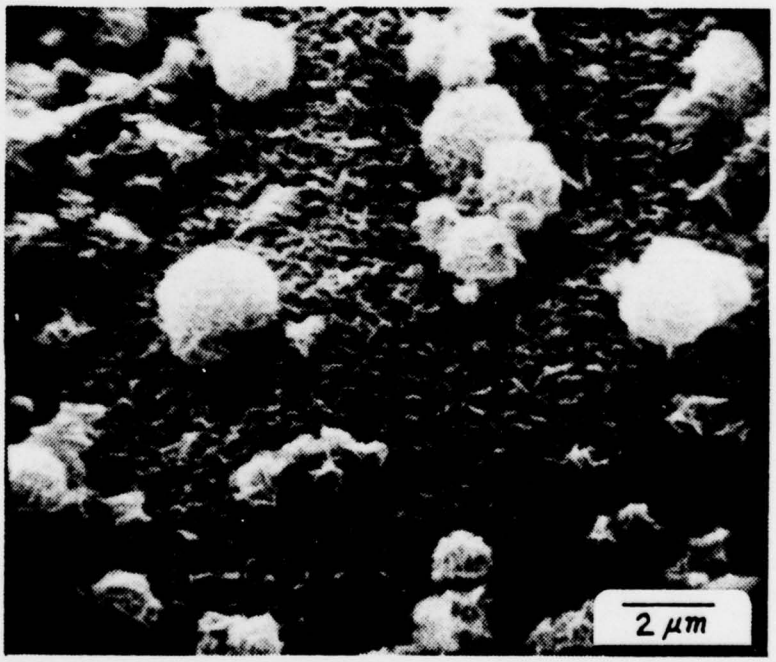

Figure 40. Zinc anode, region A; closeup view of gray and white oxidation products showing similar surface textures; 21 minutes at 1.67 mA/cm^2 plus 12 minutes at 6.67 mA/cm^2 in 9.96N KOH, 6600X.

and Bockris [24] have reported similar observations of zinc anode oxidation product textures. Figure 40 also shows that the surface texture of white and gray products are similar, even though the white product is loose and fluffy in comparison to the tight gray layer.

Samples run to passivation displayed specific characteristics. Prior to passivation a nearly complete gray layer was observed to cover the surface; the gray layer usually had some incompleteness at pit sites, such as shown in Figure 41. A light dusting of white product was generally observed on top of the gray layer. As passivation was approached, the amount of white product increased, and sometimes clusters of white product particles developed, usually close to pit site openings in the gray layer, as in Figures 42 and 43. Occasionally, oxidation product growth would be observed to outline large pitted areas where many small pits had grown together; Figures 43 and 44 show this type of behavior. In Figure 44 it also should be noted that white particles are beginning to build up in the pits themselves. Frequently the electrolyte was observed to cloud up and become milky colored just about at the same time passivation occurred. Several samples displayed a tendency for the gray product layer to develop random dark patches, just prior to passivation, as in Figure 45. This type of color change has been reported by other researchers; for example Hull, et al., [25] reported zinc oxide color changes in 5M KOH of light gray, silver, milky, and black, depending upon the operating region of the current-potential curve.

At passivation, a rapid, easily observed precipitation of white product occurred, which tended to blanket the anode surface in an

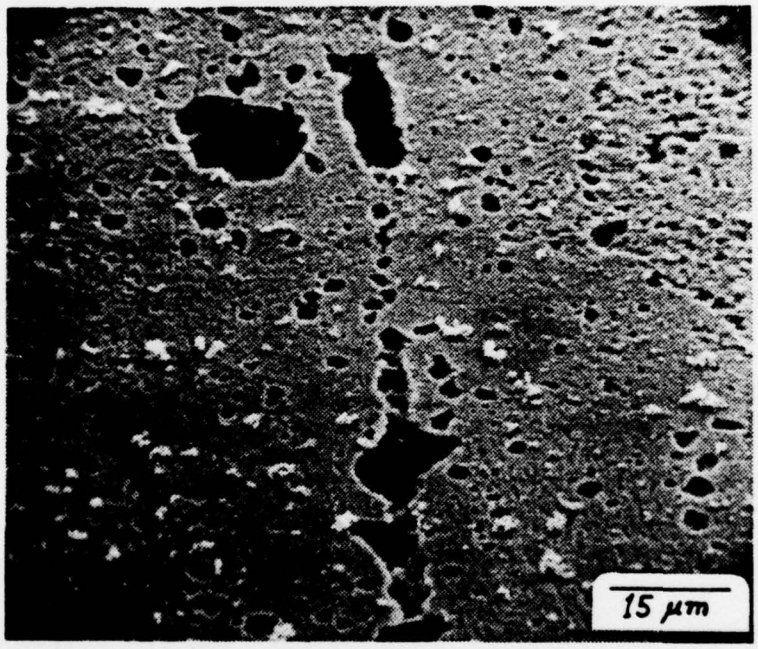

Figure 41. Zinc anode, region B; surface pits partially aligned along possible grain boundary; gray and white oxidation products are covering surface; 15 minutes at 10 mA/cm^2 in 9.96N KOH, 1120X.

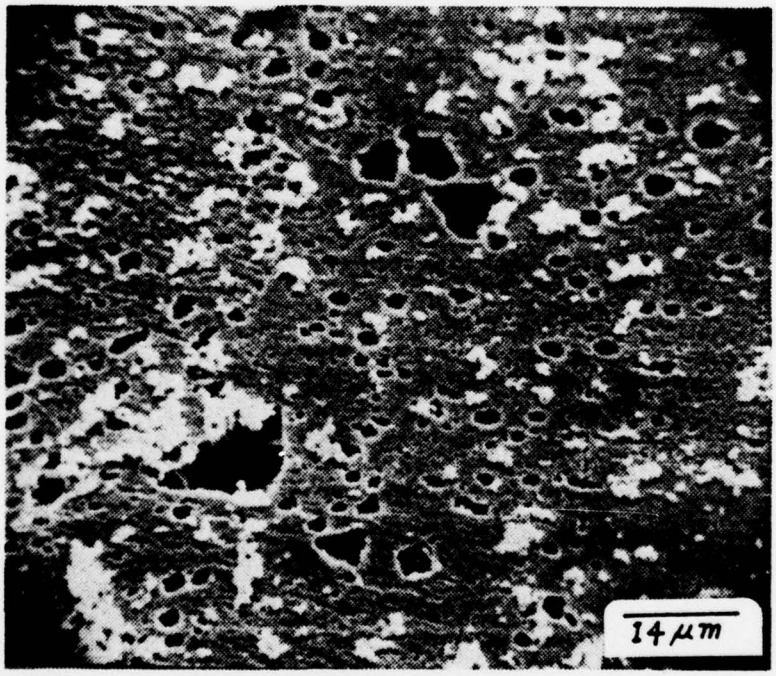

Figure 42. Zinc anode, region B; gray oxidation layer nearly complete over surface pits; nucleation sites of white oxidation products are also in view; 15 minutes at 10 mA/cm^2 in 9.96N KOH, 1150X.

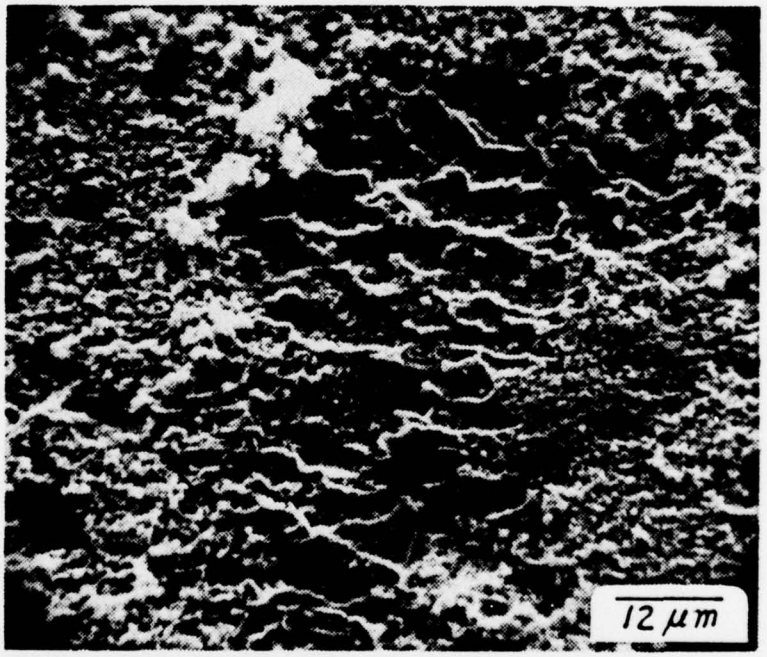

Figure 43. Zinc anode, region B; incomplete gray oxidation product layer surrounding etch pits; a thin top cover of white product also appears; 15 minutes at 10 mA/cm^2 in 9.96N KOH, 1250X.

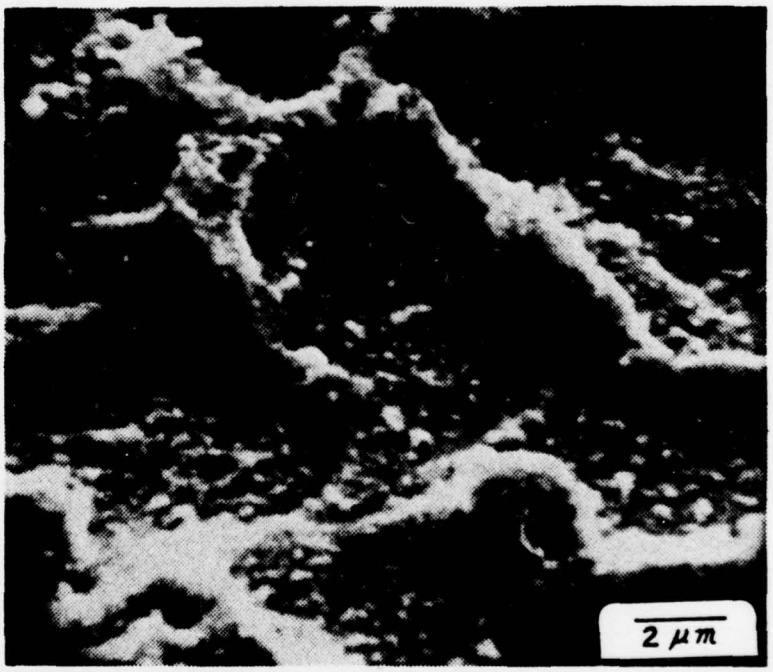

Figure 44. Zinc anode, region B; closeup view of pits with oxidation product growth outlining cavity edges; 15 minutes at 10 mA/cm^2 in 9.96N KOH, 6200X.

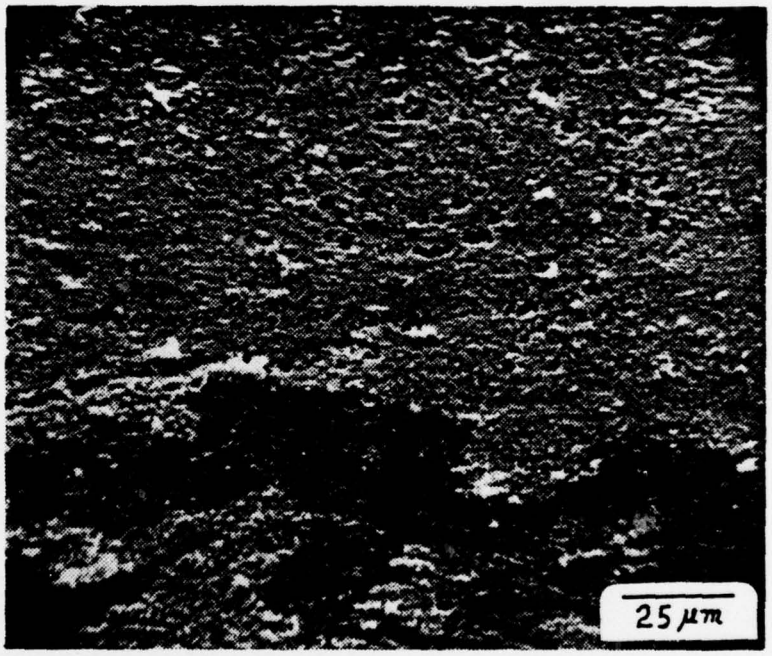

Figure 45. Zinc anode, region C; complete gray oxidation layer (darker in some areas) which is covered by a partial layer of white oxidation product; 15 minutes at 10 mA/cm^2 in 9.96N KOH, 620X.

incomplete fashion, leaving some areas densely covered with white product and others with sparse coverage. Figures 46 and 47 show this variable type of white product coverage. A typical densely covered anodic area is shown in detail by Figures 48 and 49; although densely covered, the flocculent nature of the white product particles produces a very porous looking layer that is distinctly different from a dense gray product layer. Dense white product layers such as these were about 5 μm thick. Figure 50 shows the boundary between dense white product and sparse white product; the flocculent nature of the white product is vividly illustrated. Also in evidence is white product that has started to fill pit sites which were not covered by gray product.

3. Dendrite Morphology

Although not a primary objective of this study, some observations of zinc plating, the result of cathodic reduction reactions, were made. These observations were made to investigate dendritic shorting between cathode and anode of the two-dimensional cell which occurred during a few experimental runs. The growth of zinc dendrites and resultant shorting has been a recognized problem with zinc battery electrodes for a number of years and has been studied in detail by several researchers. The most frequent solution to the problem has been to design impervious separators which prevent growth between battery plates but still allow electrolyte passage.

Figure 51 shows a typical zinc dendrite growing from cathode (left) to anode (right) across the separator in the two-dimensional cell; the branch and leaf appearance is a characteristic feature. Figure 52 shows the end of several dendrite leaves where they have completed a path for short circuiting by attaching to the zinc anode.

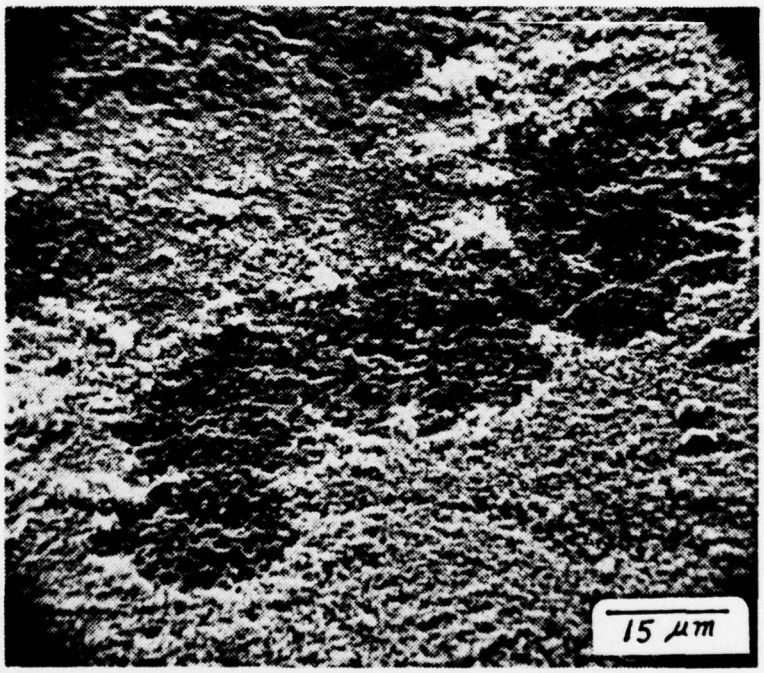

Figure 46. Zinc anode, region C; gray and white dual oxidation products, white layer incomplete, 15 minutes at 10 mA/cm^2 in 9.96N KOH, 1120X.

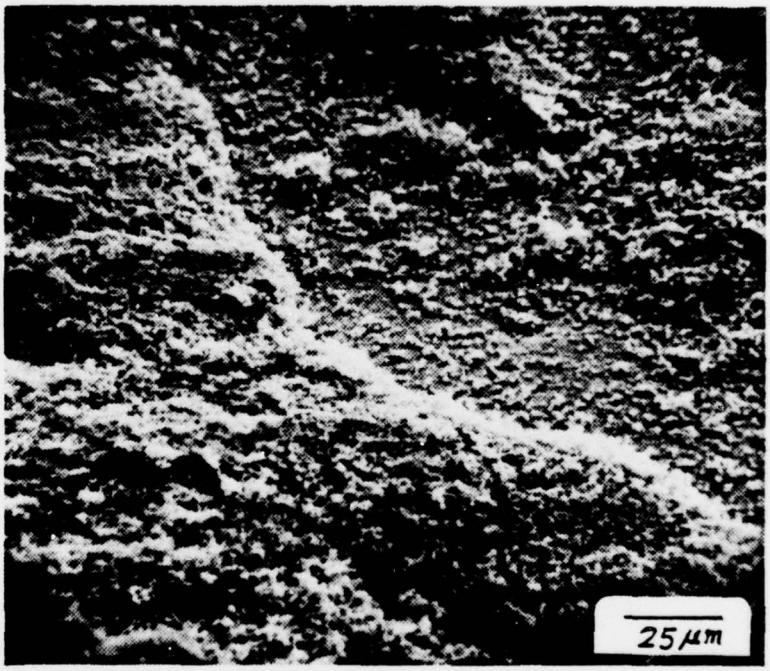

Figure 47. Zinc anode, region C; transition zone between complete two-layer oxidation products (gray and white) and incomplete two-layer products (complete gray, incomplete white); 15 minutes at 10 mA/cm^2 in 9.96N KOH, 570X.

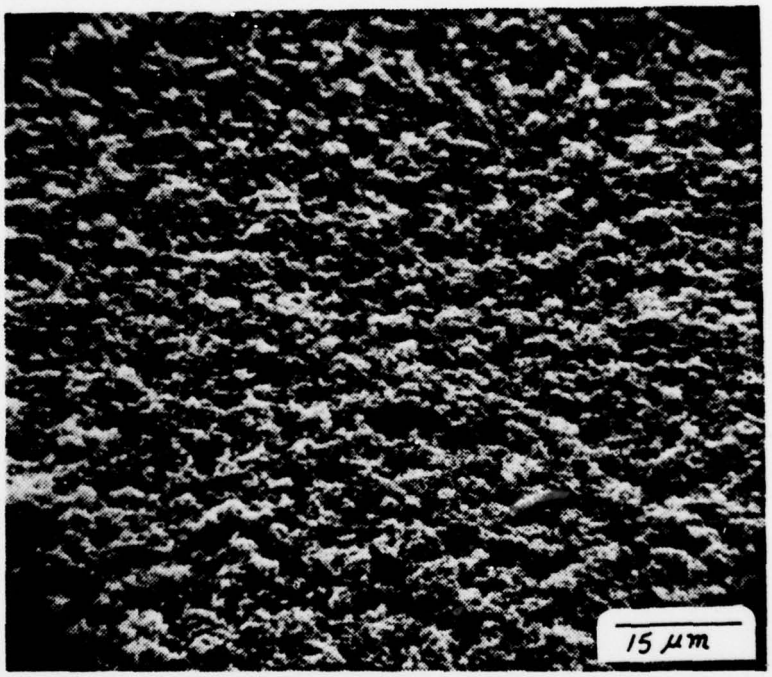

Figure 48. Zinc anode, region B; view of dense layer of white oxidation product; 15 minutes at 10 mA/cm^2 in 9.96N KOH, 1200X.

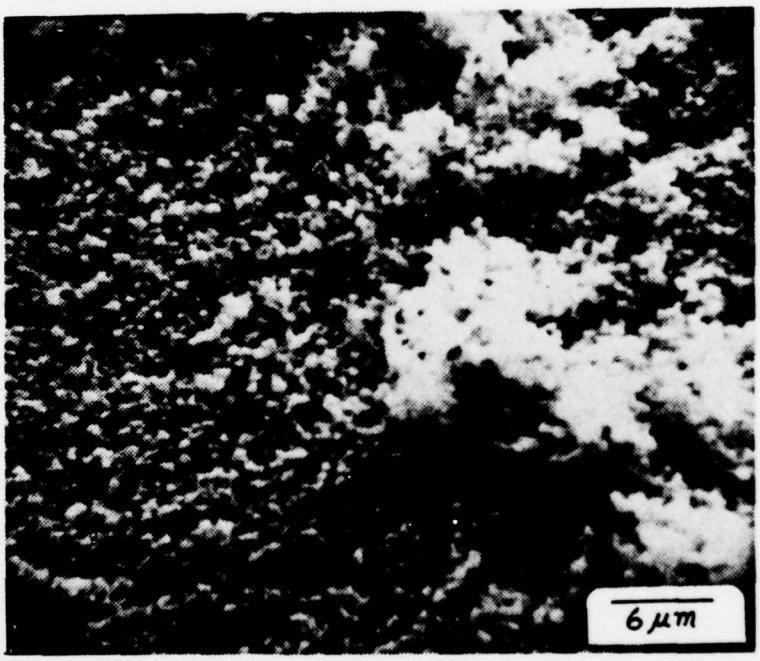

Figure 49. Zinc anode, region B; gray and white oxidation products, white product showing vertical growth; 15 minutes at 10 mA/cm^2 in 9.96N KOH, 2400X.

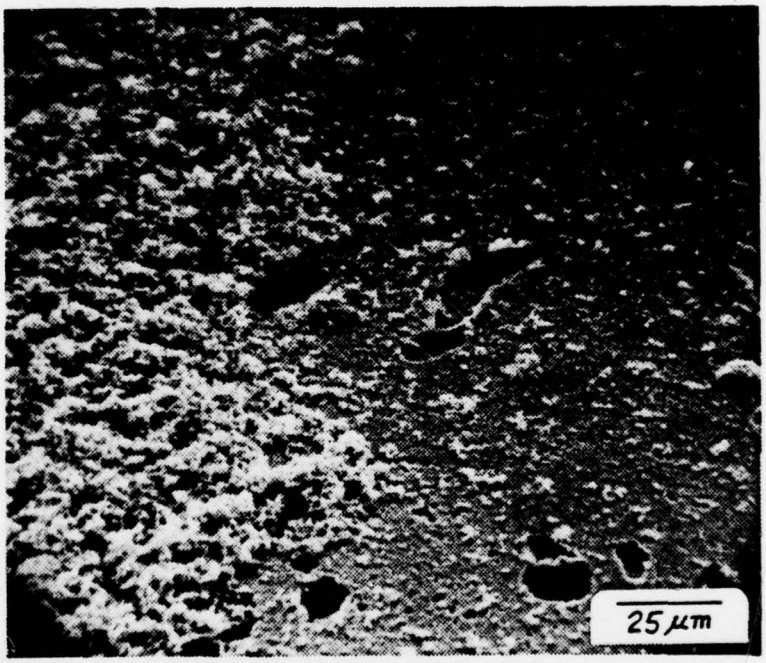

Figure 50. Zinc anode, region B; boundary between complete white oxidation product layer (left) and incomplete white layer (right); gray oxidation product layer appears below the white product; 15 minutes at 10 mA/cm^2 in 9.96N KOH, 600X.

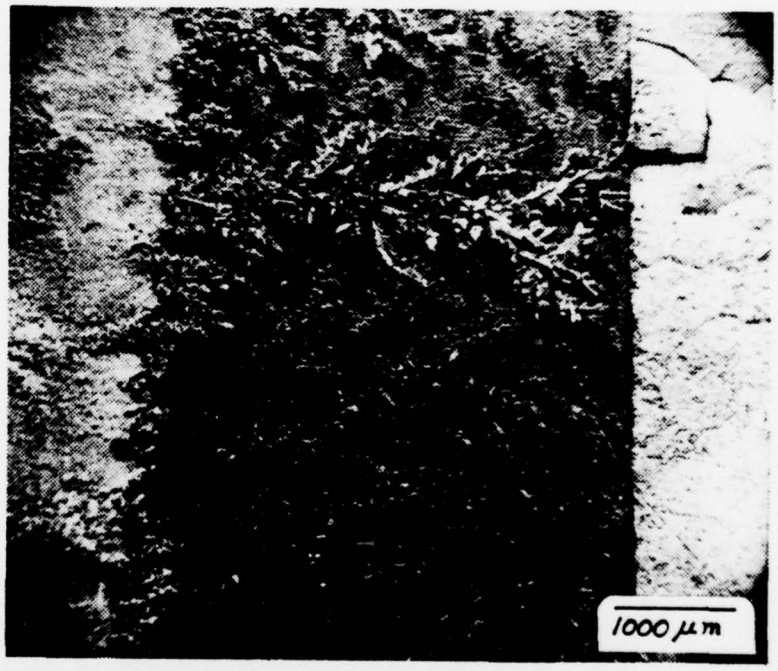

Figure 51. Separator between zinc anode and copper cathode; view of zinc dendrites growing from cathode to anode; 21 minutes at 1.67 mA/cm^2 plus 12 minutes at 6.67 mA/cm^2 in 9.96N KOH, 17X.

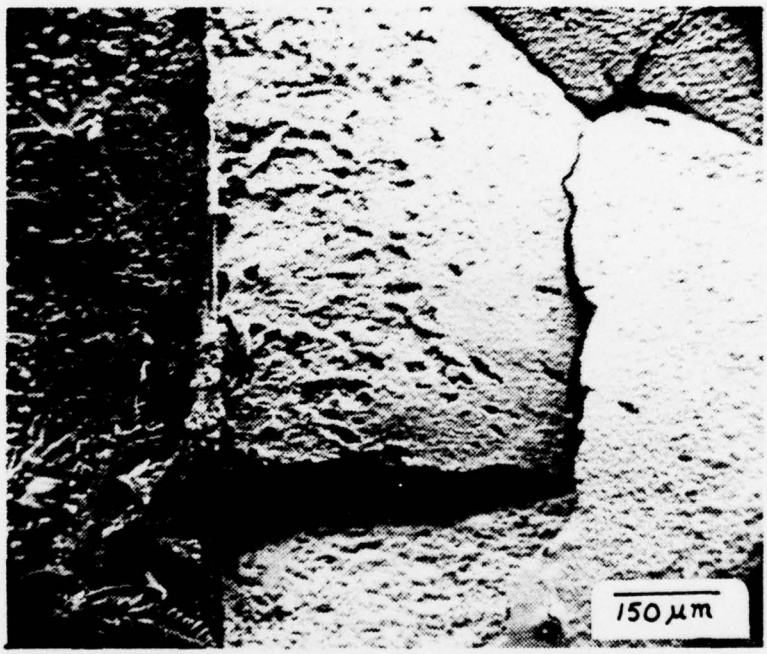

Figure 52. Zinc anode, region A, adjacent to separator; view of shorting dendrite which has grown across separator from cathode; thick, cracked surface of oxidation product layer also visible; 21 minutes at 1.67 mA/cm^2 plus 12 minutes at 6.67 mA/cm^2 in 9.96N KOH, 100X.

Figures 53-55 show the cathodic end of the dendritic growth; these figures show the growth process at zinc plating sites that eventually produces dendrites. Figure 53 shows a frequently observed arrangement of hexagonal zinc plates that occurs during initial plating; the plates tend to stack together randomly, producing small islands or clusters. Hexagonal plates have diameters ranging from 2 μm to 5 μm at this stage. As plating reactions continue, the islands grow together and plate sizes increase, as shown in Figure 54; here, plates have grown as large as 9 μm. Continuation of growth next to the separator produces vertical columns such as those shown in Figure 55. The growth of these columns, estimated to be about 15 μm high, is believed to be influenced by surrounding hydrogen gas generation resulting from competing cathodic reactions involving reduction of H^+ ions. The observable gas production tends to concentrate current at certain cathodic sites by gas blanketing surrounding locations; the higher current densities at these sites tend to increase the zinc plating reaction rates there. Additionally, gas blanketing prevents any horizontal growth of zinc plating such that the predominant growth is vertical. Thus, concentrated plating action which can only grow vertically is the result, forcing zinc columnar growth out into the electrolyte. The limits of vertical growth in these experiments were defined by the spacing between cathode surface and cover slide which was set by the 15 μm mylar spacer. After that limit was reached, the growth pushed across the separator toward the anode.

Figure 56 shows the columnar stacked hexagonal zinc plates growing across the separator; the general direction of growth may be

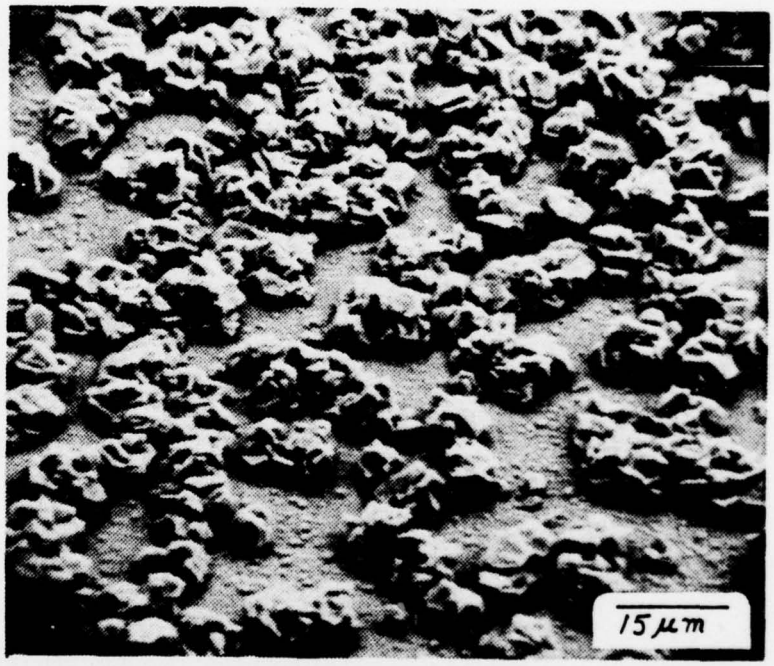

Figure 53. Copper cathode, next to separator; typical clusters of hexagonal zinc plates which grow during initial stages of cathodic plating; 21 minutes at 1.67 mA/cm^2 plus 12 minutes at 6.67 mA/cm^2 in 9.96N KOH, 1100X.

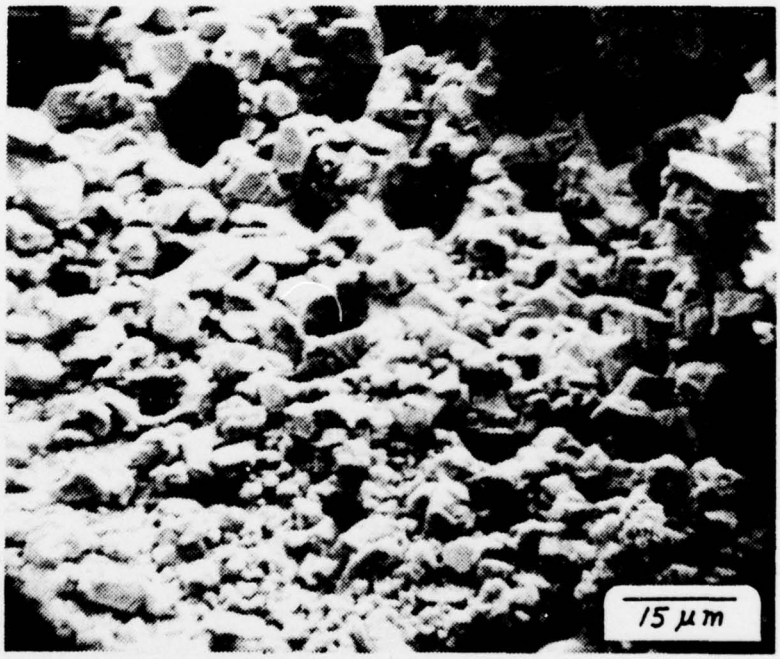

Figure 54. Copper cathode, next to separator; typical stacked hexagonal plates resulting from zinc plating; 21 minutes at 1.67 mA/cm^2 plus 12 minutes at 6.67 mA/cm^2 in 9.96N KOH, 1080X.

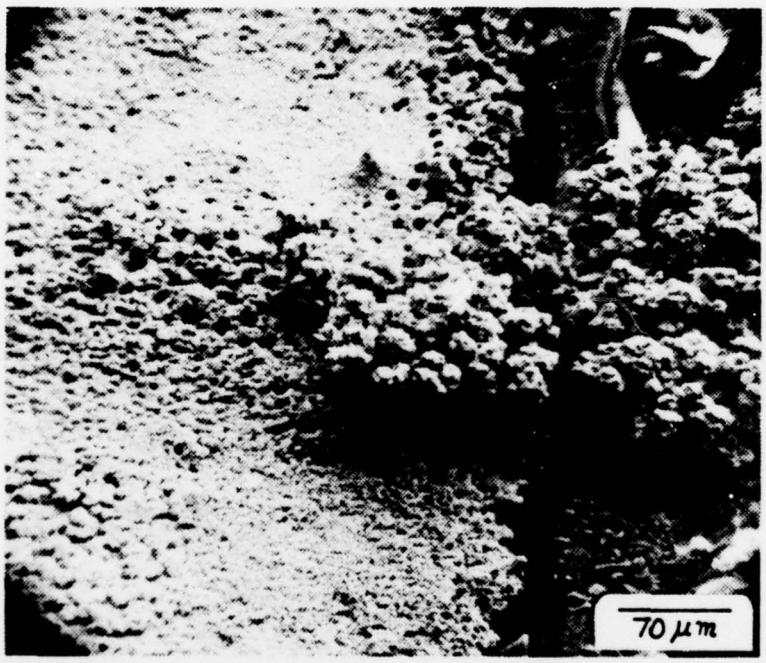

Figure 55. Copper cathode, adjacent to separator; view of zinc plating which has initially grown in vertical columns and then moved horizontally across separator to form a shorting dendrite; 21 minutes at 1.67 mA/cm^2 plus 12 minutes at 6.67 mA/cm^2 in 9.96N KOH, 220X.

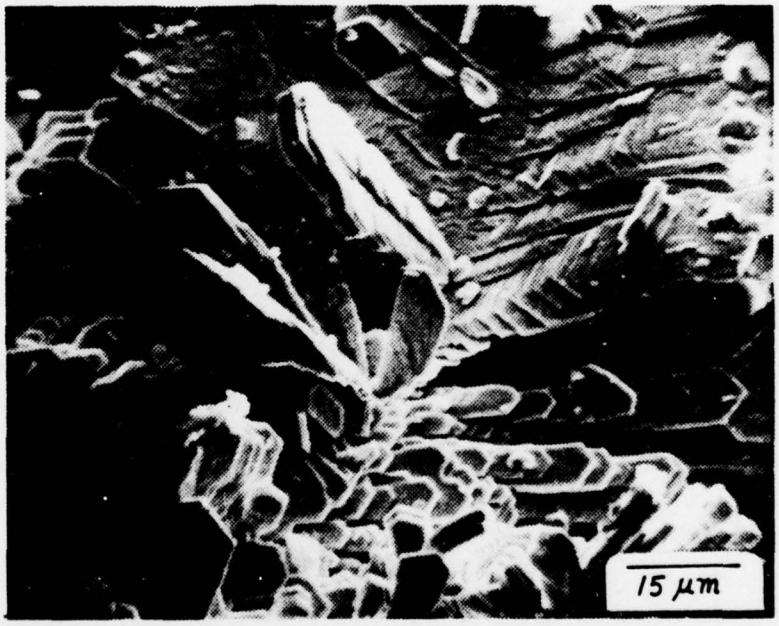

Figure 56. Separator between cathode and zinc anode; closeup of ordered zinc plates that comprise a dendrite which has grown across the separator from cathode to anode; 21 minutes at 1.67 mA/cm^2 plus 12 minutes at 6.67 mA/cm^2 in 9.96N KOH, 1080X.

observed to be vertical and to the right where the anode is located. Hexagonal zinc plate sizes have increased as they have grown across the separator; plate sizes as large as 14 μm are visible in Figure 56.

B. THREE-DIMENSIONAL EXPERIMENT RESULTS

The three-dimensional experimental work was originally intended as a method to obtain quantitative measurement of penetration distance in a three-dimensional porous zinc electrode matrix, in addition to obtaining morphology data associated with oxidation. Due to failures resulting from sphere bed conductivity, as previously reported, the three-dimensional work was limited to the use of a very thin "monolayer" anode comprised of zinc or plated spheres with which it was desired to investigate oxidation product morphology on individual spheres. It was hoped that correlation could be obtained between three-dimensional oxidation product growth and growth observed in two-dimensional work. Additionally, it was desired to obtain data to correlate changes in current density with morphological changes. Appendix B contains experimental data for three-dimensional experiments.

The goal of correlating current density changes with changes in oxidation product morphology was not realized. Although nine experimental runs utilizing both zinc and plated spheres were conducted, using current densities from 1 mA/cm^2 to 50 mA/cm^2, the results for each run were basically the same. Those results were that, without exception, for each current density value used, some spheres had extensive oxidation product growth while others showed no visible growth or only partial growth. Thus heavily oxidized spheres could be found in the anode

which had been exposed at low current density, and conversely, spheres showing no visible reaction products could be found in the anode which had been exposed at a high current density. These results precluded obtaining a cause and effect relationship between current density and morphology. Apparently the problem with conductivity experienced in the sectioned bed experiment was also a problem with this experiment. It appears that some spheres in the anodic bed had poorer conductivity than others, possibly as the result of initial oxidation product growth, leading to the ultimate result of little or no current flow through some spheres and large amounts through others. The non-uniform oxidation product growth throughout the bed was the obvious consequence. Evidently a porous electrode constructed from lossely packed zinc spheres is not suitable for achieving the desired objective.

In spite of the failures mentioned, morphological study of oxidized spheres was possible and did yield useful data. Figure 57 shows typical unexposed plated spheres; the relatively smooth surface texture was characteristic of most zinc and plated spheres prior to KOH exposure. Figure 58 shows a silver sphere after exposure; etch pits are visible, and there are a few small dark patches on the surface. The silver sphere was anodically exposed in order to provide a visual reference for the results of oxidizing silver in KOH. The intent was to produce an aid for use in identifying any silver oxidation products that might appear on plated spheres in the event that zinc plating was very thin or incomplete, allowing silver base metal to participate in oxidation reactions.

Figure 59 shows clear evidence of pitting on the surface of an exposed plated sphere with little or no oxidation products visible.

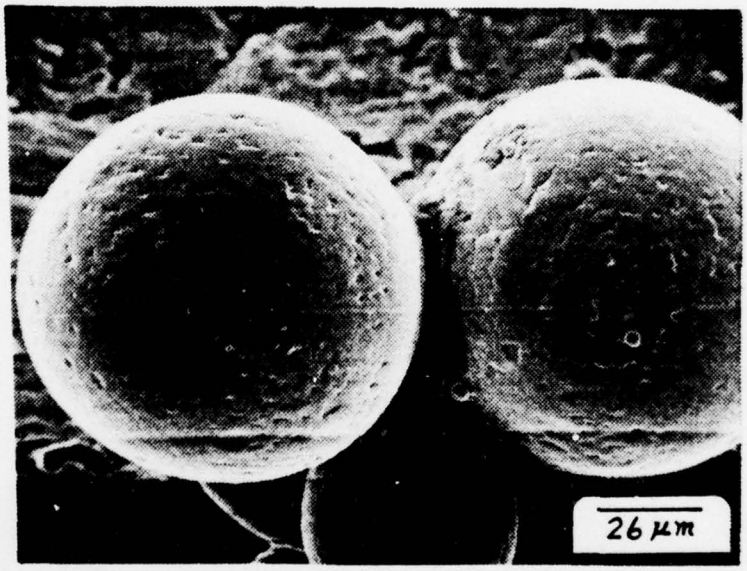

Figure 57. Typical unexposed plated sphere, 580X.

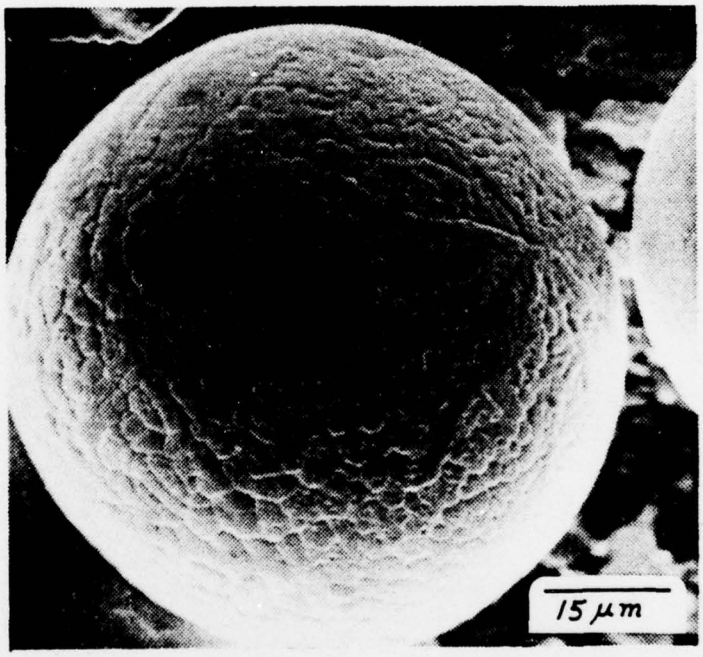

Figure 58. Silver sphere with visible etch pits; 30 seconds at 50 mA/cm^2 in 9.96N KOH, 1200X.

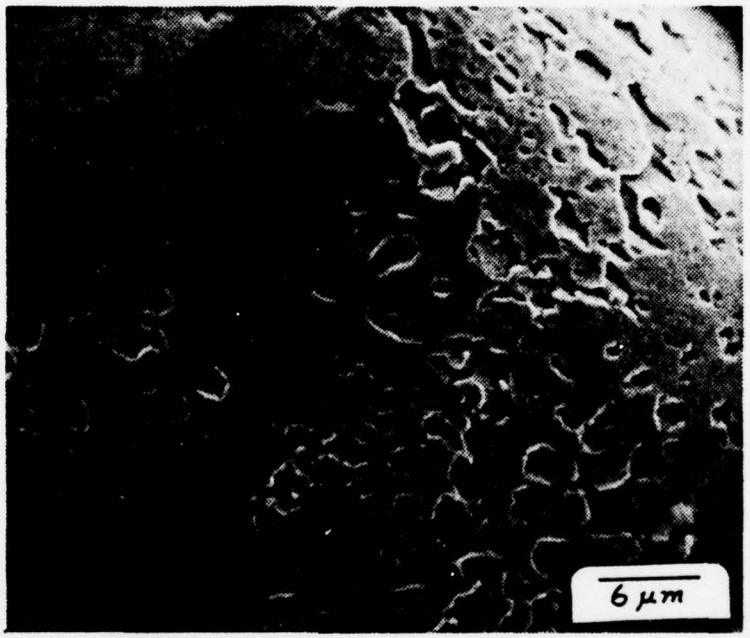

Figure 59. Plated sphere showing extensive pitting; 30 seconds at 50 mA/cm^2 in 9.96N KOH, 2400X.

This pitting displays the same general characteristics as the pitting observed in two-dimensional experiments, such as in Figure 19. As with the two-dimensional pitting, the lack of oxidation products on the surface is probably indicative of low current-time product exposure for this sphere. The average pit diameter is 2.1 μm, and the pit density if 1.25×10^7 pits/cm^2. Pit size is about half of that observed for the two-dimensional experiments, and pit density is 14 times greater. These results indicate that the sphere had smaller pits and more of them than the two-dimensional anode, which may be indicative of a more uniform current distribution on a given spherical surface.

Figures 60-63 show similar oxidation products as those observed during the two-dimensional experiments. Figures 60 and 61 show a nearly complete gray product layer with some pit site openings visible; a small amount of white product may be seen on the gray layer surface. These results are comparable to those observed in Figure 41 for the two-dimensional work. The layer of gray product in Figure 61 is estimated to be 0.8 μm thick, which compares favorably to thickness values previously reported for two-dimensional sample gray layers. Figures 62 and 63 show white product growth on top of a gray layer which also bears close resemblance to results observed from two-dimensional work, such as shown in Figure 42. White particle sizes in Figure 63 are approximately 0.5 μm, somewhat smaller than sizes found on two-dimensional samples.

Figures 64-71 show the oxidation products found on plated spheres. These products can be grouped into individual gray and white product types, as with past observations; however, the gray product consistently

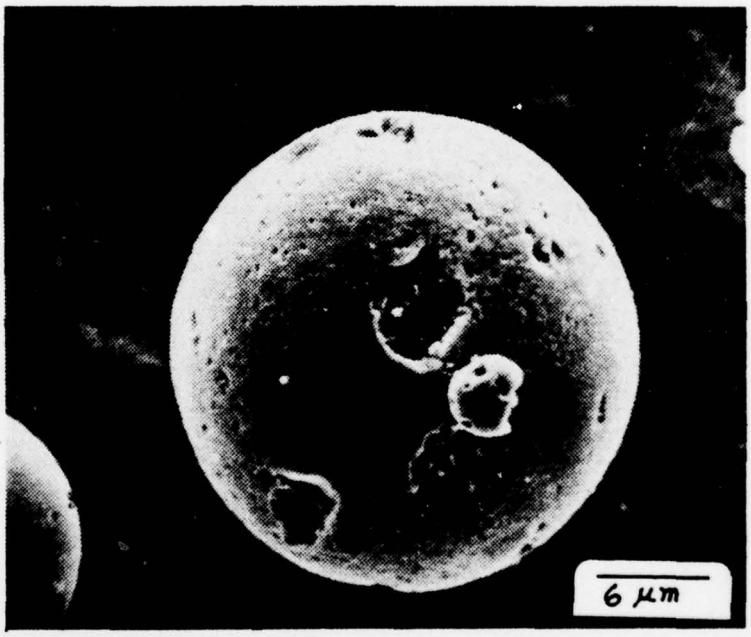

Figure 60. Zinc sphere with nearly complete gray oxidation layer; several large pits remain uncovered; 30 seconds at 50 mA/cm^2 in 9.96N KOH, 2600X.

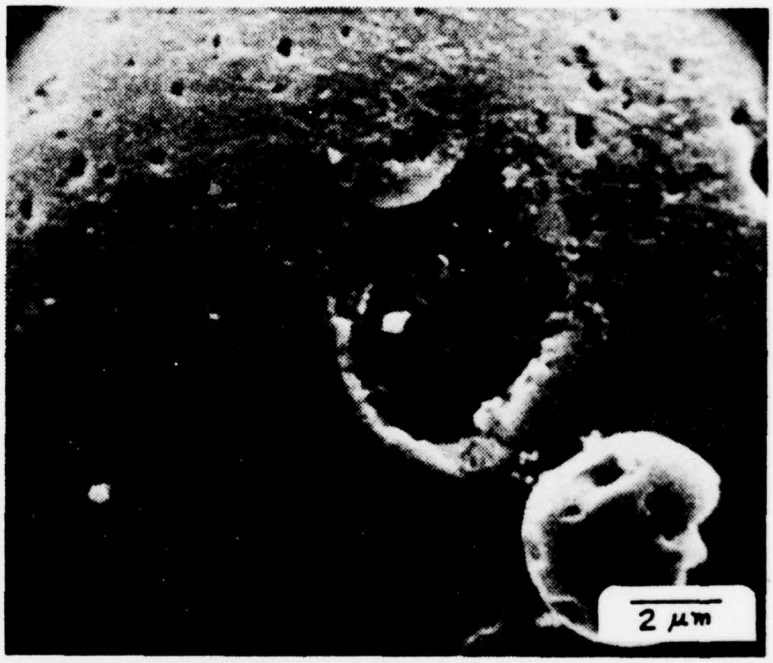

Figure 61. Closeup of zinc sphere pit site with surrounding gray oxidation layer and observable initial oxidation product nucleation within the pit; 30 seconds at 50 mA/cm^2 in 9.96N KOH, 6400X.

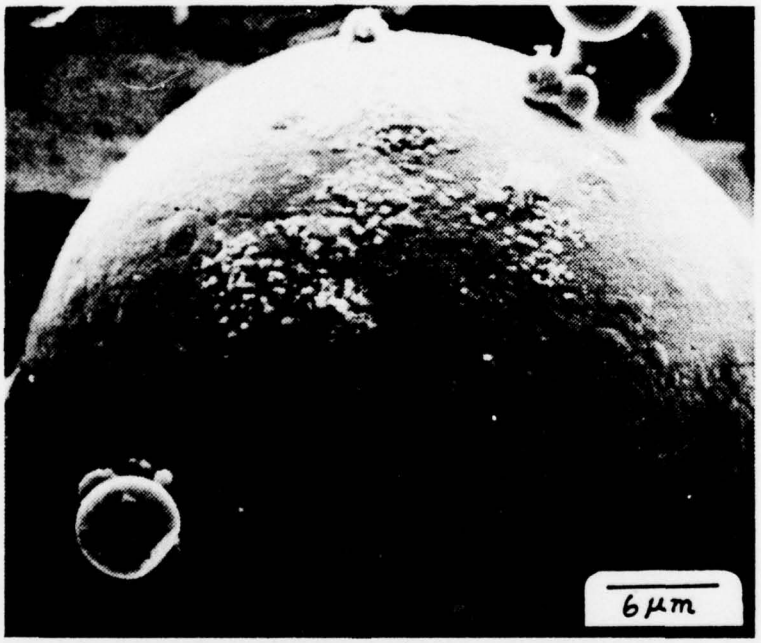

Figure 62. Zinc sphere surface showing complete gray oxidation product layer and nucleation sites of incomplete white oxidation product layer; 30 seconds at 50 mA/cm^2 in 9.96N KOH, 2700X.

Figure 63. Closeup of zinc sphere surface on which white oxidation product nucleation sites have developed over gray oxide surface layer; 30 seconds at 50 mA/cm^2 in 9.96N KOH, 6700X.

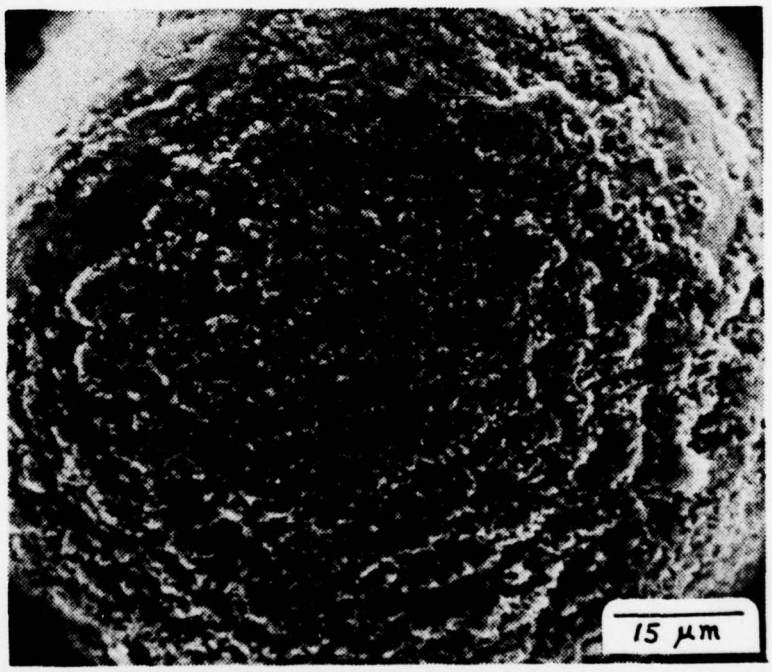

Figure 64. Plated sphere displaying growth of dark and light ("salt and pepper") oxidation products; 30 seconds at 50 mA/cm^2 in 9.96N KOH, 1200X.

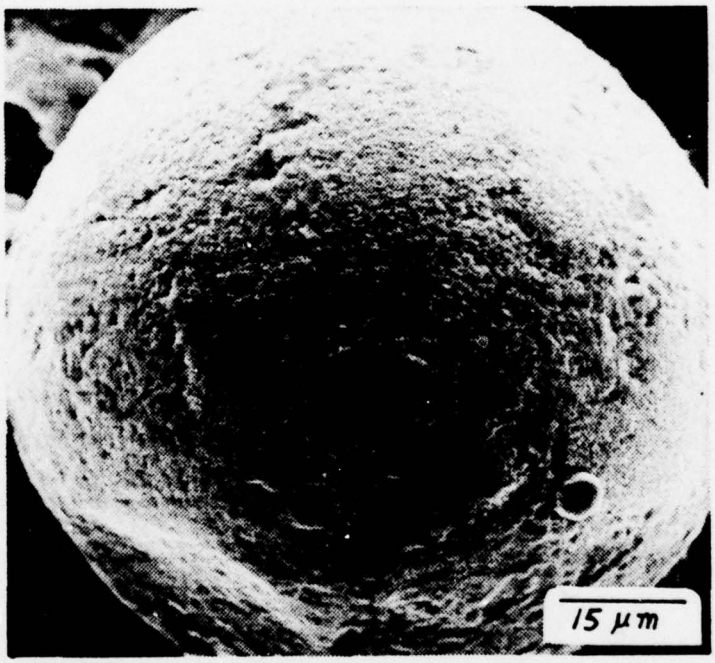

Figure 65. Plated sphere displaying complete surface cover composed of "salt and pepper" oxidation product; 30 seconds at 25 mA/cm^2 in 9.96N KOH, 1250X.

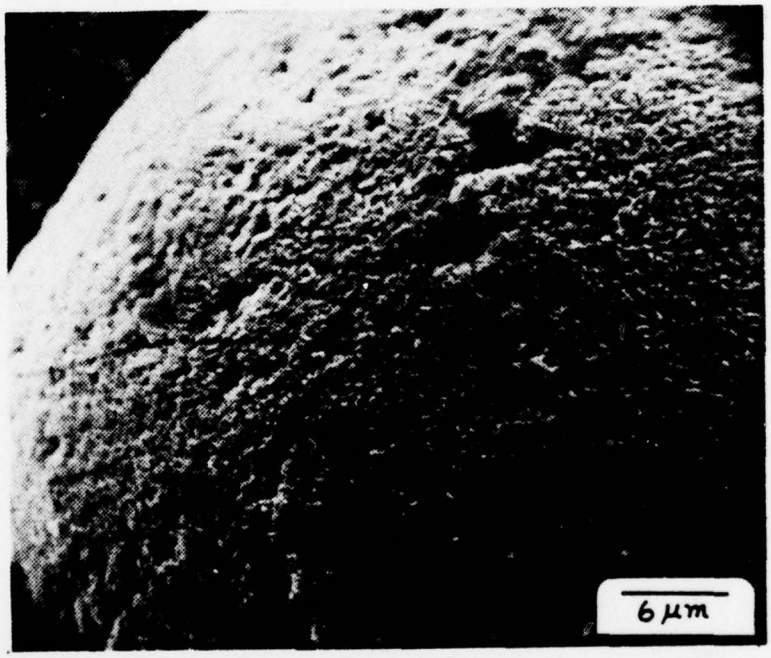

Figure 66. Plated sphere completely covered with "salt and pepper" oxidation product layer; 30 seconds at 25 mA/cm^2 in 9.96N KOH, 2500X.

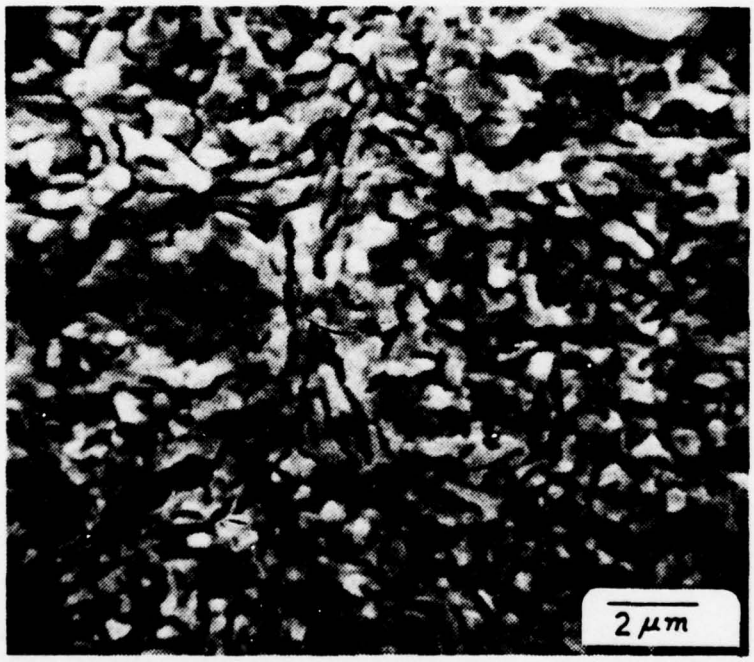

Figure 67. Closeup view of "salt and pepper" oxidation product on plated sphere; product appears as a cracked gray layer with a scattering of white particles; 30 seconds at 5 mA/cm^2 in 9.96N KOH, 6700X.

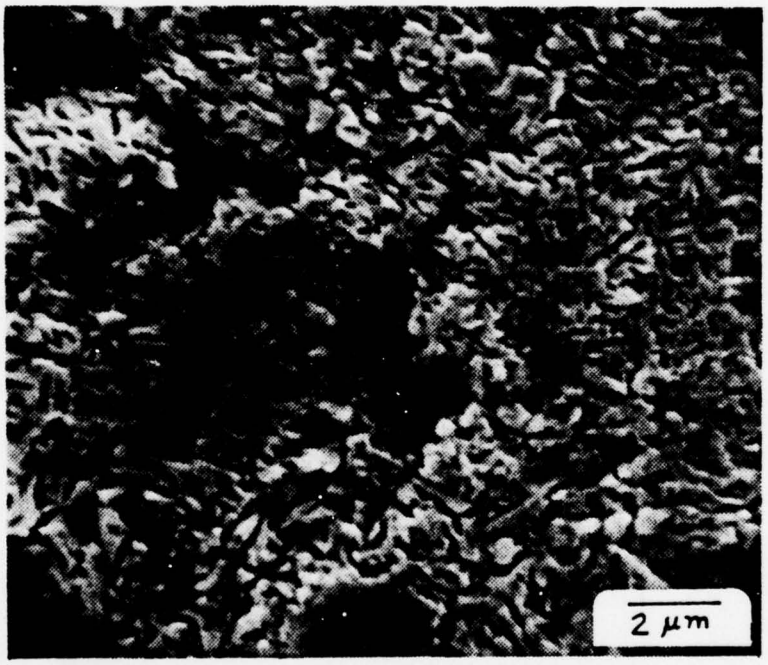

Figure 68. High magnification view of a dense "salt and pepper" oxidation product layer on a plated sphere surface; individual constituent white and gray products are distinguishable; 30 seconds at 25 mA/cm^2 in 9.96N KOH, 6300X.

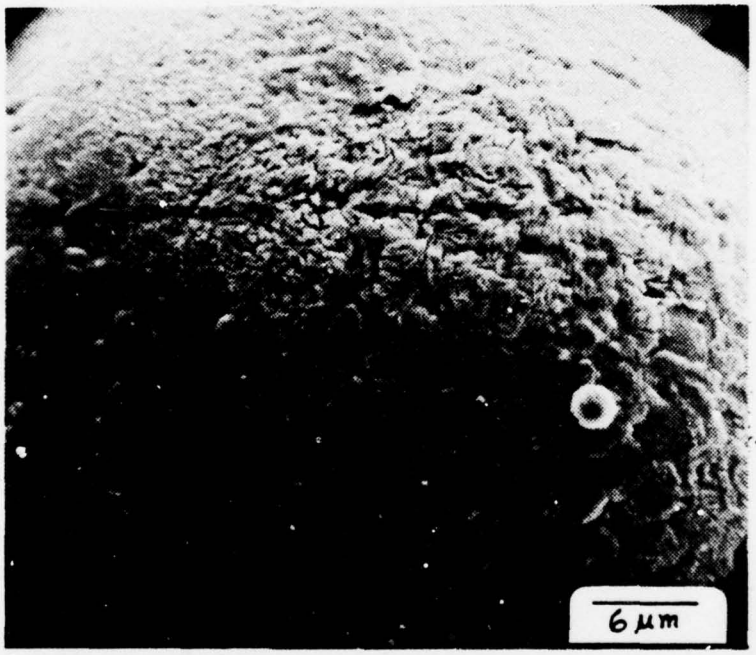

Figure 69. Plated shere surface on which an incomplete layer of "salt and pepper" oxidation product has grown; 30 seconds at 25 mA/cm^2 in 9.96N KOH, 2500X.

Figure 70. Closeup of plated sphere surface on which "salt and pepper" oxidation product appears; initial stages of product growth are visible in lower half of photograph; 30 seconds at 25 mA/cm^2 in 9.96N KOH, 6200X

Figure 71. Advanced stage of "salt and pepper" oxidation product growth on plated sphere surface; thick, crusty product has developed; 30 seconds at 10 mA/cm^2 in 9.96N KOH, 1250X.

had a random pattern of 0.5 μm to 3 μm cracks. The reason for the cracks is unknown. They were only found on plated spheres, so perhaps their development had some relationship to the cyanide plating bath used in preparing the plated spheres. This thought, however, is only speculation. Whatever the cause, the gray layer cracks altered the overall appearance of a combined gray and white product coverage such that it took on a salt and pepper type of appearance. Accordingly, the combined product has been called "salt and pepper product" in this study. Figure 64 shows salt and pepper product partially covering the spherical surface, while Figures 65-66 show nearly complete surface coverage. Figures 67-68 are close views of salt and pepper product; these figures show that the white product in the salt and pepper composite is loosely deposited upon a more adherent gray layer in a manner previously observed to occur on two-dimensional samples. The white product has a diameter of 0.5 μm, which is almost the same as for the white product of Figure 63. Figures 69-70 provide a look at the early stages of salt and pepper product growth. Gray layer "cracking" appears to develop as an inherent feature of nucleation and growth and is not the result of later thickness buildup, i.e. is not actually mechanical cracking of the product. Figure 71 shows advanced stages of salt and pepper growth; the rugged, "cracked" texture is still visible, even with this very thick layer.

A small number of plated spheres displayed growth of very dark colored oxidation products which had not been encountered elsewhere in this study; Figures 72-75 show plated spheres with these products. In recognition of the shape of these mysterious products they were

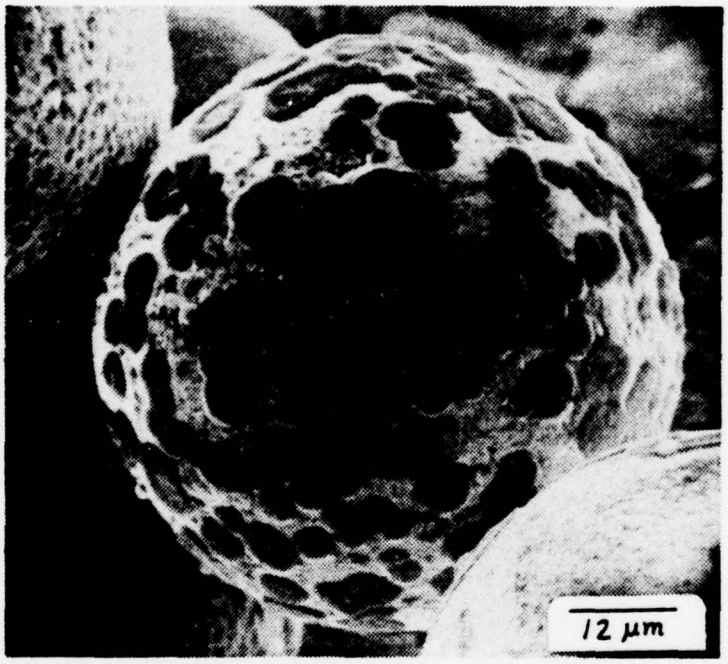

Figure 72. Plated sphere showing growth of dark "pancake" shaped oxidation products; 30 seconds at 50 mA/cm^2 in 9.96N KOH, 1300X.

Figure 73. Profile of "pancake" shaped oxidation products on plated sphere surface; 30 seconds at 50 mA/cm^2 in 9.96N KOH, 2500X.

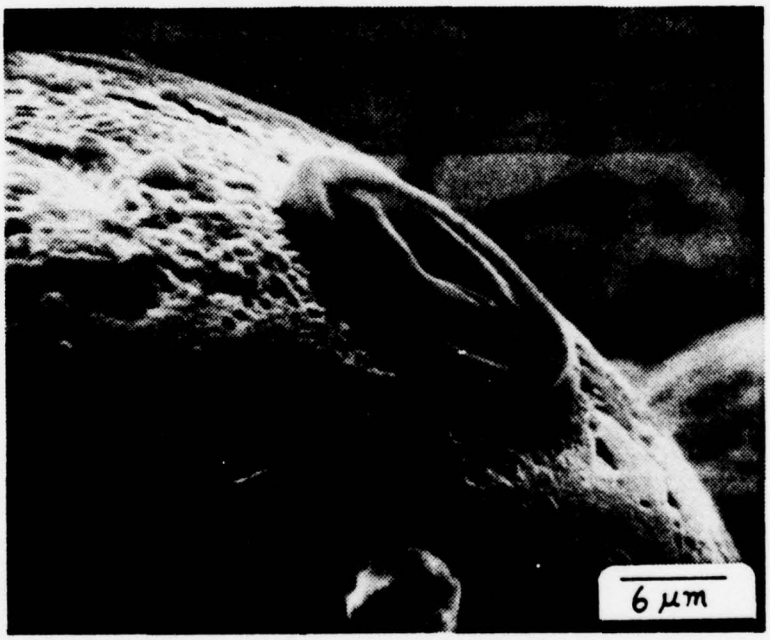

Figure 74. View of single "pancake" shaped oxidation product on plated sphere surface; dimpled center is visible; 30 seconds at 50 mA/cm^2 in 9.96N KOH, 2500X.

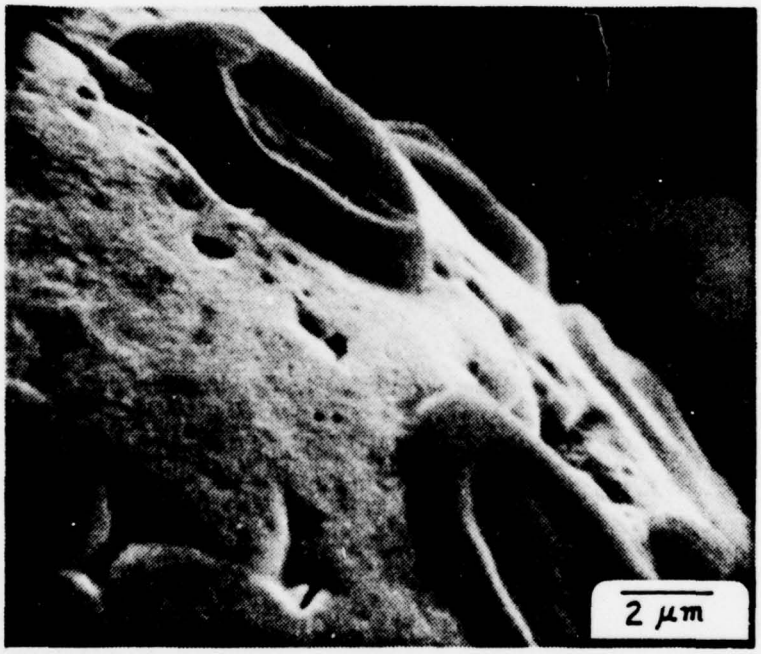

Figure 75. Closeup profile view of "pancake" shaped oxidation products on plated sphere; height of products is clearly visible; 30 seconds at 50 mA/cm^2 in 9.96N KOH, 6300X.

called "pancake product" for reference. Pancake product diameters ranged from 3.8 μm to 8.7 μm, and average height was 1.0 μm. Most of the pancakes were dimpled in the center, indicating a reaction site from which the product was spreading; Figure 74 shows a very distinctive example of this characteristic. Since pancake products were found only on a few plated spheres, it is postulated that they are some type of silver oxide product, resulting from the oxidation reaction of spheres having an incomplete zinc plating layer. Since plated spheres showed a relatively thin layer of zinc in cross-section (Figure 9), it is not unreasonable to suspect that some areas may have not been plated. Additionally, the bare silver sphere which was exposed for reference (Figure 58) did show some small dark patches, which may be indicative of early pancake growth.

Figures 76-79 show plated spheres which had combined growth of salt and pepper as well as pancake products. Where this occurred, the pancakes spread out and over the tighter, more surface adherent salt and pepper product. In some cases the pancakes displayed a certain amount of transparency, as evident in Figures 78 and 79; in these figures the salt and pepper product is visible under the pancake product by looking through the pancakes. Early growth of pancake product appears to resemble a light haze over the top of the salt and pepper product.

C. SUMMARY OF RESULTS

In order to encapsulate the large amount of data obtained during this study, it is useful to tabulate the quantitative measurements and also postulate a model that helps explain the observed morphology.

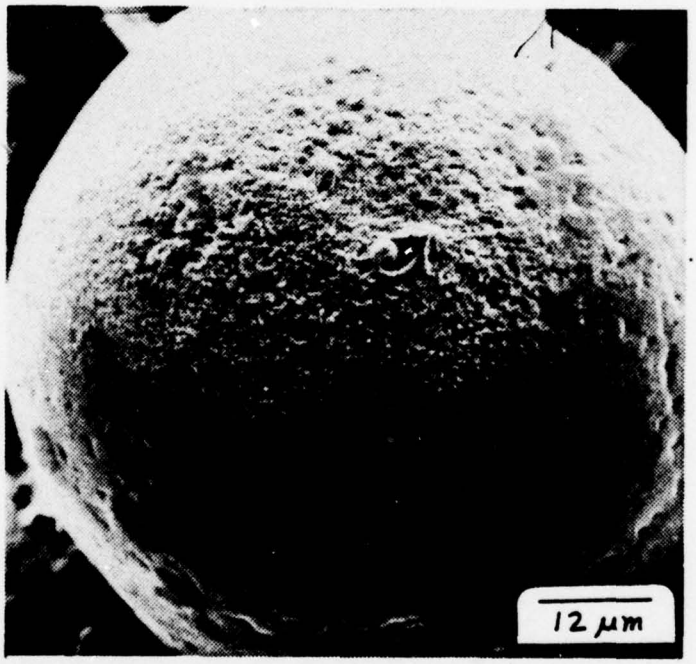

Figure 76. "Salt and pepper" oxidation product growing on plated sphere surface; a few "pancake" oxidation products are also present; 30 seconds at 5 mA/cm^2 in 9.96N KOH, 1320X.

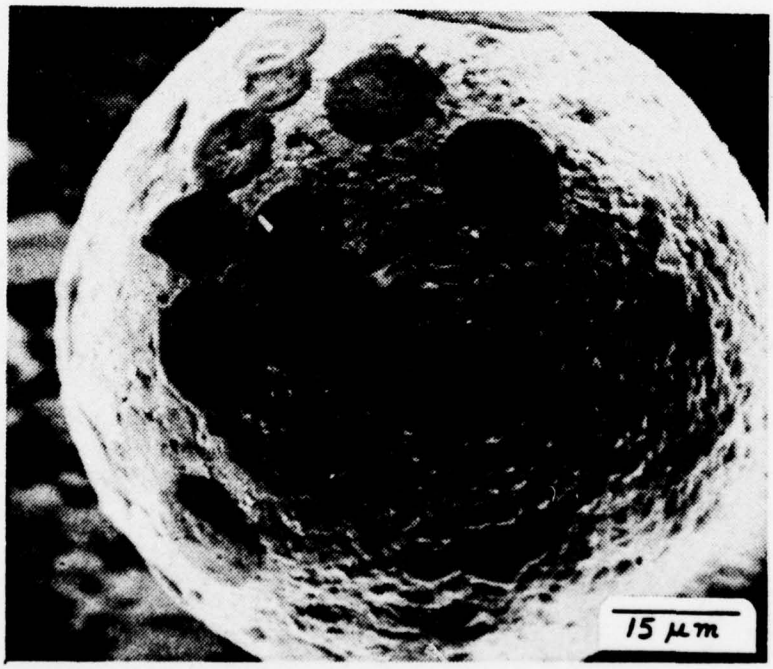

Figure 77. Plated sphere showing growth of "pancake" and "salt and pepper" oxidation products; 30 seconds at 50 mA/cm^2 in 9.96N KOH, 1200X.

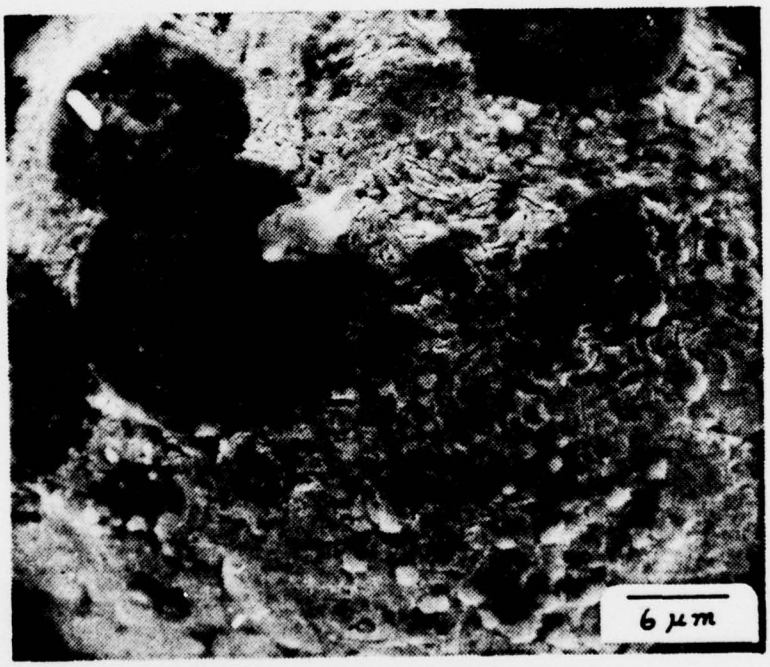

Figure 78. Close view of "pancake" and "salt and pepper" oxidation products on plated sphere surface; transparency of "pancakes" may be observed; 30 seconds at 50 mA/cm^2 in 9.96N KOH, 2400X.

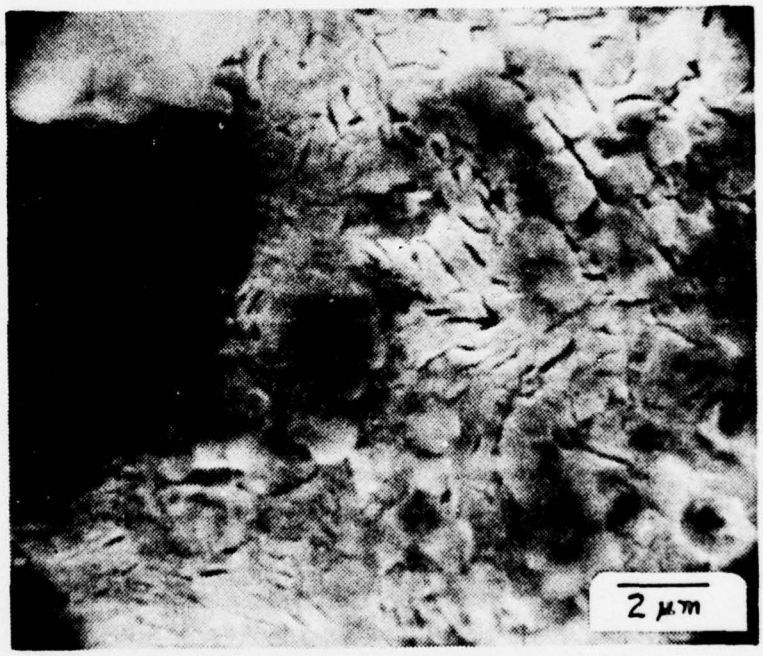

Figure 79. High magnification view of "salt and pepper" oxidation product on plated sphere surface; transparent dark and gray patches are "pancake" oxidation products; 30 seconds at 50 mA/cm^2 in 9.96N KOH, 6100X.

1. Quantitative Results

Summarized quantitative data for both two-dimensional and three-dimensional experiments are presented in Table II, categorized according to predominant observed features.

2. Postulated Oxidation Model

In order to explain qualitatively the events responsible for observed results that occurred during this study, a six step model is postulated which describes the zinc anode behavior through passivation. The model is discussed here and conceptualized in Figure 80.

Starting with the exposure of a clean zinc anode (step 1) to KOH, the initial process that occurs is dissolution pitting (step 2). The pitting process is preferential, showing greater pitting at grain boundaries, inclusion sites, and high stress locations. The zinc ions produced during this dissolution form oxidation products, in reacting with electrolyte, which are subsequently dissolved by the electrolyte to form complex zincate ions. In this step, the rate of oxidation product dissolution exceeds the rate of formation, due to a low zincate concentration in the electrolyte and the ability of the electrolyte to supersaturate in zincate.

The first deposited oxidation products appear in step 3 as small, precipitated white particles, generally locating at sites removed from the actively dissolving pit sites. The rate of dissolution of oxide product has decreased below the rate of formation at this time due to an increase in the concentration of zincate in the electrolyte. Almost simultaneously with step 3, step 4 occurs, in which gray product begins growing as a layer on the anodic surface; the gray layer begins

Table II

SUMMARY OF ZINC ANODE OXIDATION QUANTITATIVE RESULTS

Feature	Quantitative Value	Comments
Anode microstructure grain parameters	Average diameter: 50.5 μm Average density: 2.8×10^4 grains/cm^2	Two-dimensional anode only.
Penetration distance	Less than 2 mm (from reduction profile) 0.84-2.4 mm (from visual observation)	Two-dimensional anode only; 1.35 mm most frequent observed value.
Etch pits	Average diameter: 2-4 μm Average density: 9.1×10^5-1.25×10^7 pits/cm^2	Smallest size and largest density found in three-dimensional experiments.
Gray oxidation product (ZnO)	Thickness: 0.2-5.0 μm "Crack" length: 0.5-3.0 μm (plated spheres only)	Appears as compact, surface adherent layer.
White oxidation product (ZnO)	Diameter: 0.5-10.0 μm Density: 7.7×10^4 particles/cm^2 - full cover	Loose, flocculent, spherical particles; found with or without gray product.
Pancake oxidation product	Diameter: 3.8-8.7 μm Thickness: 0.8-1.5 μm	Dark, smooth, circular product appearing on a few plated spheres; believed to be silver oxide product.

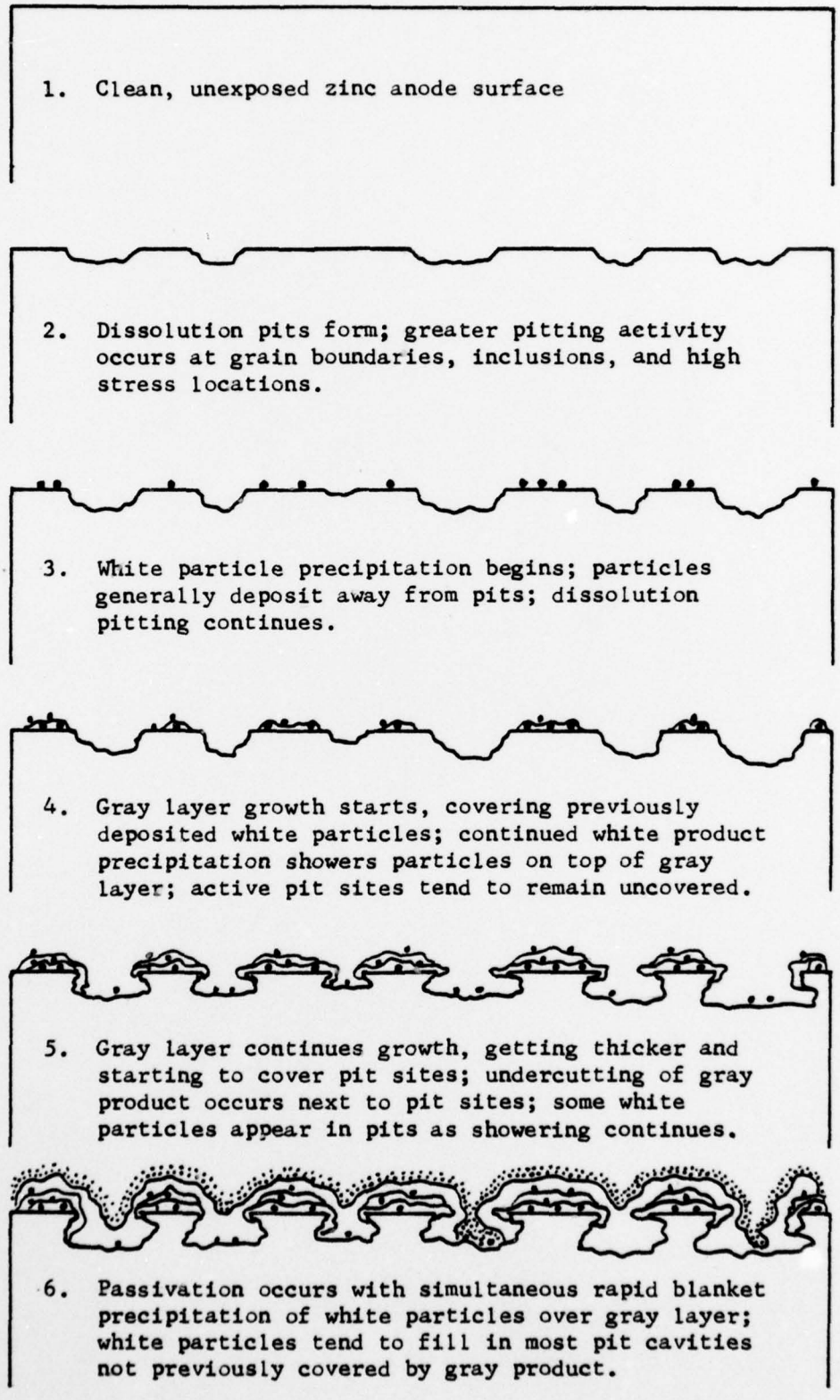

Figure 80. Zinc anode oxidation model.

growth closest to the cathode and moves toward anodic locations further away from the cathode. The beginning of gray layer growth is related to a minimum threshold current-time product, and layer movement is associated with non-uniform anodic current distribution such that movement progresses from locations of high current density to locations of lower current density. Gray layer growth initially remains away from active pit sites and tends to cover previously deposited white precipitate particles. The gray product is not the result of a precipitation mechanism; instead, it forms directly upon the anode surface as a relatively insoluble product of oxidation. As the gray product forms and grows, precipitated white product continues to shower upon it.

Continued growth of gray product proceeds in step 5, and the layer thickness increases. In its horizontal growth, the gray layer begins to cover some pit sites, and as a result, the dissolution process within pits being covered produces undercutting of the oxidation layer. As time passes, pit sites close to the cathode are completely covered by the growing gray layer. As the gray layer growth process proceeds, simultaneous precipitation of white product lightly covers the gray surface, and white product begins to also appear within some uncovered pits. The amount of white product accumulating on the surface is greater than in step 4, but coverage is still relatively sparse. Zincate concentration in the electrolyte has increased and is approaching supersaturation values.

As passivation (step 6), pit sites closest to the cathode are covered by a very thick gray layer, other more remote pit sites may be lightly covered, partially uncovered, or entirely uncovered,

depending upon the extent of remoteness. At the time of passivation, a rapid precipitation of white particles occurs over most of the anodic surface, covering the gray layer and also filling in partially covered pit sites, and uncovered pits and anode surface. The white product cover is not uniform and can be extremely dense or a lighter cover, depending upon location. At this point the electrolyte becomes milky colored also, indicating supersaturation with zincate.

The cause of passivation is not fully understood or agreed upon by most researchers. Powers and Breiter [26] have reported the gray layer (Type II ZnO) to be the cause of passivation, while Armstrong and Bell [27] believe a thin, highly resistive film, whose composition is unknown, to be responsible for passivation of the zinc anode. Armstrong and Bell postulate that the passivating film may be so thin as to be unobservable by conventional means. In this study, rapid white precipitation occurred at passivation, and the gray layer was most complete at passivation, although not entirely complete. These results are insufficient to assert a cause of passivation; however, the lack of complete surface coverage by the gray layer at passivation seems to indicate that the gray layer is not solely responsible for passivation. The complexity of zinc oxidation product formation and dissolution has masked a clear definition of the passivation mechanism, and more extensive research is needed before a clear understanding is possible.

V. CONCLUSIONS AND RECOMMENDATIONS

A. CONCLUSIONS

As a result of this study, the following conclusions have been reached:

1. Anodic oxidation of zinc in KOH electrolyte produces two oxidation products. One product is white and flocculent, depositing as a precipitate from zincate ions in the electrolyte. The other product is gray, adheres tightly to the surface, and forms directly upon the surface. The gray product is not the result of an electrolyte bulk-phase precipitation mechanism but rather is a relatively insoluble product that forms and deposits in close proximity to the reaction site.

2. Oxidation product deposition on the zinc anode requires a minimum current-time product. Prior to achievement of this threshold value, the zinc anode is dissolved through a pitting mechanism in which preferential attack occurs at grain boundaries and other high energy areas in the crystal structure.

3. Dissolution pit sites are active sources of zinc ions throughout the anodic oxidation process. Insulation of pit sites from the electrolyte by film coverage is probably a partial cause of passivation.

4. Penetration of zinc oxidation reactions in a porous structure is limited to less than 2 mm. Electrode thickness values should be comparable.

5. Zinc anode passivation does not have a well defined mechanism. At passivation, the gray product layer is relatively complete, but not entirely, and a rapid precipitation of white product covers the gray layer with a non-uniform layer of white particles. The rapid precipitation indicates that the limit in zincate supersaturation of the electrolyte occurs at or just before passivation.

6. Zinc dendrites are produced as the result of columnar growth of hexagonal zinc plates duirng cathodic plating. Columnar growth is promoted by cathodic hydrogen gas generation.

7. Incomplete zinc plating of silver structures leads to the production of complex oxidation products in KOH such as the "pancakes" observed in this study, which are believed to be silver oxide. This type of unexpected product may introduce added complications in a zinc cell. This may be an important observation for zinc systems since porous zinc electrode manufacture frequently utilizes a zinc plated silver grid.

B. RECOMMENDATIONS

A great disappointment in this study was the failure to obtain useful data from the three-dimensional sectioned bed experiment. More insight into the porous zinc anode oxidation process would have been gained with success in this experiment. It is therefore recommended that future zinc anode research efforts be directed toward an operable sectioned electrode design. More comprehensive penetration profile information could be obtained as well as the current density dependance of such a profile. The lack of zinc sphere-to-sphere conductivity needs to be addressed and solved if future porous electrode models depend upon sphere bed design.

It is also recommended that additional two-dimensional experiments be carried out to confirm the results obtained in this study. This recommendation is made in recognition of the fact that many procedural and technique problems occurred during these experiments which often clouded the results obtained. In order to validate the results of this study, a duplication effort should be carried out, which could not be accomplished during this research effort due to the time constraint placed on student research at the Naval Postgraduate School.

APPENDIX A

TWO-DIMENSIONAL EXPERIMENTAL DATA

EXPERIMENT #1 - Zinc anode oxidation, zinc cathode

CURRENT (mA)	EXPOSURE TIME (sec)	ANODE POTENTIAL (volts)	OBSERVED OXIDATION PRODUCT PENETRATION (units)
0	0	1.35	0
1	0.5	1.37	0
1	0.5	1.37	0
1	0.5	1.37	0
1	1.0	1.37	0
1	2.0	1.37	1
1	5.0	1.42	6
1	2.0	1.42	7
1	2.0	1.42	8
1	5.0	1.42	10
1	5.0	1.42	11
1	5.0	1.42	11
1	5.0	1.43	12
1	5.0	1.43	12
1	5.0	1.43	12
1	5.0	1.43	13

note: 148.2 units = 1cm

EXPERIMENT #2 - Zinc anode oxidation, zinc cathode

CURRENT (mA)	EXPOSURE TIME (sec)	ANODE POTENTIAL (volts)	OBSERVED OXIDATION PRODUCT PENETRATION (units)
0	0	1.37	0
1.0	5	1.37	0
1.0	5	1.37	0
1.0	5	1.37	0
1.0	5	1.37	0
1.0	5	1.37	0
1.0	20	1.37	0
1.0	20	1.37	0
1.0	100	1.31	not observed
1.0	100	1.31	not observed
1.0	100	1.31	not observed
1.0	100	1.31	not observed
10.0	2	Off-scale	not observed
5.0	2	Off-scale	not observed
0.1	10	Off-scale	not observed
1.0	10	1.30	not observed
3.0	10	1.30	not observed
3.0	20	1.33	not observed
3.0	20	1.32	not observed
3.0	50	1.32	not observed
3.0	50	Off-scale	18

note: Several exposures were interrupted due to equipment malfunction; some data therefore may not be accurate.

EXPERIMENT #3 - Reduction of oxidized zinc anode

CURRENT (mA)	EXPOSURE TIME (sec)	AREA REDUCED (cm^2)	CHARGE DENSITY (mC/cm^2)	DISTANCE FROM SEPARATOR (mm)
5.0	4.3	0.0228	943.0	0.122
1.0	8.1	0.0291	278.0	0.398
0.5	5.9	0.0133	221.0	0.692
0.1	63.8	0.0437	146.0	1.000
0.3	21.9	0.0367	179.0	1.420
0.3	20.7	0.1300	47.8	2.280
0.3	10.4	0.1300	54.7	3.700
0.3	7.6	0.1840	16.0	5.360

note: Portion of anode was masked with tape to allow reduction of one small area at a time.

EXPERIMENT #4 - Zinc anode oxidation, zinc cathode

CURRENT (mA)	EXPOSURE TIME (sec)	ANODE POTENTIAL (volts)	OBSERVED OXIDATION PRODUCT PENETRATION (units)
1.0	50	1.36	0
1.0	50	1.36	0
1.0	50	1.36	0
1.0	50	1.36	0
1.0	50	1.36	0
1.0	50	1.36	8
1.0	50	1.36	8
1.0	50	1.37	not observed
1.0	50	1.37	not observed
1.0	50	1.40	16
1.0	50	1.41	not observed
1.0	50	1.41	20

EXPERIMENT #5 - Zinc anode oxidation, copper cathode

CURRENT (mA)	EXPOSURE TIME (sec)	ANODE POTENTIAL (volts)	OBSERVED OXIDATION PRODUCT PENETRATION (units)
1.0	50	unstable	0
1.0	50	1.48	0
1.0	50	not observed	not observed
1.0	50	not observed	not observed
1.0	50	not observed	not observed
1.0	50	not observed	15
1.0	50	not observed	not observed
1.0	50	not observed	20
1.0	50	not observed	20
1.0	50	not observed	20
1.0	50	not observed	20
1.0	50	not observed	20

note: Reference electrode malfunction occurred during experiment; also, large amount of hydrogen generation disturbed current distribution and made observations difficult.

EXPERIMENT #6 - Zinc anode oxidation, copper cathode

CURRENT (mA)	EXPOSURE TIME (min)	OBSERVED OXIDATION PRODUCT PENETRATION (units)
1.0	11	35
4.0	12	35
1.0	10	35

note: Hydrogen gas generation blocked current at front of anode; fresh electrolyte added several times during experiment; dendrites grew from cathode to anode causing shorting.

EXPERIMENT #7 - Zinc anode, zinc cathode

CURRENT (mA)	EXPOSURE TIME (min)	AVERAGE PASSIVATION TIME (min)
4.0	98	17.5

note: Exposure time is the sum total of several shorter duration runs to passivation; after passivation, electrolyte was renewed for new run; visible coating of white precipitate at passivation cleared with new electrolyte addition.

EXPERIMENT #8 - Zinc anode oxidation, copper cathode

CURRENT (mA)	EXPOSURE TIME (min)
6.0	15

note: This was a continuous run to passivation; at passivation white precipitate rapidly covered anode surface.

APPENDIX B

THREE-DIMENSIONAL EXPERIMENTAL DATA

EXPERIMENT #1 - Sectioned sphere bed experiment

SAMPLE TYPE: zinc spheres anode

COUNTER ELECTRODE: silver/silver oxide

ANODE BED THICKNESS: 1.0 cm

SECTION THICKNESS: 0.005 cm (first section)

0.010 cm (subsequent sections)

TOTAL CURRENT PASSED: 7.81 mA

CURRENT DENSITY: 5.0 mA/cm^2

EXPOSURE TIME: 10 min (continuous)

ELAPSED EXPOSURE TIME (min)	ANODIC POTENTIAL (volts)
0	1.366 (open circuit)
2	1.200
4	1.201
7	1.206
8	1.208
9	1.166
10 (current stop)	1.163
11	1.378 (open circuit)
12	1.385 (open circuit)

EXPERIMENT #2 - Monolayer experiment

RUN #	SPHERE TYPE	CURRENT DENSITY (mA/cm^2)	EXPOSURE TIME (seconds)	ANODE POTENTIAL (volts)
1	plated	50	30	not recorded
2	plated	25	30	1.056
3	plated	5	30	1.218
4	plated	10	30	1.193
5	plated	1	30	1.253
6	zinc	1	30	not recorded
7	zinc	10	30	1.171
8	zinc	50	30	off-scale
9	silver	50	30	off-scale

LIST OF REFERENCES

1. Garrett, A. B., Batteries of Today, Research Press, Dayton, Ohio, 1957.

2. Falk, S. U. and Salkind, A. J., Alkaline Storage Batteries, Wiley, New York, 1969.

3. Heise, G. W. and Cahoon, N. C., The Primary Battery, Wiley, New York, 1971.

4. Vinal, G. W., Storage Batteries, Wiley, New York, 1955.

5. Newman, J. S. and Tobias, C. W., "Theoretical Analysis of Current Distribution in Porous Electrodes," Journal of the Electrochemical Society, v. 109, p. 1183, 1962.

6. Wagner, C., "Theoretical Analysis of the Current Density Distribution in Electrolytic Cells," Journal of the Electrochemical Society, v. 98, p. 116, 1951.

7. Newman, J. and Tiedemann, W., "Porous Electrode Theory with Battery Applications," AIChE Journal, v. 21, p. 25, 1975.

8. Delahay, P. and Tobias, C. W., Advances in Electrochemistry and Electrochemical Engineering, v. 5, p. 87, Wiley, 1967.

9. Fleischer, A. and Lander, J. J., Zinc-Silver Oxide Batteries, Wiley, New York, 1971.

10. Yardney Electric Corporation, Energy Data Book, p. 10, 1965.

11. MacBreen, J., "Zinc Electrodes Shape Change in Secondary Cells," Journal of the Electrochemical Society, v. 119, p. 1620, 1972.

12. Air Force Aero Propulsion Laboratory, Wright-Patterson AFB, Technical Report AFAPL-TR-71-32, Control Experiments on Active Material Migration in Zinc Electrodes, by J. J. Lander and J. E. Cooper, October 1971.

13. Air Force Aero Propulsion Laboratory, Wright-Patterson AFB, Technical Report AFAPL-TR-76-9, Engineering Analysis of Shape Change in Zinc Secondary Electrodes, by K. W. Choi, D. Hamby, D. N. Bennion, and J. Newman, March 1976.

14. Katan, T. and Bauman, H. F., "Relating Structural Variables of Porous Electrodes," Journal of the Electrochemical Society, v. 122, p. 77, 1975.

15. Szpak, S. and Katan, T., "An Experimental Study of Reaction Profiles in Porous Electrodes," Journal of the Electrochemical Society, v. 122, p. 1063, 1975.

16. MacBreen, J. and Dalin, G. A., "The Mechanism of Zinc Shape Change in Secondary Batteries," Extended Abstracts, The Electrochemical Society, Inc., Battery Division, v. 11, p. 123, 1966.

17. Katan, T., Szpak, S., and Bennion, D. N., "Silver/Silver Chloride Electrodes: Surface Morphology on Charging and Discharging," Journal of the Electrochemical Society, v. 121, p. 757, 1974.

18. Metals Handbook, v. 8, p. 2, American Society for Metals, 1973.

19. Cambridge Scientific Instruments Limited, Manual TL 1116-OM-96118-002, Stereoscan S4-10 Scanning Electron Microscope, Issue 1.

20. Heyer, R. H., Engineering Physical Metallurgy, D. Van Nostrand Co., New York, 1940.

21. Luebke, H. L., A Scanning Electron Microscope Study of the Effects of Anode Velocity and Current Density on the Corrosion of Ship Hull Zinc in Synthetic Sea Water, MSME Thesis, Naval Postgraduate School, June 1976.

22. Powers, R. W., "Film Formation and Hydrogen Evolution on the Alkaline Zinc Electrode," Journal of the Electrochemical Society, v. 118, p. 685, 1971.

23. Powers, R. W., "Anodic Films on Zinc and the Formation of Cobwebs," Journal of the Electrochemical Society, v. 116, p. 1652, 1969.

24. Nagy, Z. and Bockris, J., "On the Electrochemistry of Porous Zinc Electrodes in Alkaline Solutions," Journal of the Electrochemical Society, v. 119, p. 1129, 1972.

25. Hull, M. N., Ellison, J. E., and Toni, J. E., "The Anodic Behavior of Zinc Electrodes in Potassium Hydroxide Electrolytes," Journal of the Electrochemical Society, v. 117, p. 192, 1970.

26. Powers, R. W. and Breiter, M. W., "The Anodic Dissolution and Passivation of Zinc in Concentrated Potassium Hydroxide Solutions," Journal of the Electrochemical Society, v. 116, p. 719, 1969.

27. Armstrong, R. D. and Bell, M. F., "The Electrochemical Behaviour of Zinc in Alkaline Solution," Electrochemistry, v. 4, p. 1, 1974.

INITIAL DISTRIBUTION LIST

		No. Copies
1.	Defense Documentation Center Cameron Station Alexandria, Virginia 22314	2
2.	Library, Code 0212 Naval Postgraduate School Monterey, California 93940	2
3.	Department Chairman, Code 69 Department of Mechanical Engineering Naval Postgraduate School Monterey, California 93940	2
4.	Associate Professor A. J. Perkins, Code 69Ps Department of Mechanical Engineering Naval Postgraduate School Monterey, California 93940	5
5.	Dr. Ted Katan Lockheed Palo Alto Research Laboratory, 52-35/204 3251 Hanover Street Palo Alto, California 94304	2
6.	Lieutenant J. R. Savory, USN Engineering Duty Officer School, Class 3-77B Mare Island Vallejo, California 94592	4
7.	Office of Naval Research (ONR) Arlington, Virginia 22217 Attn: Dr. George Neece, Code 472	1
8.	Office of Naval Research Branch Office 1030 East Green Street Pasadena, California 91106 Attn: Dr. R. J. Marcus	1
9.	Naval Research Laboratory Washington, D. C. 20375 Attn: Mr. Eugene Wells, Mr. Al Simon	1
10.	Dr. John J. Lander Energy Conversion Branch, Aerospace Power Division Air Force Wright Aeronautical Labs (AFSC) WPAFB, Ohio 45433	1

11. Naval Sea Systems Command — 1
Code 0331C
Washington, D. C. 20362
Attn: Mr. John W. Murrin

12. Naval Surface Weapons Center (White Oak) — 1
Electrochemistry Branch
Silver Spring, Maryland 20910
Attn: Dr. J. H. Ambrus

13. Naval Ship Engineering Center (NAVSEC) — 1
Battery Section, Code 6157D
Crystal City, Washington, D. C. 20360
Attn: Mr. Al Hemy

14. Energy Research and Development Agency (ERDA) — 1
Division of Energy Storage Systems
20 Massachusetts Ave.
Washington, D. C. 20545
Attn: Mr. Kurt Klunder

15. Naval Sea Systems Command (NAVSEA) — 1
Code 0331
Washington, D. C. 20360
Attn: Mr. Sol Matesky

16. Naval Underwater Systems Command (NUSC) — 1
San Diego, California 92132
Attn: Dr. P. Hirschler

17. International Lead Zinc Research Organization — 1
292 Madison Ave.
New York, N.Y. 10017
Attn: Mr. Al Cook

18. Dr. G. Goodman — 1
Globe-Union, Inc.
5757 North Green Bay Ave.
Milwaukee, Wisconsin 53201

19. Dr. J. Boechler — 1
Electrochimica Corp.
2485 Charleston Road
Mountain View, California 94040

20. Dr. R. C. Chudacek — 1
McGraw-Edison Co.
Edison Battery Division
Box 28
Bloomfield, New Jersey 07003

21. Yardney Electric Corporation — 1
Yardney Electric Division
82 Mechanic Street
Pawcatuck, Connecticut 02891
Attn: Mr. C. Gill, Mr. W. Ryder

22. Commander, Naval Air Systems Command — 1
Department of the Navy
Washington, D. C. 20360
Attn: Code 310C (Mr. H. Rosenwasser)

23. U. S. Army Research Office — 1
Box 12211
Research Triangle Park, North Carolina, 27709
Attn: CRD-AA-IP

24. Dr. A. L. Slafkosky — 1
Scientific Adviser
Commandant of the Marine Corps
Code RD-1
Washington, D. C. 20380

25. The Assistant Secretary of the Navy (R&D) — 1
Department of the Navy
Room 4E736, Pentagon
Washington, D. C. 20350